PH.D. THESIS

Università degli Studi di Padova
Department of Physics and Astronomy "G. Galilei"

PH.D. COURSE IN
SCIENCE AND ENGINEERING OF MATERIALS AND NANOSTRUCTURES
XXXII SERIES

Two-Dimensional Nanostructure Arrays for Plasmonic Nanolasers

Coordinator: *Ch.mo Prof. Giovanni* MATTEI
Supervisor: *Prof.ssa Tiziana* CESCA
Co-Supervisor: *Ch.mo Prof. Giovanni* MATTEI

Ph.D. Student: *Diego* PICCOTTI

To Martina, my family, my friends
and all the NanoStructures Group,
in particular my supervisor Tiziana and Prof. Giovanni Mattei.

一、血気の勇を戒むること 一、礼儀を重んずること 一、努力の精神を養うこと 一、誠の道を守ること 一、人格完成に努むること 訓

榎�木慶之輔

Dōjō kun

Hitotsu Jinkaku Kansei Ni Tsutomeru Koto
Each person **must strive for the completion and perfection** of one's character

Hitotsu Makoto No Michi Wo Mamoru Koto
Each person must be faithful and protect the way of truth

Hitotsu Doryoku No Seishin Wo Yashinau Koto
Each person must endeavor (fostering the spirit of effort)

Hitotsu Reigi Wo Omonzuru Koto
Each person must respect others and the rules of etiquette

Hitotsu Kekki No Yu Wo Imashimuru Koto
Each person must refrain from hot blooded behavior (guard against impetuous courage)

Abstract

The interest for plasmonic nanolasers has been growing in the last ten years, since they are one of the most promising ways to reach the miniaturization of lasers. In fact, these devices could break the limit of physical confinement of light thanks to the virtual cavity given by plasmonic nanostructures which substitutes the current macroscopic optical cavities. These plasmonic devices can also support high speed operation mode, low lasing threshold and a narrow directional emission.

For this reason, during this project, we focused on the design, the synthesis and the characterization of plasmonic nanolasers based on Au nanodome arrays and Ag nanodisk arrays. In order to synthesize highly ordered nanostructure arrays, we used Nanosphere Lithography (NSL), which is a cost effective and high throughput technique based on the self-assembling of polystyrene nanospheres. Thanks to the versatility of NSL, we have developed different nanofabrication protocols, combining NSL with Reactive Ion Etching (RIE) and Physical Vapor Deposition (PVD). Therefore, we investigated the optical properties of our synthesized arrays, recreating the optical band structure along the high symmetry directions of the reciprocal space. Suitable dye emitters (Pyridine 2 and Styryl 9M) were selected in order to couple their emission with the optical modes of the nanoarrays, on the basis of optical band structure information. In addition, in order to optimize the plasmonic properties and the local field enhancement of the metallic nanostructures, numerical simulations by COMSOL Multiphysics$^{\circledR}$ were performed.

The interaction between dye and plasmonic structure generated an amplified emission. In particular, for Au nanodome arrays coupled with Pyridine 2 dissolved in ethanol, an amplification on the emission arises at $720\,\text{nm}$ with a threshold behavior at $0.9\,\text{mJ}/\text{cm}^2$ and the FWHM of $14\,\text{nm}$. Furthermore, a highly directional emission was obtained at $17°$ with an angular divergence of $3°$ which takes place along the Rayleigh anomaly mode. By comparing the results of Au nanodome arrays and silica nanodome arrays, we concluded that lattice modes give a contribution to the emission directionality, while plasmonic modes provide a reduced lasing threshold overcoming the energy loss.

Ag hexagonal nanodisk array showed a similar behavior to the Au nanodome arrays: we found a lasing threshold at $1.6\,\text{mJ}/\text{cm}^2$, with also a similar FWHM. In this case, the emission is directed at $65°$ and presents an angular divergence of about $14°$.

Moreover, we investigated a nanolaser with a solid-state gain medium for the interest in applications and for the device integration on a chip. The Styryl 9M laser dye is embedded in a PMMA film and coupled with an Au nanodome array. This solid-state system presents an amplified emission at $795\,\text{nm}$ with a threshold of $1.2\,\text{mJ}/\text{cm}^2$ and a FWHM of about $26\,\text{nm}$. The sample shows also a directional emission at $24°$ and with an angular divergence of $6°$. Further investigations have shown the possibility to eliminate the substrate, creating a self-standing device, which exhibits an amplified emission with similar properties of that with the substrate.

Finally, in order to discern the spontaneous or stimulated nature of the emission, we performed coherence measurements of the emitted beam. By a modified Michelson interferometer, a coherence length of about $29\,\mu$m was determined for Au nanodome arrays above threshold. This result demonstrated that a coherent, low-threshold and highly directional emission can be obtained by coupling a suitable fluorescent dye to a properly designed virtual cavity realized by an ordered array of plasmonic nanostructures.

Estratto

Nell'ultima decina di anni, l'interesse per i nanolaser plasmonici è cresciuto siccome sono uno tra i modi più promettenti per la miniaturizzazione dei laser. Infatti, questi dispositivi possono superare il limite di confinamento fisico della luce, grazie alla cavità virtuale data dalle nanostrutture plasmoniche che sostituiscono la convenzionale cavità ottica macroscopica. Inoltre, questi dispositivi plasmonici possono supportare modalità di funzionamento ad alta velocità, bassa soglia di emissione laser e una direzionalità ben definita.

Per questa ragione, durante questo progetto, ci siamo concentrati sulla progettazione, la sintesi e la caratterizzazione di nanolasers plasmonici basati su array di nanocupole di oro e array di nanodischi di argento. Al fine di sintetizzare reticoli di nanoparticelle con un ordine elevato, abbiamo utilizzato la Nanosphere Lithography (NSL), una tecnica economica e ad alta produttività basata sull'autoassemblaggio di nanosfere di polistirene. Grazie alla versatilità della NSL, abbiamo sviluppato diversi protocolli di nanofabbricazione, combinando la NSL con i processi di Reactive Ion Etching (RIE) e deposizione fisica da vapore (PVD). Successivamente, abbiamo studiato le proprietà ottiche dei campioni sintetizzati, ricostruendo la struttura a bande ottica lungo le direzioni di alta simmetria dello spazio reciproco. Abbiamo selezionato due adeguati emettitori coloranti, la Pyridine 2 e lo Styryl 9M, al fine di accoppiare la loro emissione con le modalità ottiche dei reticoli nanostrutturati, sulla base delle informazioni della struttura a bande ottica. Inoltre, per ottimizzare le proprietà plasmoniche e l'amplificazione del campo locale delle nanostrutture metalliche, delle simulazioni numeriche sono state effettuate tramite il software COMSOL Multiphysics$^\circledR$.

L'interazione tra il colorante e la struttura plasmonica ha generato un'emissione amplificata. In particolare, nel reticolo di nanocupole di oro accoppiato alla piridina 2 disciolta in etanolo, un'amplificazione dell'emissione si presenta a $720\,\mathrm{nm}$ con un comportamento a soglia a $0.9\,\mathrm{mJ/cm^2}$. Inoltre, è stata ottenuta un'emissione direzionale a $17°$ con una divergenza angolare di $3°$ che avviene lungo l'anomalia di Rayleigh. Confrontando i risultati dei reticoli di nanocupole di oro con quelli dei reticoli di nanocupole di silice, abbiamo concluso che i modi di reticolo danno un contributo alla direzionalità dell'emissione, mentre i modi plasmonici forniscono una riduzione della soglia laser superando così la perdita di energia.

Il reticolo esagonale di nanodischi di argento mostra un comportamento simile a quello con le nanocupole di oro: abbiamo trovato una soglia laser a $1.6\,\mathrm{mJ/cm^2}$, con anche una simile FWHM. In questo caso, questo fascio è diretto a $65°$ e presenta una divergenza angolare di circa $14°$.

Inoltre, abbiamo studiato anche un nanolaser con un mezzo di guadagno a stato solido per l'interesse nelle applicazioni e nell'integrazione di dispositivi su chip. Il colorante laser Styryl 9M è incorporato in un film di PMMA e accoppiato con un reticolo

di nanocupole di oro. Questo sistema a stato solido presenta un'emissione amplificata a 795 nm con una soglia di $1.2\,\text{mJ/cm}^2$ e una FWHM di circa 26 nm. Questo campione manifesta anche un'emissione direzionale a $24°$ con una divergenza angolare di $6°$. Ulteriori ricerche hanno dimostrato la possibilità di eliminare il substrato, creando un dispositivo autoportante, che presenta un'emissione amplificata con proprietà simili a quella con il substrato.

Infine, per discernere la natura spontanea o stimolata dell'emissione, abbiamo misurato la coerenza del raggio emesso. Tramite un interferometro di Michelson dedicato, la lunghezza di coerenza è stimata a circa $29\,\mu$m per i reticoli di nanocupole d'oro sopra la soglia. Questo risultato ha dimostrato che è possibile ottenere un'emissione coerente, a bassa soglia e altamente direzionale, accoppiando un colorante fluorescente adeguato con una cavità virtuale opportunamente progettata e realizzata da una reticolo ordinato di nanostrutture plasmoniche.

Contents

Introduction

The continuous advancement of technology, required by the pressing and inexhaustible evolution of the market, has led the study of materials increasingly to the center of industrial development and research. Especially in recent years, the interactions of electromagnetic waves and matter at the nanoscale have created a strong interest in scientific research, both as a pure and an applied study.

"*Atoms on a small scale behave like nothin gon a large scale, for they satisfy the laws of quantum mechanics. So, as we go down and fiddle around with the atoms down there, we are working with different laws, and we can expect to do different things.*" [1] citing Richard Feynman's speech held in December 1959 at the annual meeting of the American Physical Society at the California Institute of Technology (Caltech). As Feynman foresaw, materials at nanoscale dimension have different and innovative properties as a function of size, such as optical, magnetic, catalytic and mechanical properties.

One of the most attractive area of interest in nanoscience is *Nanophtonics* which studies the behaviour of radiation, typically in the UV, visible and infra-red (IR) range, at the nanoscale and the interaction between nanometric objects and light. In this field the study of the properties of electromagnetic waves interacting with metal nanostructures, in particular noble metals, is called *Plasmonics*. Plasmonics offers a control of the light confinement below the diffraction limit (namely half of the wavelength $\lambda/2$) and of the consequent enhancement of the optical near-field [2].

In fact, the diffraction limit places a physical limit on the miniaturization of optical and optoelectronic devices, making it impossible to scale down all those devices that require light confinement. In particular optical cavities, which are a major component of lasers, suffer of this limit. LASER (*light amplification by stimulated emission of radiation* [3]), is a device that emits light whose peculiarities are the coherence, the monochromaticity and a high directionality with the ability to reach extremely high powers.

Since its invention in 1960, consisting of a ruby crystal as gain medium which emitted red light [4], the laser has revolutionised the scientific research, such as by opening up new ways of investigation and manipulation of matter, but also in the other research fields and in everyday life. Today it is used conspicuously in many applications and devices, from ordinary pointers, code scanners, CD / DVD / Blue-ray players, in medicine, surgery, aesthetics, military, metrology, metal cutting, motoring , classic or 3D printers. The enormous use of these devices stimulates their continuous development and the parallel progress in materials science has made a significant contribution to the improvement of lasers. For example, the introduction of organic semiconductors (e.g. dyes), which combine novel properties to simple manufacture with the possibility to tune the chemical structure to obtain desired features [5], has led a rapid development of organic semiconductor lasers. These are based on light-emitting diodes, which are easily found in simple displays, open up the possibility of compact and low-cost visible lasers suit-

able for several applications, from diagnosis to sensing, from communications to optical circuits.

However, when we scale these devices down, they present a physical limit given by the impossibility to confine light below the diffraction limit. Plasmonics can overcome these limits thanks to the confinement of electromagnetic waves by metallic nanostructures. The physical phenomenon behind these properties is the excitation of *surface plasmons* (SPs). These consist of the collective oscillation of free electrons at the interface between two materials with the real part of the dielectric function ($Re[\epsilon]$) of opposite sign, such as a metal and a dielectric. The coherent oscillation of the electrons generates an evanescent wave in the dielectric that amplifies the electromagnetic field locally in proximity of the metallic surface [6]. The local field acts as in an optical cavity and in this sense a plasmonic structure can be interpreted as a cavity.

The idea, first proposed by Bergman and Stockman in 2003, is to adopt localized surface plasmons as cavities to amplify the stimulated emission of an emitter, thus defining the concept of SPASER, *surface plasmon amplification by stimulated emission of radiation* [7]. To date the concept of SPASER is still evolving and the inclusion of travelling surface plasmon polariton amplifiers or plasmonic nanolasers, is still under discussion. Since 2007, when the first experimental demonstration of a SPASER was presented [8], the race for miniaturization has led to the fabrication of nanolasers with unique architectures [9–15].

However, the main difficulty encountered to create these devices is the inherent loss of the metal material, which makes the mechanism less efficient. The most exploited solution today is to create a plasmonic-photonic hybrid system, where the diffractive effects of the lattice meet with the plasmonic properties of individual particles, giving rise to a collective phenomenon, called plasmonic *surface lattice resonance* (SLR) [16]. This mode, unlike that of a single particle, is characterized by the suppression of radiative losses and has a narrower resonance, which guarantees a better efficiency. Devices created by exploiting the SLR phenomenon are often called Lattice Plasmon Lasers.

Proposed in 2008 by Zheludev et al. by using split-ring resonators at infrared wavelength [17], it was then demonstrated in 2012 by Suh and Odom et al. with gold nanobowties arranged in a square lattice coupled with a dye (IR140) in polyurethane, exhibiting a laser emission at a wavelength of $873\,\mathrm{nm}$ [12]. The following year, Van Beijnum et al. reported lasing from a metal hole array with a semiconductor (InGaAs) gain, but with a working temperature down to 5K. [18].

In these few years, different groups have studied this type of devices among which the most important are: the Odom group of Northwestern University in Illinois, have studied the possibility of lasing emission by gold, silver [19], aluminium [20] nanodisks and gold nonobowties [12, 21] placed in a square lattice, deepening properties as coherence [22], ultrafast dynamics [23], stretchability [24], tunability [25] and multimodal emission by plasmonic superlattice [26]; The Quantum Dynamics group led by P. Törmä of Aalto University in Finland have studied silver [27], aluminium [28] and nickel [29] nanoparticles arranged in square, honeycomb [30] lattice and 1D chain [31], deepening the ultrafast dynamics [32] and multimodal modes with plasmonic superlattice [33]; Resonant Nanophotonic group led by A. Koenderink of AMOLF Institute in Netherlands, have focused on basic emission properties [34–37] and the role of order [38]; Cunningham et al. have studied lasing emission from plasmic nano-dome arrays [39].

In the present work, the design, synthesis and characterization of novel plasmonic-based nanolaser devices represent the main purpose of the present work. We focused

on studying off-normal directional emission, typical of our devices, and demonstrating the stimulated nature of the emitted beam. Moreover, the synthesis by a cost-effective and high-throughput technique has been taken into particular consideration, proving the possibility of realizing plasmonic nanolasers with a cost-effective way. For this purpose, in the device fabrication, it is employed Nanosphere Lithography (NSL) technique, which allows to create wide areas and fine tuning of the morphology of ordered nanostructures, by self-assembling of polystyrene (PS) nanospheres (NSs) as a lithographic mask [40, 41]. Different nanostructure arrays are designed and synthesized: gold nanodome array and silver nanodisk arrays, arranged in a hexagonal two-dimensional lattice; and silver nanoprism arrays in a honeycomb two-dimensional lattice.

Furthermore, Finite Elements Method (FEM) simulations of the electromagnetic response of the nanoarrays are performed by COMSOL Multiphysics$^{\circledR}$ in order to better understand and help in the optimization of the optical properties of the nanostructured arrays.

The nanoarrays are then characterized by morphological and optical investigations, measuring the photonic dispersion diagram of the plasmonic arrays. Gain medium is then coupled with the nanostructures: it consists in a laser dye (Pyridine 2 or Styryl 9M) dissolved in ethanol or embedded in a polymer matrix (PMMA).

The emission properties of the devices are then characterized taking into account: wavelength, bandwidth, threshold, output direction, angular divergence, polarization and coherence.

The thesis will be structured as follows:

Chapter 1 will describe theoretically the physical mechanism that governs the lasing emission of plasmonic nanolaser devices. First it will be described how a common laser device works, subsequently the plasmonic properties will be explained and how and why they are useful for laser devices.

Chapter 2 will illustrate the synthesis process of the nanostructures in detail, for nanodome, nanodisk and nanoprism arrays, stressing on the fine control of the morphological parameters and thus the plasmonic properties.

Chapter 3 will talk about the morphological and optical characterizations of the plasmonic arrays. It will also present results of Finite Elements Method (FEM) electrodynamic simulation performed by COMSOL Multiphysics$^{\circledR}$ of the electromagnetic response of metal nanostructures.

Chapter 4 will describe the photoluminescence (PL) setup and the modified Michelson interferometer used to characterize the emission properties of the investigated nanosystem. The obtained results about the emission properties of the investigated plasmonic nanolasers are then report and discuss. Furthermore, It will present some possible improvements.

Chapter 5 will report the conclusions and possible future developments.

Chapter 1

Plasmonic Nanolasers

In this chapter we will cover the basics of how a plasmonic nanolaser device works. Firstly, I will introduce the concept of laser and its operation, I will deal briefly with the aspects that concern this work, if you want to deepen the topic I recommend two books: "*Principles of lasers*" of O. Svelto [42] and "*Lasers*" of A. E. Siegman [43]. Subsequently, the plasmonic theory will be described, introducing the concepts that will help us to understand how metallic nanoparticles can be considered as cavities. For further details, I recommend the book "Plasmonics: fundamental and application" of S. Maier [2]. Finally, from the notions explained above, we will be able to describe the operation of a plasmonic nanolaser.

1.1   Principles of LASER

A LASER, acronym of *light amplification by stimulated emission of radiation* [3], is a light source whose emitted radiation is characterized by a high degree of spatial and temporal coherence, high monochromaticity, directionality and the ability to reach extremely high powers, which distinguish it from other light sources. The theoretical foundations of lasers were established by Albert Einstein in 1917 [44], based on the probability of *spontaneous emission*, *stimulated emission* and *absorption* processes occurring (Fig. 1.1).

For simplicity of exposition and for greater clarity, the treatment of the phenomena will be done in a semi-classical approach, in the lowest order approximation, using the rate equation approach. Anyway, this approach is able to describe the most of laser char-

(a) Spontaneous Emission   **(b)** Stimulated Emission   **(c)** Absorption
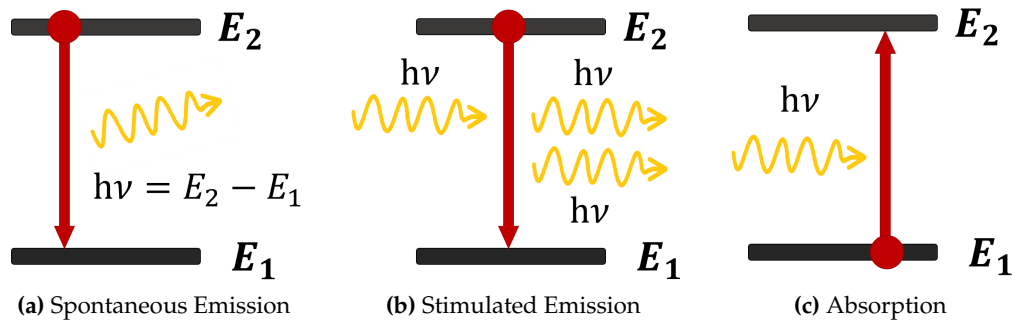
Figure 1.1: Schematic representation of spontaneous emission, stimulated emission and absorption phenomena.

acteristics. However, when it is necessary, it will be noted that the discussion in rate equation approach fails and the correct result, obtained from the purely quantum approach, will be introduced. This because the aim of this chapter is to introduce the basic concepts on the operating and properties of these devices. These concepts will then be applied to the plasmonic nanolaser devices, the subject of our work.

1.1.1 Spontaneous, Stimulated Emission and Absorption

Spontaneous Emission

We consider two energy levels, 1 and 2, of an electron in a given quantum system (atom, molecule, crystal), of energies respectively E_1 and E_2 with $E_1 < E_2$. For simplicity we will assume that level 1 is the ground state, i.e. the state of minimum energy allowed, and that the system is initially in the excited level 2. Since $E_2 > E_1$ the system tends to decay to the level 1 and the corresponding energy difference $E_2 - E_1$ must be transferred from the system. When this energy is released in the form of an electromagnetic (em) wave, the process is called *spontaneous* or *radiative emission* and corresponds to the emission of a photon with energy:

$$h\nu = E_2 - E_1 \tag{1.1}$$

where h is the Planck constant and ν is the frequency of the photon (Figure 1.1a). However, radiative emission is one of the possible ways which the system can decay: the decay, in fact, can also occur by non-radiative ways, in which case the difference of energy $E_2 - E_1$ is released not as an em wave, but for example as kinetic or internal energy of the surrounding.

In a system made up of many equal atoms or molecules, in which at a certain instant a number N_2 of atoms per unit volume are on level 2, the probability of decay by spontaneous emission per unit time and volume, i.e. the rate of decay per unit volume is given by:

$$\left(\frac{dN_2}{dt}\right)_{sp} = -AN_2 = -\frac{N_2}{\tau_{sp}} \tag{1.2}$$

where the positive coefficient A is called spontaneous emission rate or Einstein's A coefficient. $\tau_{sp} = 1/A$ is called average lifetime for spontaneous emission and it is the interval of time after which the probability of finding an atom on level 2 (or after which the number of atoms on level 2) is reduced of a factor $1/e$, due to the spontaneous emission process.

Similarly, we can apply the same considerations for the non-radiative decay, and we can write

$$\left(\frac{dN_2}{dt}\right)_{nr} = -\frac{N_2}{\tau_{nr}} \tag{1.3}$$

with τ_{nr} the effective lifetime of the non-radiative decay process. Unlike τ_{sp} that depends only on the considered transition, τ_{nr} depends not only on the transition but also on the characteristics of the surrounding environment.

Therefore, it can be defined the transition lifetime τ as:

$$\frac{1}{\tau} = \frac{1}{\tau_{sp}} + \frac{1}{\tau_{nr}}$$

and then

$$\frac{dN_2}{dt} = -\frac{N_2}{\tau} = -\left(\frac{N_2}{\tau_{sp}} + \frac{N_2}{\tau_{nr}}\right) \tag{1.4}$$

It can be defined the fluorescence quantum yield Φ as the ratio of the number of emitted photons to the number of atoms initially raised to level 2, as

$$\Phi = -\frac{\int (N_2(t)V/\tau_{sp})dt}{N_2(0)V} = \frac{\tau}{\tau_{sp}} \tag{1.5}$$

where V is the volume of the material, $N_2(t)/\tau_{sp}$ represents the number of atoms decaying in radiative way per unit volume and unit time. From eq. 1.4 result

$$N_2(t) = N_2(0)e^{-t/\tau} \tag{1.6}$$

From eq. 1.6 it emerges that the decay measurement of the emitted radiation decay provides an estimation of the total lifetime τ and not the radiative lifetime τ_{sp}.

Stimulated Emission

Now we consider again the situation in which the system is in the state 2, but it is hit by photon of frequency $\nu = (E_1 - E_2)/h$ (eq. 1.1). In this case there is a finite probability that the wave forces the system to make the transition $2 \rightarrow 1$, via emission of a photon that sums up to the incident one. This process is called *stimulated emission* and is schematically shown in figure 1.1b.

There is a substantial difference with respect to the case of spontaneous emission, in which the photon emitted in the transition can be emitted in any direction and has no definite phase relationship with respect to the other emitted photons. In the stimulated emission process, since the process is forced by the incident em wave (photon), the emission of each system takes place in phase with the incident wave and in the same direction.

We can write this case:

$$\left(\frac{dN_2}{dt}\right)_{st} = -W_{21}N_2 \tag{1.7}$$

where the probability density of a stimulated transition W_{21}, differently from the Einstein's coefficient A, depends on the particular transition and also on the flux F of incident photons (i.e., the number of photons per unit of surface and time) as

$$W_{21} = \sigma_{21}F \tag{1.8}$$

σ_{21} has the dimension of an area and is called *stimulated emission cross-section* and $F = \frac{I}{h\nu}$, where I is the beam intensity, in unit of W/m^2

Absorption

Finally, let's consider the *absorption* process, always between the two levels 1 and 2: in this case the system, which is initially in the fundamental state 1, absorbs an incident photon of frequency ν, corresponding to the energy difference between two states (eq. 1.1), and goes to the excited level 2, as shown in figure 1.1c.

Similarly to the previous processes the absorption probability can be written as

$$\left(\frac{dN_1}{dt}\right)_{a} = -W_{12}N_1 \tag{1.9}$$

where W_{12} is the absorption probability density or rate, which depends on the flux F of photons too, as

$$W_{12} = \sigma_{12}F \tag{1.10}$$

where the *absorption cross-section* σ_{12} depends only on the particular transition.

Furthermore, if the levels are non-degenerate, Einstein demonstrate that $W_{21} = W_{12}$ and $\sigma_{21} = \sigma_{12}$. Generally, if g_1 and g_2 are the degeneracy degrees of state 1 and 2 respectively, then it will be $g_2 W_{21} = g_1 W_{12}$ and $g_2 \sigma_{21} = g_1 \sigma_{12}$.

The absorption cross-section in equation (1.10) is related to the absorption coefficient according to the expression

$$\alpha = \sigma_{12} N_1 \tag{1.11}$$

In order to give a quantitative estimation of the probability coefficients of the transitions a quantum electrodynamics approach is needed. Very briefly by time dependent perturbation theory, with the electric dipole approximation, it is possible to give an expression to $W = W_{12} = W_{21}$:

$$W = \frac{2\pi^2}{3n\varepsilon_0 ch^2} |\mu|^2 I g(\nu - \nu_0) \tag{1.12}$$

where n is the refractive index of the medium, ε_0 is the vacuum permittivity, c is the speed of light, h is the Planck constant, $|\mu| = |\mu_{12}| = |\mu_{21}|$ is the amplitude of the electric dipole moment (that for an atom can be $\sim ea$ where e is the electron charge and a the radius of the atom), I the intensity of the incident radiation and $g(\nu - \nu_0)$ is the transition lineshape.

From equations 1.12 and 1.10, the cross-section σ results

$$\sigma = \sigma_{12} = \sigma_{21} = \frac{2\pi^2}{3n\varepsilon_0 ch} |\mu|^2 \nu g(\nu - \nu_0) \tag{1.13}$$

Under the same approximations we can also derive the Einstein's coefficient A and the spontaneous emission lifetime τ_{sp}

$$A = \frac{1}{\tau_{sp}} = \frac{16\pi^3 \nu_0^3 n |\mu|^2}{3h\varepsilon_0 c^3} \tag{1.14}$$

1.1.2 The LASER idea

Let us now consider a plane wave of intensity $I = h\nu F$, which travels in a certain material, along the z axis. N_1 and N_2 the populations of atoms (number of atoms per unit volume) in levels 1 and 2 of the material and $h\nu = E_2 - E_1$. Propagating in the medium the intensity of the wave will undergo a change $dI = h\nu dF$ (see figure 1.2). We only consider the processes of stimulated emission, which for each incident photon, "adds" another photon in the same direction as the incident one, and absorption that "removes"
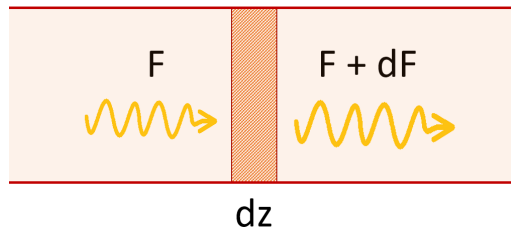
Figure 1.2: Photon flux changing of dF travelling through a material for a distance dz.
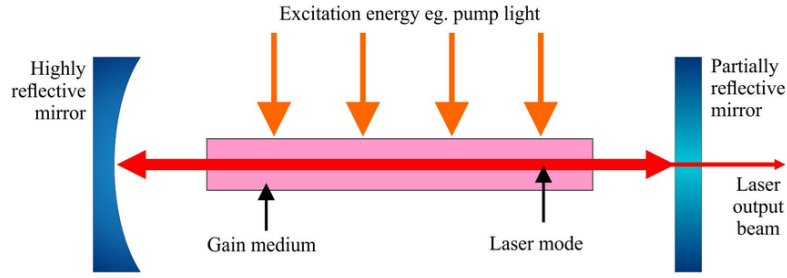
Figure 1.3: Scheme of LASER.

an incident photon. The number of photons added and removed, by unit of time, is given by equations 1.7 and 1.9. Recalling 1.8 and 1.10, we have that:

$$dF = \sigma F(N_2 - N_1)dz \tag{1.15}$$

and we can see that the material behaves like an amplifier ($dF/dz > 0$) if $N_2 > N_1$, while it behaves like an absorber ($dF/dz < 0$) if $N_2 < N1$. At thermal equilibrium the populations are controlled by the Boltzmann statistics:

$$\frac{N_2^e}{N_1^e} = e^{-\frac{E_2 - E_1}{k_B T}} \tag{1.16}$$

where $k_B = 1.38 \times 10^{-23}$ JK^{-1} is the Boltzmann constant, T is the temperature in Kelvin degrees and N_1^e and N_2^e are the equilibrium populations. Therefore, at thermal equilibrium, $N_2 < N_1$ and the material acts like an absorber.

If you can reach a non-equilibrium condition for which there is a *population inversion*, that is a situation in which the populations of the two levels satisfy the condition $N_2 > N_1$, the material acts as an amplifier to the frequency ν. In this case, it is useful to define the gain parameter g instead of the absorption coefficient α and from 1.11 we can write:

$$g = \sigma(N_2 - N_1) \tag{1.17}$$

To obtain an oscillator from an amplifier is necessary to introduce a positive feedback; this is obtained by placing the active material in an optical cavity. Generally, optical cavities or optical resonators confine light by multiple reflection, producing standing waves for specific resonance frequencies ν_r due to the interference phenomena. These standing waves are called resonant modes, which naturally oscillate in the cavity [43].

The easiest configuration of an optical cavity is represented by two flat mirrors (Fabry-Pérot cavity) (figure 1.3).

A plane wave of frequency ν_r in the visible will travel back and forth through the active material and will be amplified at each step. Part of the light can be extracted if one of the mirrors is semi-transparent, like mirror 2. A beam will be extracted, when the population inversion $N_2 - N_1$ is such that the gain per pass in the active material compensates for the losses. We can immediately verify that there is a threshold condition for the laser operation. Named R_1 and R_2 the reflectances of the two mirrors respectively, L_i the internal losses per pass in the cavity and l the length of the active material, the threshold condition results:

$$R_1 R_2 (1 - L_i)^2 e^{2gl} = 1 \tag{1.18}$$

where e^{2gl} represents the ratio between the number of photons present after travelling back and front in the material and the initial one and $R_1 R_2 (1 - L_i)^2$ represents the losses in the double pass. It should be noted that, the semi-reflective mirror (mirror 2) is the element that allows us to extract a usable laser beam outside the cavity formed by the two mirrors: $(1 - R_2)$ represents the fraction of energy (or photons) that is not reflected back into the cavity. From equations 1.18 and 1.17 we see that the threshold condition is reached when the inversion of population, $N_2 - N_1$, reaches a critical value N_c, called *critical inversion*, given by

$$N_c = -[ln R_1 R_2 + 2ln(1 - L_i)]/2\sigma l = \gamma/\sigma l \qquad (1.19)$$

where $\gamma = -[ln R_1 R_2 + 2ln(1 - L_i)]/2$ represents the single pass logarithmic losses of the cavity.

Once the critical inversion is reached, oscillation will build up from spontaneous emission. The photons that are spontaneously emitted along the cavity axis will, in fact, initiate the amplification process.

When one wants to reduce the size of a laser, its operation does not change, however the optical cavities suffer from a shrinking limit due to the confinement of the light imposed by the diffraction limit. The idea of a plasmonic nanolaser is to replace the optical cavity with metallic nanostructures that operate as virtual cavities, as we will see later.

1.1.3 Population Inversion and Rate Equations

How is it possible to generate an inversion of population? The first idea could be to consider a two-level system with a sufficient strong em wave at frequency ν shining on it. Initially $N_1 > N_2$ and absorption predominates on stimulated emission. So more atoms will be raised from level 1 to level 2 than viceversa nonetheless, as soon as the equilibrium of the two populations is reached, $N_1 = N_2$, we can see from eq. 1.15 that the material becomes transparent to the incident radiation: the number of photons absorbed per unit of time is equal to the number of photons emitted per stimulated emission. Therefore, by using only a two-level system, one cannot obtain population inversion.

In order to get population inversion three or more levels have to be considered. The scheme of operation of three- and four-level systems is reported in figure 1.4. For the three-level scheme, the system is exited from level 1 to level 3; if the transition between level 3 to level 2 is quick enough, i.e. $\tau_{32} \ll \tau_{21}$, population inversion can be obtained between levels 1 and 2. However, before obtaining the population inversion, the system have to reach the condition $N_1 = N_2$.

Instead, for a four-level scheme, the ground level is identified as level 0, from which atoms are raised to level 3. From this level, if the atoms rapidly decay into the level 2, i.e. $\tau_{32} \ll \tau_{21}$, a population inversion can be obtained between level 2 end level 1. In level 2, the atoms relax then through spontaneous and stimulated emissions into level 1. At this level, a fast decay ($\tau_{10} \ll \tau_{21}$) into the ground leads to a negligible population in level 1, if level 1 is far enough to level 0, i.e. $E_1 - E_0 > k_B T$. This means that, only a small number of atoms need to be excited in the level 2 to form population inversion, proving that a four-level laser is much more efficient and practical then the three-level laser.

All the systems with more levels can be schematically describes as a three- or a four-level system.

Taking into account a 4 level system, its population dynamics as well as the photon flux can be evaluated by a simple model of rate equations. This model is based on the

(a) Three-level scheme   **(b)** Four-level scheme
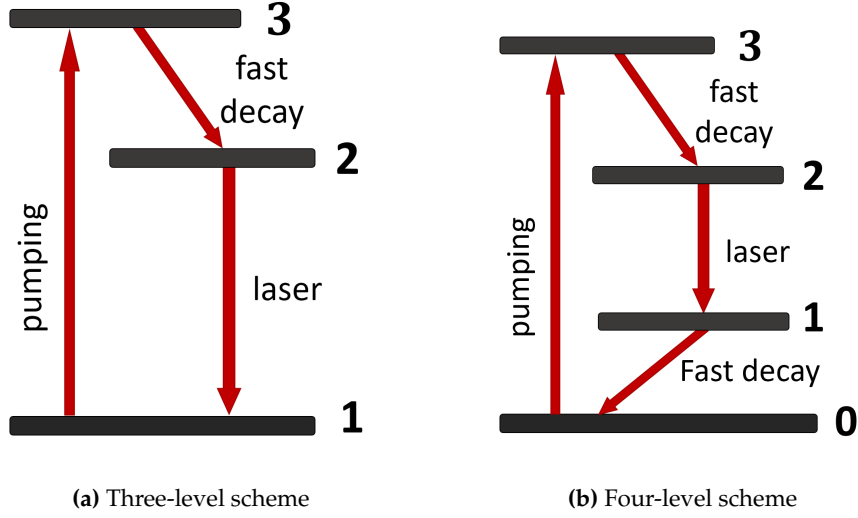
Figure 1.4: Schematic representation of the three- and four-level systems for laser emission.

balance between the atom transitions and the number of the photons created or annihilated.

For a four-level system with non-degenerate levels we can write the system of rate equations as

$$\frac{dN_0(t)}{dt} = \frac{N_1(t)}{\tau_{10}} + \frac{N_3(t)}{\tau_{30}} - W_p \, N_0(t) \tag{1.20a}$$

$$\frac{dN_1(t)}{dt} = \frac{N_2(t)}{\tau_{21}} - \frac{N_1(t)}{\tau_{10}} - F \, \sigma_{21} \left[N_1(t) - N_2(t) \right] \tag{1.20b}$$

$$\frac{dN_2(t)}{dt} = \frac{N_3(t)}{\tau_{32}} - \frac{N_2(t)}{\tau_{21}} + F \, \sigma_{21} \left[N_1(t) - N_2(t) \right] \tag{1.20c}$$

$$\frac{dN_3(t)}{dt} = -\frac{N_3(t)}{\tau_{32}} - \frac{N_3(t)}{\tau_{30}} + W_p \, N_0(t) \tag{1.20d}$$

where W_p, called *pumping rate,* is the rate of the pumping process and describe the excitation probability as

$$\left(\frac{dN_3}{dt} \right)_\nu = W_p N_0 \tag{1.21}$$

Moreover, $N_3(t = 0) \simeq N_1(0) \simeq 0$ and the total population $N_t = N_0 + N_1 + N_2 + N_3$.

We will resume this discussion after introducing the plasmonic properties of nanostructured arrays and then we will see how these can be described the dynamics of a plasmonic nanolaser.

1.1.4 Properties of LASER Beam

The most peculiar properties of a laser beam are:

Monochromaticity

In short, this property is a consequence of two concomitant facts: only the em of frequency ν given by eq. 1.1 can be amplified and, given a resonant cavity, oscillation can occur only at the characteristic resonance frequencies of the cavity. The engineering of the cavity therefore can lead to an extremely narrow bandwidth, below $1\,\text{nm}$.

For our samples, monochromaticity is investigated and will be a fundamental characteristic of emitted beam.

Coherence

- *Spatial coherence.* Given two points P_1 and P_2 of on the wavefront of an em wave at time t_0 and indicating with ε_1 and ε_2 the electric fields respectively, for definition of wavefront, the phase difference between the two electric fields at time t_0 will be zero. If this phase difference remains zero at any time t, the two points will be coherent, and if this it happens whatever the two points on the wavefront are, it is said that the em wave has *perfect spatial coherence*. In practice, for any point P_1, P_2 is contained within a finite area S_c around P_1. In this case it is said that the wave possesses *partial spatial coherence* and for each point P we can introduce an area of coherence $S_c(P)$.

- *Temporal coherence.* Consider the electric field in a generic point P of the wavefront of an em wave at time t and time $(t+\tau)$. If the difference of phase between $E(t)$ and $E(t+\tau)$ remains constant for any time $0 \leq \tau \leq \tau_0$, the em wave has *partial temporal coherence* with a *coherence time* equal to τ_0; if the phase difference remains constant for any one value of τ, it is said that the em wave has *perfect temporal coherence*.

  It is worth noting that the two concepts of spatial and temporal coherence are distinct and that, for example, an em wave can have partial temporal coherence while being perfectly coherent from the spatial point of view.

It is possible to define a *normalized correlation function* at the first-order for the electric field of a light source, which is referred to as the *complex degree of first-order coherence*. This function provides a measure of the coherence between two different points of the wave at two different times.

$$\gamma^{(1)}(\mathbf{r}_1, \mathbf{r}_2, \tau) = \frac{\langle E(\mathbf{r}_1, t+\tau) E^*(\mathbf{r}_2, t)\rangle}{\langle E(\mathbf{r}_1, t) E^*(\mathbf{r}_1, t)\rangle^{1/2} \langle E(\mathbf{r}_2, t) E^*(\mathbf{r}_2, t)\rangle^{1/2}} \tag{1.22}$$

Where $\langle\rangle$ represents the ensemble average. If $\tau = 0$, $|\gamma^{(1)}(\mathbf{r}_1, \mathbf{r}_2, 0)|$ is the *degree of spatial coherence*. Instead if $\mathbf{r}_1 = \mathbf{r}_2 = \mathbf{r}$, $|\gamma^{(1)}(\mathbf{r}, \tau)|$ is the *degree of temporal coherence*. $|\gamma^{(1)}(\mathbf{r}, \tau)| \leq 1$. Moreover, it is possible to define a *coherence time* τ_{co}, such that $|\gamma^{(1)}(\mathbf{r}, \tau_{co})| = 1/2$ and the corresponding *coherence length* $l_{co} = \tau_{co}c$.

Let's consider the superposition of two beam, the intensity profile can be written by the normalized correlation function at the first order as

$$I = I_1 + I_2 + 2\sqrt{I_1 I_2}|\gamma^{(}1)| \cos\left[\omega\tau - \phi(\tau)\right] \tag{1.23}$$

where $\cos\left[\omega\tau - \phi(\tau)\right]$ is the phase of the correlation function. We note that the intensity pattern, i.e. the characteristic fringes of an interference phenomenon, is due to the rapid variation of the cosine.

We can define a visibility V of the fringes as

$$V = \frac{(I_{max} - I_{min})}{(I_{max} + I_{min})} = \frac{2\sqrt{I_1 I_2}}{I_1 + I_2}|\gamma^{(1)}(\mathbf{r}, \tau)| \tag{1.24}$$

If $I_1 = I_2$, so $V = |\gamma^{(1)}(\mathbf{r}, \tau)|$. The visibility can be easily measured and gives us information about the first-order correlation of the two beams, and then the coherence degree. In fact, plotting the visibility $V(\tau)$ as a function of the time delay, the coherence time τ_{co} will be equal to the FWHM of the visibility curve, from its definition.

Since $\gamma^{(1)}$ is related by a Fourier transform to $\Delta\nu$ it is possible to find [45]

$$\tau_{co} \cong \frac{1}{\Delta\nu} \approx \frac{\lambda^2}{c\Delta\lambda} \tag{1.25}$$

from which we note the strong relationship between monochromaticity and temporal coherence. This relation is closely analogous to the Heisenberg uncertainty relation and can be proved using the same procedure as used to derive the uncertainty relation. Furthermore, in section 4.4 it will be explained how to derive the coherence time τ_{co} by a modified Michelson interferometer.

Directionality

Directionality is an important characteristic which is widely use on several applications of lasers, for this reason we will take it into particular consideration for our samples. This property is a consequence of the fact that the active material is placed in a open resonant cavity. Considering for instance a Fabry-Pérot cavity, only a resonant mode can oscillate in the cavity, for the geometry of the resonator, an em wave propagating in the orthogonal direction of the mirrors (or in a direction very close to it), with a suitable frequency ν_r, can oscillate.

Let's first consider a laser beam that has perfect spatial coherence. The intrinsic divergence of this beam, due to the diffraction is given by the ratio:

$$\theta_d = \beta\lambda/D \tag{1.26}$$

where θ_d is the divergence angle, λ the radiation wavelength, D is the diameter of the light beam and β is a numerical factor of the order of the unit that depends on the the amplitude distribution form and how the divergence and diameter of the beam are defined. In this case we speak of a limited laser beam for diffraction. Considering a laser beam with wavelength $\lambda = 630\,\text{nm}$ (red) with a diameter of $3\,\text{mm}$, we obtain, for $\beta = 1$, $\theta_d \sim 2 \cdot 10^{-4}$ rad, or an increase in the diameter equal to $0.4\,\text{mm}$ for each meter of propagation. If the laser beam is only partially coherent in terms of space, the area of coherence S_c behaves as a diffracting element whereby the beam divergence turns out to be

$$\theta_d = \beta\lambda/\sqrt{S_c} \tag{1.27}$$

greater than that limited by diffraction.

Brightness

The power emitted by an em wave source per unit surface area per unit solid angle is defined as *brightness*. More precisely, $dP = B cos\theta dS d\Omega$, where dP is the power emitted

by a surface element dS within the solid angle $d\Omega$ at the angle θ with respect to the normal to the surface element. For an isotropic source, brightness B is a constant. In general, B may depend on θ. For a laser beam B can be very high due to the fact that the beam is collimated.

Given a beam with power P, diameter D and divergence of θ, assuming that θ is very small (i.e., $cos\theta \cong 1$), then it can be found

$$B = \frac{4P}{(\pi D \theta)^2} \tag{1.28}$$

If beam is diffraction limited, $\theta = \theta_d$ so

$$B = \left(\frac{2}{\beta \pi \lambda}\right)^2 P \tag{1.29}$$

which is the maximum brightness that a beam of power P can have.

Short Pulse Duration

Pulsed emission is not an intrinsic property of laser beam and it can be generated by different techniques, such as *Q-switching* or *mode locking*. Pulsed lasers are widely used in many applications due to their possibility to reach high pulse energy or high peak pulse power. Q-switching technique allows to generate ns pulses by introducing loss mechanism which exceeds the gain of the medium. Then it is rapidly removed when energy stored in the medium has approached the maximum possible level, producing short pulses of high energy and peak power.
On the other hand, using the mode locking technique it is possible to produce light pulses of duration equal to approximately the inverse of the line width of the laser transition $2 \rightarrow 1$. For liquid and solid state lasers, having line widths $10^5 - 10^6$ times greater than those of gas lasers, light pulses can be generated of duration of the order of ten fs. The property of short duration, which implies a concentration of energy over time, can be considered as the counterpart of the monochromaticity, which implies a concentration of energy in terms of wavelength.

1.2 Introduction to Plasmonics

Plasmonics is the field of nanophotonics that studies the interaction between electromagnetic (em) radiation and metal nanostructures. This interaction, which strongly depends on the frequency and electronic structure of the metal, can be described in a classical framework based on Maxwell's equations without the need to resort to quantum mechanics. This is valid for metallic structures up to the size of a few nanometers, when the effects due to the quantum nature of the constituents begin to be important and the properties strongly depend on the size or more precisely on the number of atoms. In other words, above a size of a few nanometers the energy of the electronic levels, determined by the high density of the free carriers, is lower than the thermal excitation energy $k_B T$ at room temperature [2, 46].

1.2.1 Metal-Radiation Interaction

In general, metals have three different behaviours depending on the frequency of the em wave. For low-frequency radiation, such as microwaves or far-infrared radiation, electromagnetic waves do not propagate through metals that are very reflective. Only a negligible fraction of radiation penetrates the metal to a depth called *skin depth*. By increasing the frequency and approaching the visible spectrum, the penetration of the em field into the metal increases and the dissipation becomes considerable. Finally, going to ultraviolet frequencies, a metal behaves as a dielectric allowing the propagation of em radiation. However, while alkaline metals become transparent to UV radiation, noble metals, such as gold and silver, have a strong adsorption in the UV range due to the interband transitions.

In order to interpret this behaviour, the dispersive properties can be described via a complex dielectric function $\varepsilon(\omega)$, which provides the basis of most optical phenomena. To evaluate em response of metals, Maxwell's equations are the starting point

$$\nabla \cdot \mathbf{D} = \rho_{ext} \tag{1.30a}$$

$$\nabla \cdot \mathbf{B} = 0 \tag{1.30b}$$

$$\nabla \times \mathbf{E} = -\frac{\partial \mathbf{B}}{\partial t} \tag{1.30c}$$

$$\nabla \times \mathbf{H} = \frac{\partial \mathbf{D}}{\partial t} + \mathbf{J_{ext}} \tag{1.30d}$$

where $\mathbf{E}$ is the electric field, $\mathbf{D}$ the electric displacement vector, $\mathbf{H}$ the magnetic field, $\mathbf{B}$ the magnetic induction and ρ_{ext} and $\mathbf{J_{ext}}$ are, respectively, the external charge and current current density vector.

Polarization $\mathbf{P}$ and magnetization $\mathbf{M}$ link the four fields via

$$\mathbf{D} = \varepsilon_0 \mathbf{E} + \mathbf{P} \tag{1.31a}$$

$$\mathbf{H} = \frac{1}{\mu_0} \mathbf{B} - \mathbf{M} \tag{1.31b}$$

where ε_0 and μ_0 are the electric permittivity and the magnetic permeability of vacuum, respectively.

In the following we will take into account only electric polarization effects, because in our case where only non-magnetic media will be considered, $\mathbf{M}$ is neglected.

Since the polarization $\mathbf{P}$ is related to the internal charge density ρ_{int} by $\nabla \cdot \mathbf{P} = -\rho_{int}$, charge conservation $\nabla \cdot \mathbf{J}_{int} = -\frac{\partial \rho_{int}}{\partial t}$ implies that

$$\mathbf{J}_{int} = \frac{\partial \mathbf{P}}{\partial t} \tag{1.32}$$

Polarization $\mathbf{P}$ represents the electric dipole moment per unit volume inside the material and, in a homogeneous, linear and isotropic dielectric medium, it is related to the electric field with a linear relationship [47]

$$\mathbf{P} = \varepsilon_0 \chi \mathbf{E} \tag{1.33}$$

where χ is the dielectric susceptibility, which is related to the *dielectric function* by $\varepsilon = 1 + \chi$.

Therefore, the electric displacement vector in eq. 1.31a can be written as

$$\mathbf{D} = \varepsilon_0 \varepsilon \mathbf{E} \tag{1.34}$$

This it is correct for linear media without temporal or spatial dispersion. Unfortunately these assumptions are not satisfied by metals whose response strongly depends on frequency. Taking into account the non-locality in time and space, the linear $(\mathbf{r}, t)$ relationship is generalized as

$$\mathbf{D}(\mathbf{r}, t) = \varepsilon_0 \int dt' d\mathbf{r}' \varepsilon(\mathbf{r} - \mathbf{r}', t - t') \mathbf{E}(\mathbf{r}', t') \tag{1.35}$$

In the frequency domain, by Fourier transform, equations (1.35) are simplified significantly by turning the convolutions into multiplication

$$\mathbf{D}(\mathbf{K}, \omega) = \varepsilon_0 \, \varepsilon(\mathbf{K}, \omega) \, \mathbf{E}(\mathbf{K}, \omega) \tag{1.36}$$

where $\mathbf{K}$ is the wavevector and ω the angular frequency of the individual plane-wave components of the field.

In this context another approximation can be done, since we will study the optical properties of the samples in the near-infrared (NIR), visible (VIS) and ultraviolet (UV) spectral regions. It is possible to consider $\varepsilon(\mathbf{K} = \mathbf{0}, \omega) = \varepsilon(\omega)$ in the limit of *spatially local* response, namely as long as the wavelength λ in the material is significantly longer than all the characteristic dimensions, such as unit cell size or electron mean free path. In general this condition is satisfied up to the UV region, $\lambda \gtrsim 100$ nm.

$\varepsilon(\omega)$ is in general a complex function of ω, which is a real number, and can be expressed as $\varepsilon(\omega) = \varepsilon_1(\omega) + i\varepsilon_2(\omega)$. The dielectric function is also related to the complex *refractive index* according to the expression:

$$\tilde{n}(\omega) = \sqrt{\varepsilon(\omega)} \tag{1.37}$$

$\tilde{n}$ is also a complex function of ω, and can be expressed as $\tilde{n}(\omega) = n(\omega) + ik(\omega)$, where the *real refractive index* $n(\omega)$ and the *extinction coefficient* $k(\omega)$ are the measurable quantities. From eq. 1.37 the components, ε_1 and ε_2, of the dielectric function are linked with n and k as

$$\varepsilon_1 = n^2 - k^2 \tag{1.38a}$$

$$\varepsilon_2 = 2nk \tag{1.38b}$$

$$n^2 = \frac{\varepsilon_1}{2} + \frac{1}{2}\sqrt{\varepsilon_1^2 + \varepsilon_2^2} \tag{1.38c}$$

$$k = \frac{\varepsilon_2}{2n} \tag{1.38d}$$

Moreover, the extinction coefficient $k(\omega)$ determines the optical absorption of em waves propagating inside the material and it is linked to the *absorption coefficient* α in the Lambert-Beer's law by

$$\alpha(\omega) = \frac{2k(\omega)\omega}{c} \tag{1.39}$$

Dielectric Function Model

It can be seen that most of the information on metal-radiation interactions is given by the dielectric function $\varepsilon(\omega)$. Let's now see how simple analytical models can give us a theoretical description that well approximates the data in the range of our interest. A big advantage of having an analitycal formula for dielectric function $\varepsilon(\omega)$ is that it can be easily included in numerical solvers for Maxwell's equations, such as the finite-difference time-domain (FDTD) scheme [49].

The model called *Drude-Lorentz model* is an extension, proposed by H. A. Lorentz, to the more simple *Drude model* or *free electron gas model* by P. K. L. Drude. Drude model assumes a density of free electrons moving through a fixed lattice formed by positive ions. Moreover, electron-electron and electron-core interactions are considered negligible and so electrons can be treated as free particles. However, taking into account the *effective mass m* of each electron, some aspects of the band structure can be included.

In analogy with the kinetic theory, during the motion in the metal, electrons collide with positive ions with a characteristic *collision frequency* $\gamma = \frac{1}{\tau}$, where τ is know as the *relaxation time* of the free electron gas.

Despite these strong assumptions, this model gives good results in a wide range of frequencies, up to the interband transitions of the metal. For alkaline metals this happens at the UV range, but for noble metals the interband transitions become important in the visible range, limiting the validity of the model. Specifically, for copper and gold this occurs at about $2\,\mathrm{eV}$ ($\lambda \sim 600\,\mathrm{nm}$), for silver at about $4\,\mathrm{eV}$ ($\lambda \sim 300\,\mathrm{nm}$).

The Drude model was then extended by Lorentz in order to overcome the disagreement found in the energy range of interband transition. Lorentz took into account the contribution of bounded electrons, adding a harmonic term to the motion equation

$$m\ddot{\mathbf{x}} + m\gamma\dot{\mathbf{x}} + m\omega_0^2\mathbf{x} = -e\mathbf{E} \tag{1.40}$$

(a) Silver

(b) Gold
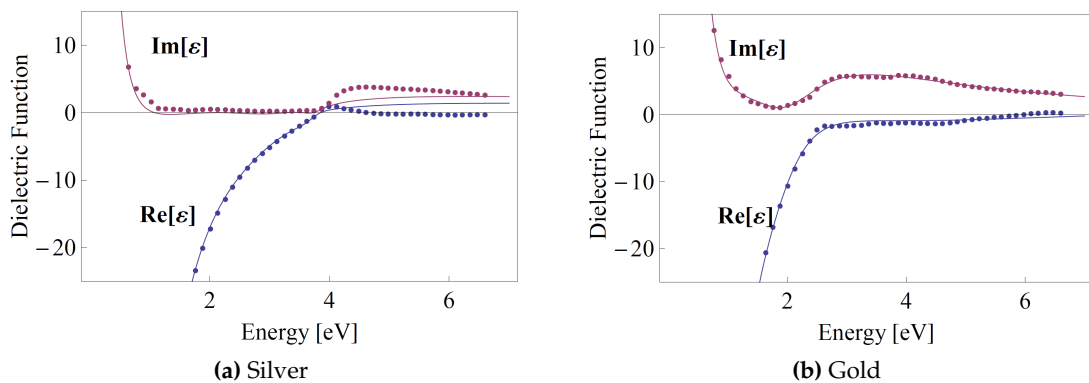
Figure 1.5: Best fits to the experimental data from Johnson and Christy [48] (dots) obtained with the Drude-Lorentz model, for silver **(a)** and gold **(b)**.

where ω_0 represents a resonance frequency that corresponds to a particular interband transition with $\hbar\omega_0$ energy. When more than one transition is considered, we will have a system with the same number of non-homogeneous differential equations like (1.40), each of them with its own resonance frequency ω_j and collision frequency γ_j.

Then, from the definition of macroscopic polarization vector **P**, the dielectric function in this revised model results

$$\varepsilon(\omega) = \varepsilon_\infty - \frac{\omega_p^2}{\omega^2 + i\gamma\omega} + \sum_{j=1}^{N} \frac{A_j}{\omega_j^2 - \omega^2 + i\gamma_j\omega} \tag{1.41}$$

where A_j are free parameters which change depending on the considered metal.

$$\omega_p = \sqrt{\frac{n\,e^2}{m\varepsilon_0}} \tag{1.42}$$

is the *plasma frequency*, where n is the *free electron density* and ε_∞ is a parameter that varies between 1 and 10. In particular, ε_∞ takes into account the presence of a highly polarized environment caused by d electrons near the Fermi surface.

Figure 1.5 shows an excellent agreement between the experimental data from Johnson and Christy [48] and the analytical dielectric function $\varepsilon(\omega)$, determined with the Drude-Lorentz model, performed by Hao and Nordlander [50] considering 4 interband transitions.

1.2.2 Localized Surface Plasmon

Let's consider a gas of free electrons in oscillatory motion, then we can define a *plasmon* as a quantum of these free electron gas density oscillations. We can distinguish three types of plasmons:

(a) **Volume plasmons** (fig. 1.6a) occur in a bulk metal. They are travelling waves with a frequency ω_p given by eq. 1.42. However, due to their its longitudinal nature, volume plasmons cannot couple to em radiation and are excited only by charged particle impact.

(b) **Surface plasmon polaritons** (SPP) (fig. 1.6b), represented in fig. 1.6b, are em excitations evanescently confined in a sub-wavelength spatial region in the perpendicular direction of the interface between a metal and a dielectric where they propagate. These em surface waves arise from the coupling of em field and the free electron gas in the metal and have a characteristic frequency $\omega_{sp} = \frac{\omega_p}{\sqrt{1+\varepsilon_m}}$, called *surface plasmon*

<table>
<tr><td>**(a)** Volume Plasmon</td><td>**(b)** Surface Plasmon Polariton</td><td>**(c)** Localized Surface Plasmon</td></tr>
</table>
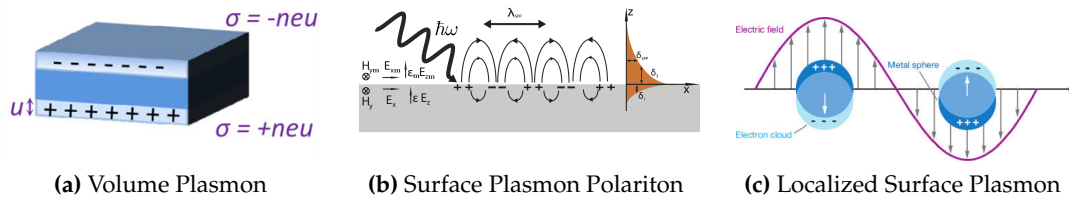
Figure 1.6: Comparative sketches of **(a)** volume plasmon, **(b)** surface plasmon polariton and **(c)** localized surface plasmon.

frequency, where ε_m is the dielectric function of the dielectric medium.

However, to excite SPP phase-matching is needed. In fact, due to their bound nature, from the Helmholtz equation, the dispersion relation of SPP excitations results $\beta = k_0\sqrt{\frac{\varepsilon\varepsilon_m}{\varepsilon+\varepsilon_m}}$, where $k_0 = \omega/c$ is the wavevector in the vacuum. Since $\beta > k$, SPP excitations correspond to the part of the dispersion curves lying to the right of the respective light line, as shown in fig. 1.7. Thus, special phase-matching techniques such as grating or prism coupling are required for their excitation.

(a) Drude model for ε.

(b) Experimental data obtained by Johnson and Christy [48] for ε.
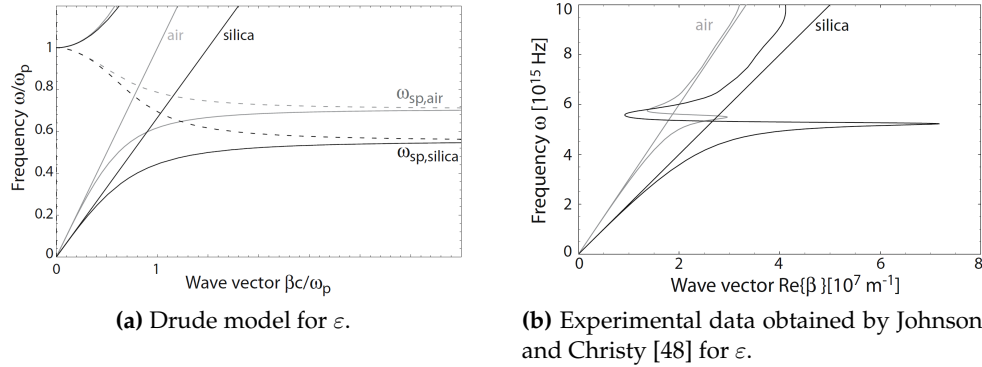
Figure 1.7: Dispersion relation of SSPs at silver/air (gray curve) and silver/silica (black curve) interface, for different estimations of the dielectric function.

(c) **Localized surface plasmons** are non-propagating excitations of the free electron gas that arise under three-dimensional confinement in a nanoparticle coupled with the em field, as sketched in fig. 1.6c. The nanoparticle exerts a restoring force induced by the depolarization field on the electrons, therefore the system behaves like a forced-damped harmonic oscillator. This behaviour produces a resonance phenomenon called *localized surface plasmon resonance* (LSPR), which generates an amplification on the electric field inside and in the immediate vicinity (near-field zone) of the nanoparticle. This amplification, called *local field enhancement*, is the basis for most of applications in plasmonics, especially for plasmonic nanolasers.

The LSPR depends on many factors as size, shape, electron density and effective mass,of the nanostructures and the dielectric function of the medium where the particles are embedded.

Unfortunately, an analytical approach for this problem is made difficult by all these dependences. Only for spherical or spheroidal particles an analytical solution was obtained. For non-interacting spherical particles in a non-absorbing medium, Mie theory gives a full treatise of scattering and absorption [51–53] and Gans made a generalisation for spheroidal particles [54]. Out of this conditions, i.e., for different shapes or interacting particles, numerical approaches are required due to the problem complexity.

Quasi-Static Regime

The *quasi-static regime approximation* consists in considering a nanoparticle much smaller than λ of the impinging light. The spatial variation and the phase difference of the electric field across the nanoparticle can be neglected, thus considering the nanoparticle immersed in uniform electric field that varies in time.

Consider a homogeneous and isotropic sphere of radius a, as shown in figure 1.8, placed in an isotropic and non-absorbing environment with dielectric constant ε_m. A static electric field $\mathbf{E} = E_0\hat{\mathbf{z}}$ along the $\mathbf{z}$ direction surrounds the sphere. In an electrostatic approach, the Laplace equation results to be $\nabla^2\Phi = 0$ and taking into account the spherical symmetry, the electric potential Φ will be a linear combination of the Legendre polynomials. Then, imposing the boundary and continuity conditions on the particle surface, the electric field is calculated by the relation $\mathbf{E} = -\nabla\Phi$ and results

$$\mathbf{E_{in}} = \frac{3\varepsilon_m}{\varepsilon + 2\varepsilon_m}\,\mathbf{E_0} \tag{1.43a}$$

$$\mathbf{E_{out}} = \mathbf{E_0} + \frac{3\mathbf{n}(\mathbf{n}\cdot\mathbf{p}) - \mathbf{p}}{4\pi\varepsilon_0\varepsilon_m}\,\frac{1}{r^3} \tag{1.43b}$$

where $\mathbf{n}$ is the unit vector in the direction of the point of interest P (fig. 1.8) perpendicular to the sphere surface and the *dipole momentum* $\mathbf{p}$ is

$$\mathbf{p} = 4\pi\varepsilon_0\varepsilon_m a^3\,\frac{\varepsilon - \varepsilon_m}{\varepsilon + 2\varepsilon_m}\,\mathbf{E_0} \tag{1.44}$$

$\mathbf{E}_{out}$ describes the superposition of the applied field and that of a dipole located at the particle center. Moreover, it is possible to define the *polarizability* α via $\mathbf{p} = \varepsilon_0\varepsilon_m\,\alpha\,\mathbf{E_0}$ and thus in quasi-static approximation it results

$$\alpha_{qs} = 4\pi a^3\,\frac{\varepsilon - \varepsilon_m}{\varepsilon + 2\varepsilon_m} \tag{1.45}$$

It can be observed from this equation that if the imaginary part, $Im[\varepsilon(\omega)]$, of the dielectric function is negligible, the polarizability α diverges under the *Fröhlich condition*:

$$Re[\varepsilon(\omega)] = -2\varepsilon_m \tag{1.46}$$

When the Fröhlich condition is fulfilled, a resonant mode occurs which is associated to the dipole surface plasmon, called *Localized Surface Plasmon Resonance* (LSPR). It is also easy to find that, under this condition, $\varepsilon(\omega) \sim \varepsilon_1(\omega) = 1 - \omega_p^2/\omega^2$, and therefore from equation 1.46, it follows

$$\omega_{LSPR} = \frac{\omega_p}{\sqrt{1 + 2\varepsilon_m}} \tag{1.47}$$

where ω_p is the plasma frequency.

We note that the resonance mode implies an enhancement of both internal and external dipolar fields. From equations 1.43 the *local field factor*, f, can be defined via $\mathbf{E_{in}} = f\,\mathbf{E_0}$. f represents the enhancement factor inside the sphere and in this case it
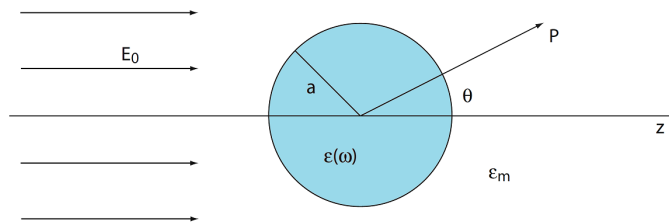
Figure 1.8: Scheme of the geometry used in the model

results to be $f = \frac{3\varepsilon_m}{\varepsilon + 2\varepsilon_m}$.

Moreover, we note that outside the sphere the field decreases quickly, as r^{-3}, determining the properties in the *near-field* zone.

It is interesting to note that considering an electric field $\mathbf{E}(\mathbf{r}, t) = \mathbf{E_0}e^{-i\omega t}$ with a harmonic time dependence and consequently the dipole momentum $\mathbf{p}(t) = \varepsilon_0\varepsilon_m\alpha\mathbf{E_0}e^{-i\omega t}$, the polarizability α does not change, remaining the same as in the electrostatic case (eq. 1.45).

Remind complete electric $\mathbf{E}(t) = \mathbf{E}e^{-i\omega t}$ and magnetic $\mathbf{H}(t) = \mathbf{H}e^{-i\omega t}$ fields induced by an oscillating electric dipole can be written [55] as

$$\mathbf{E_{dip}} = \frac{1}{4\pi\varepsilon_0\varepsilon_m}\left\{k^2(\hat{\mathbf{r}} \times \mathbf{p}) \times \hat{\mathbf{r}}\,\frac{e^{ikr}}{r} + [3\hat{\mathbf{r}}(\hat{\mathbf{r}} \cdot \mathbf{p}) - \mathbf{p}]\left(\frac{1}{r^3} - \frac{ik}{r^2}\right)e^{ikr}\right\} \tag{1.48a}$$

$$\mathbf{H_{dip}} = \frac{ck^2}{4\pi}(\hat{\mathbf{r}} \times \mathbf{p})\,\frac{e^{ikr}}{r}\left(1 - \frac{1}{ikr}\right) \tag{1.48b}$$

where $k = 2\pi/\lambda$ is the wavevector and the position $\mathbf{r} = r\hat{\mathbf{r}}$.

The cross-sections for scattering σ_{sca} and absorption σ_{abs} can be extrapolated taking into account the dipole em field in equations (1.48) and considering *Poynting vector* $\mathbf{S} = \frac{1}{\mu_0}\mathbf{E} \times \mathbf{H}$. They are also linked to the polarization α by the following equations [52]:

$$\sigma_{sca} = \frac{k^4}{6\pi}|\alpha|^2 = \frac{8\pi}{3}k^4a^6\left|\frac{\varepsilon - \varepsilon_m}{\varepsilon + 2\varepsilon_m}\right|^2 \tag{1.49a}$$

$$\sigma_{abs} = k\,\text{Im}[\alpha] = 4\pi ka^3\,\text{Im}\left[\frac{\varepsilon - \varepsilon_m}{\varepsilon + 2\varepsilon_m}\right] \tag{1.49b}$$

Therefore, the *extinction cross-section* for a sphere of volume V and dielectric function $\varepsilon = \varepsilon_1 + i\varepsilon_2$ in quasi-static approximation is

$$\sigma_{ext} = \sigma_{sca} + \sigma_{abs} = 9\,\frac{\omega}{c}\,\varepsilon_m^{3/2}\,V\,\frac{\varepsilon_2}{[\varepsilon_1 + 2\varepsilon_m]^2 + \varepsilon_2^2} \tag{1.50}$$

Finally, it can be noted that during the treatment no restriction was assumed on the material of the sphere, therefore the results are valid also for a dielectric sphere, even if no resonance phenomenon persists since the dielectric function of a dielectric is always positive and the Fröhilch condition will never be met.

If we consider larger particles ($a \gtrsim \lambda/10$), where the variation of the electric field phase across the nanosphere is no longer negligible, the quasi-static approximation will no longer be valid. In this respect, the *modified long-wavelength approximation* (MLWA), allow us to extend the quasi-static approximation to larger particles. This consists in a linear expansion over the size parameter ka of the dipolar electric field up to power k^3 [56].

Then the polarizability in MLWA can be writetten [57], taking in to account the one in quasi-static approximation (1.45), as

$$\alpha_{MLWA} = \frac{\alpha_{qs}}{1 - \frac{k^2}{a}\alpha_{qs} - \frac{2}{3}ik^3\alpha_{qs}} \tag{1.51}$$

The first term at the denominator, proportional to k^2, is linked to the *dynamic depolarization* respons [56] and describes the effect of the electric field produced by the charge

distribution delay between the two opposite sides of the sphere. Such depolarization field, since is proportional to k^2, reduces the importance of the $\text{Im}[\varepsilon(\omega)]$, increasing the polarization. The second term, purely imaginary, counteracts this increase. It is related to the *radiation damping* due to the radiative decay of the LSP [58], and becomes increasingly important for larger particles. It should be noted that both these effects cause a redshift of the LSPR when the particle dimension increases.

For an arbitrary size a fully multipolar expansion has to be considered as calculated by G. Mie [51]. However, the disadvantage of this theory is that it does not provide a way to build simple model for the response of arrays of particles.

Finally, how we can note from extinction cross-section σ_{ext} (eq. 1.50) and Fröhlich condition (eq. 1.46), LSPR depends on composition, shape and size of the particle, and on the surrounding medium and polarization of the incident light for non-spherical particles. Moreover, high field enhancement arises in the near-field zone ($\mathbf{E} \propto r^{-3}$). This entails a light confinement at the nanoscale, below the diffraction limit, making the nanoparticle a nanocavity. However, the quality factor $Q = \omega_{LSPR}/\Delta\omega \simeq \lambda_{LSPR}/\Delta\lambda$ of LSPRs is not too high, of the order of some tens, due to the high losses in the metal.

But another effect appears by the presence of a cavity and is called *Purcell Effect* [59, 60]. According with the Fermi's golden rule, Purcell effect describes the modification of the radiative decay rate by the presence of a cavity. As seen previously for LSPRs, a nanoparticle acts as an optical resonator in the vicinity of its surface. So we expect that Purcell effect arises again.

This phenomenon is explained and modelled as the modification of the radiative $\gamma_{sp} = 1/\tau_{sp}$ decay rate of a factor F, which, in according to the Purcell effect [59], can be written as

$$F = \frac{3Q\lambda^3}{4\pi^2 V_{mode}(2n)^3} \tag{1.52}$$

where V_{mode} is the volume mode of the cavity, which, for us, is the nanoparticle. Thanks to the very small volume mode of the nanoparticles, the Purcell factor can become quite high, compensating for the small Q-factor, and making the nanoparticles suitable to act as a laser cavity.

Since this modification is caused by the electric field, Purcell factor depends on the distance from the surface of the nanoparticle. However, if we consider an emitter too close to the nanoparticle, a quenching phenomenon occurs [60]. This quenching phenomenon is due to the non-radiative energy transfer that, for short distances, becomes important thereby quenching the fluorescence of the molecule. The principal contribute of this non-radiative energy transfer is due by Förster resonant energy transfer (FRET), that describes mechanism of energy transfer between donor molecules and metal surface instead of an organic acceptor. This effect of donor-acceptor match changes also the radiative rate of the molecules, modifying quantum efficiency η of the system. Regarding our system these phenomena can occur near to the plasmonic nanostructures and we have to take into account.

1.2.3 Plasmonic nanoparticle arrays

Placing plasmonic nanostructures in an ordered arrangement can lead to switch on plasmonic collective modes mediated by the lattice. As we will see in this section for metallic nanoparticle array, near the diffraction order of the lattice where radiating energy changes to evanescent character, dipolar interactions lead to the emergence of a new nar-

(a) Direct lattice

(b) Reciprocal lattice
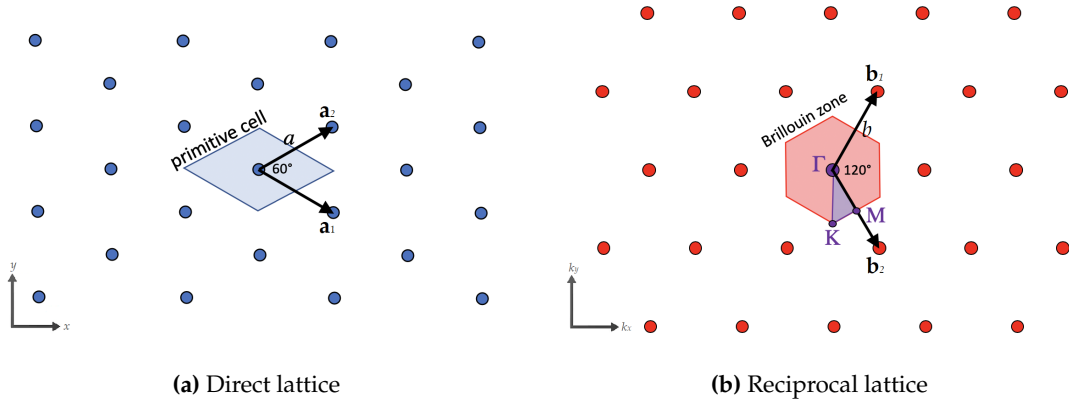
Figure 1.9: Schematic representation of the direct and reciprocal hexagonal lattice.

row linewidth plasmonic resonance [61]. This resonance is known as *Surface Lattice Resonance* (SLR). The interaction of plasmonic nanoparticles with this collective extended modes leads to the suppression of radiative damping, which is the dominant contribution to the plasmon resonance linewidth [62], making plasmonic system based on this collective resonances one possible way to minimize losses.

The properties of SLRs, which derive from the coupling of LSPRs, generally depend on the same parameters: shape, size and composition of nanoparticles, as well as on the surrounding medium and polarization of the incident radiation. Furthermore, due to their collective behaviour, SLRs depend strongly on the interparticle distance and on the long-range order in the lattice.

SLRs can be connected to Wood's anomalies in diffraction gratings [63]. Wood's anomalies, studied by R. W. Wood at the beginning of the last century [64], are due to two distinct phenomena related to each other and subsequent interpreted by Lord Rayleigh [65] and U. Fano [66].

Rayleigh Anomaly Modes

The first phenomenon, called *Rayleigh anomalies* is purely geometric and is correlated to a discontinuous change in the reflectivity, when the incident light has wavelength and angle determined by the grating period, corresponding to the condition where a diffracted wave propagates in the plane of the array. Therefore these anomalies are strongly linked with the appearance of diffraction orders. These satisfy the Bragg condition in the lattice plane that can be written as

$$\mathbf{k}_{//\mathbf{d}} = \mathbf{k}_{//\mathbf{i}} + \mathbf{G}_{nm} \tag{1.53}$$

$\mathbf{k}_{//\mathbf{d}}$ is the parallel component to the lattice plane of the diffracted wavevector, with $|\mathbf{k}_{//\mathbf{d}}| = 2\pi n_{eff}/\lambda$, where n_{eff} is the effective refractive index defining phase velocity of the diffracted waves on lattice plane (i.e., Rayleigh anomalies); $\mathbf{k}_{//\mathbf{i}}$ is the in-plane component of the wavevector of the incident light, with $|\mathbf{k}_{//\mathbf{i}}| = (2\pi/\lambda)\sin\theta$ where θ is the angle formed between the normal to the lattice plane and the wavevector of the incident wave; $\mathbf{G}_{nm}$ is the vector of the reciprocal lattice [67].

The reciprocal lattice is the corresponding lattice in the momentum space (or *k-space*) of the direct lattice, related to it by Fourier transform. The reciprocal vectors $\mathbf{G}$ have to obey to $\mathbf{R} \cdot \mathbf{G} = 2\pi N$ where $N \in \mathbb{Z}$ and $\mathbf{R}$ is the vector in the real space. The case
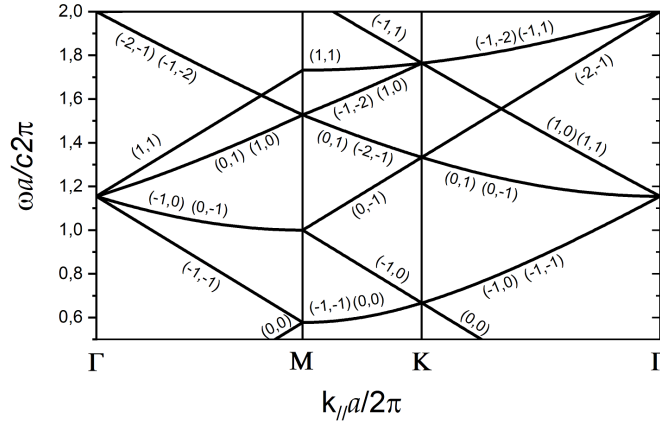
Figure 1.10: Example of Rayleigh anomalies for a two-dimensional hexagonal lattice in the highest symmetry identified by the critical points Γ, M and K.

of our interest is a two-dimensional hexagonal lattice with lattice constant a, showed in figure 1.9a, so by defining $\mathbf{R}_{ij} = i\mathbf{a}_1 + j\mathbf{a}_2$ and $\mathbf{G}_{nm} = n\mathbf{b}_1 + m\mathbf{b}_2$ where i, j, n, m are integers, we can write

$$
\mathbf{b}_1 = 2\pi \frac{\mathbf{a}_2 \times \hat{z}}{\mathbf{a}_1 \cdot (\mathbf{a}_2 \times \hat{z})} = \left(\frac{1}{\sqrt{3}}, 1\right) \frac{2\pi}{a} \qquad \text{with} \qquad \mathbf{a}_1 = \left(\frac{\sqrt{3}}{2}, \frac{1}{2}\right) a
$$

$$
\mathbf{b}_2 = 2\pi \frac{\hat{z} \times \mathbf{a}_1}{\mathbf{a}_2 \cdot (\hat{z} \times \mathbf{a}_1)} = \left(\frac{1}{\sqrt{3}}, -1\right) \frac{2\pi}{a} \qquad \qquad \mathbf{a}_1 = \left(\frac{\sqrt{3}}{2}, -\frac{1}{2}\right) a
$$

(1.54)

The corresponding reciprocal lattice is shown in figure 1.9b, where $b = |\mathbf{b}_1| = |\mathbf{b}_2| = 4\pi/\sqrt{3}a$. The Wigner-Seitz cell or first Brillouin zone is also highlighted: due to the periodicity, energy eigenstates for a photon in a crystal can be written as Bloch waves and can be completely characterized within the Brillouin zone. Instead, Γ, K and M, called *critical points*, are the points of high symmetry of the system and play a particularly important role on the diffraction. n and m are called *Miller indices*. They indicate the family of lines orthogonal to the vector $\mathbf{G}_{nm} = n\mathbf{b}_1 + m\mathbf{b}_2$. Considering only (nm) lines crossing lattice points, *lattice lines*, the perpendicular distance d_{nm} between adjacent lattice lines for an hexagonal lattice is

$$
d_{nm} = \frac{2\pi}{|\mathbf{G}_{nm}|} = \frac{\sqrt{3}}{2} \frac{a}{\sqrt{n^2 - nm + m^2}}
$$

(1.55)

which is then connected to the Bragg law as

$$
2d_{nm} \sin(\theta) = n\lambda
$$

(1.56)

where θ and λ are the angle and the wavelength of an incident em wave on the crystal.

By equations (1.53) and (1.54) it is possible to obtain the dispersion relation of each diffraction order identified by the Miller indices (n, m), i.e. Rayleigh anomalies. In figure 1.10 is shown an example of this dispersion relation for a two-dimensional hexagonal lattice in the highest symmetry direction identified by the critical points Γ, K and M.

Coupled Dipole Method

We have seen how Rayleigh anomalies emerge from a pure geometric factor related to the periodicity of the system and therefore they can also be present in a dielectric array, not having made any assumption on the material. Instead, the second aspect mentioned before was correctly interpreted for the first time by U. Fano who suggested that the origin of anomalies could be found in the excitation of surface waves. [68]. For a plasmonic nanoparticle array, SLRs derive from the coupling of the diffracted waves on the lattice plane (Rayleigh anomalies) and the LSPR of each particle. The *coupled dipole method* (CDM), it possible to show how geometric arrangement in a ordered array of metallic nanoparticles coupled by dipole interaction can led to the formation of these collective resonance modes [69, 70]. A dipolar interaction is considered between the particles placed in a periodic arrangement and it is taken in to account the modified polarizability α_{CDM} which describes the response of the system to an em field.

Let's consider an array of N spherical nanoparticles at positions $\mathbf{r}_i$ and with polarizabilities α_i described by equation (1.51) assuming MLWA for more generality. The dipole momentum of each particle will be given by $\mathbf{p}_i = \varepsilon_0 \varepsilon_m \alpha_i \, \mathbf{E}_{\mathbf{loc},i}$. The local field in the position $\mathbf{r}_i$ of the i-particle is given by the superimposition of the incident field $\mathbf{E}_{\mathbf{inc},i}$ plus the retarded induced field $\mathbf{E}_{\mathbf{dip},i}$ of the other $N-1$ dipoles, i.e. $\mathbf{E}_{\mathbf{loc},i} = \mathbf{E}_{\mathbf{inc},i} + \mathbf{E}_{\mathbf{dip},i}$. Therefore, the dipole momentum of the i-particle becomes

$$\mathbf{p}_i = \varepsilon_0 \varepsilon_m \alpha_i \, \mathbf{E}_{\mathbf{loc},i} = \varepsilon_0 \varepsilon_m \alpha_i (\mathbf{E}_{\mathbf{inc},i} + \mathbf{E}_{\mathbf{dip},i}) = \varepsilon_0 \varepsilon_m \alpha_i (\mathbf{E}_0 \, e^{i\mathbf{k}\cdot\mathbf{r}_i} - \sum_{\substack{j=1 \\ j \neq i}}^{N} A_{ij} \cdot \mathbf{p}_j) \quad (1.57)$$

with i and j run from 1 to N. It has been assumed an incident plane wave $\mathbf{E}_{\mathbf{inc},i} = \mathbf{E}_0 \, e^{i\mathbf{k}\cdot\mathbf{r}_i}$ with wavevector $k = 2\pi/\lambda$.

The dipole contribution $\mathbf{E}_{\mathbf{dip},i}$ on the i-particle is the result of the sum of electric field induced by every other dipole present in the lattice, described as $A_{ij} \cdot \mathbf{p}_j$, where A_{ij} is colled *dipole interaction matrix* [70].

Each j-term of $A_{ij} \cdot \mathbf{p}_j$ represents the electric field in $\mathbf{r}_i$ deriving from the j-dipole placed in the position $\mathbf{r}_j$, and is given by

$$A_{ij} \cdot \mathbf{p}_j = k^2 \, e^{ikr_{ij}} \frac{\mathbf{r}_{ij} \times (\mathbf{r}_{ij} \times \mathbf{p}_j)}{r_{ij}^3} + e^{ikr_{ij}} \left(1 - ikr_{ij}\right) \frac{r_{ij}^2 \mathbf{p}_j - 3\mathbf{r}_{ij}(\mathbf{r}_{ij} \cdot \mathbf{p}_j)}{r_{ij}^5} \quad (1.58)$$

where $(j \neq i)$ and $\mathbf{r}_{ij} = \mathbf{r}_j - \mathbf{r}_i$ is the vector from j-particle to i-particle.

The expression (1.57) can be written in a more compact form as

$$A'\mathbf{p} = \varepsilon_0 \varepsilon_m \mathbf{E} \quad (1.59)$$

where the diagonal terms of the matrix are defined as $A'_{ii} = 1/\alpha_i$ and the terms out of the diagonal are equal to the dipole interaction matrix terms A_{ij} in equation (1.58).

The polarization vector $\mathbf{P}$ can therefore be obtained by solving the system of $3N$ linear equations defined by eq. (1.59).

An analytical solution can be obtained for the system of equations by considering an incident plane wave perpendicular to the lattice plane and an infinite matrix of identical elements that guarantees the same polarization for each particle. By these assumptions, the polarizability of each particle results

$$\alpha_{CDM} = \frac{1}{1/\alpha_{MLWA} - S} \quad (1.60)$$
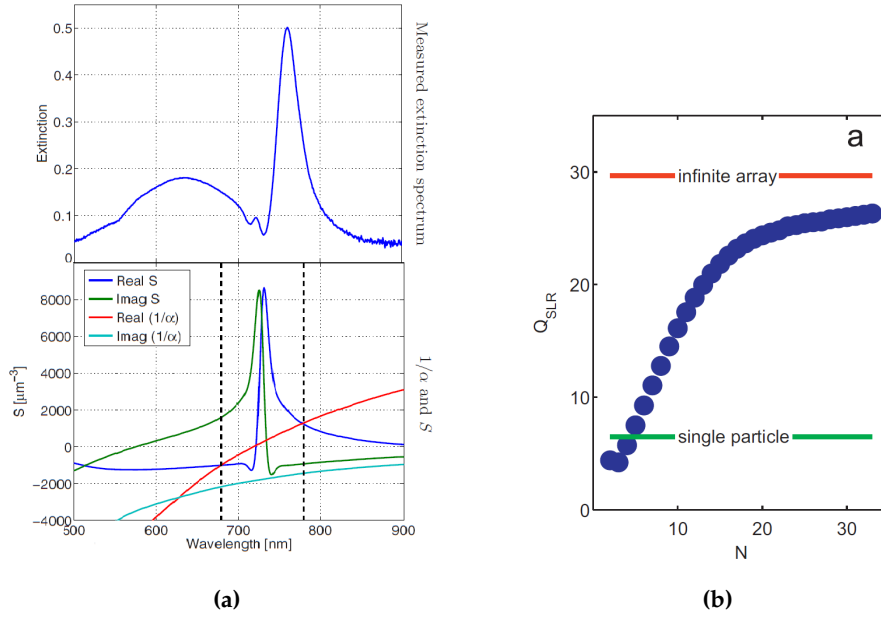
Figure 1.11: (a) Measured extinction spectrum (above) and simulated array factor and polarizability α_{MLWA} (below) for a hexagonal array of silver disks [16]; **(b)** Simulated Q-factor of SLRs as a function of the number of nanoparticles (N) along each side [71].

where the *array factor S* is defined as

$$S = \sum_{j \neq i} \left[\frac{(1 - ikr_{ij})(3\cos^2\theta_{ij} - 1)}{r_{ij}^3} + \frac{k^2 \sin^2\theta_{ij}}{r_{ij}} \right] e^{ikr_{ij}} \tag{1.61}$$

θ_{ij} identifies the angle between position vector $\mathbf{r}_{ij}$ and polarization of j-particle $\mathbf{p}_j$.
S depends only on particles separation and the kind of lattice, i.e. $\mathbf{R}_{ij}$ defined in the previous section.

Once α_{CDM} is calculated, the total extinction cross-section $\sigma_{TOT,ext}$ can be estimate by the superimposition of each dipole contributions, given by equations (1.49) and (1.50).

From (1.60) the polarizability α_{CDM} has a maximum when

$$Re[1/\alpha_{MLWA}] = Re[S] \tag{1.62}$$

This condition is associated with the rise of a resonant mode called *Surface Lattice Resonance* (SLR).

In Figure 1.11a an experiment conducted by R. W. Humphrey and A. D. Barnes [16] shows the agreement between the maximum condition (1.62) of equation (1.61) calculated numerically and the relative SLR peak in the extinction spectrum of a hexagonal array of spherical nanoparticles. Instead Figure 1.11b shows simulated Q-factor of SLRs as a function of the number of nanoparticles (N) along each side [71].

As we shall see, one of the most important applications of this resonance phenomenon is the possibility of making laser light emerge from the spectral and spatial coupling with an emitter. This is in fact made possible by the photonic-plasmonic coupling underlying the existence of the SLR mode.

1.3 Plasmonic Nanolasers

In the following, we will discuss how a plasmonic array, in our case a two-dimensional array of metallic nanostructures, can replace an optical cavity thus creating a plasmonic nanolaser, thus taking a step towards the miniaturization of laser devices below the diffraction limit.

The idea of using a nanoparticle array to obtain directional emission was proposed for split-ring resonators at infrared wavelengths about 10 years ago [17]. However, plasmonic nanolasers have recently been demonstrated for different geometries, as discussed in the Introduction section . The first demonstration dates back to 2012 by Suh and Odom et al. [12] with gold nanobowties arranged in a square lattice coupled with a dye (IR140) in polyurethane, exhibiting a laser emission at a wavelength of 873 nm.

Plasmonic nanolasers use SPP and LSP to squeeze light into volumes smaller than the wavelength. Owing to the LSPRs, nanoparticles are able to localize three-dimensionally the EM field within tens of nanometers from their surface, as we have seen in sec 1.2. A gain medium close to the nanoparticles in the excited state by the pump process, instead of emitting photons can transfer energy to the LSPR of the nanoparticles in a non-radiative way (fig. 1.12). These transitions are stimulated by the SPs already in the nanosystem and the stimulated nature of this non-radiative energy transfer generates a copious number of coherent surface plasmons in a single mode. Therefore, the energy accumulated in the plasmon oscillations can be re-emitted generating a laser emission. Moreover, plasmonic nanolasers that exploit LSR or SPP as a cavity present ultra-fast modulation, in the femtosecond time scale, due to the fast non-radiative decay of the plasmons [73].

When nanostructures, acting as resonant cavities, are placed in a periodic arrangement, the plasmonic nanolaser can support directional lasing emission and efficient outcoupling due to the constructive interference between the adjacent nanoparticles [19]. Driven by the lattice modes, each nanocavity oscillates in phase and this results in a high-quality cavity mode for coupling the near-field energy into free space. This cavity mode can be associated with hybrid modes of lattice plasmons arising from the cou-
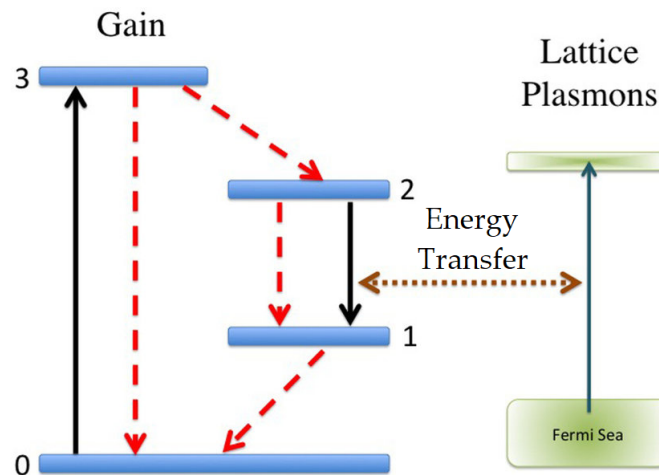
Figure 1.12: Schematic representation of the energy transfer process between gain medium and plasmonic nanosystem [72].

pling of LSPs of the single nanoparticles to diffraction modes in the periodic array. This mode can suppress radiative loss and provides an optical feedback for directional laser emission at room temperature. As previously described 1.2.3, these lattice plasmonic resonances (SLRs) are supported by metallic nanoparticles placed in a periodic array, in a medium with uniform refractive index, and their properties are determined by the single LSPRs of each nanoparticle, the lattice parameters and the environment.

We can then model the coupling between the dye and the plasmonic nanoarray in a semi-classical rate equations approach as follows.

1.3.1 Semi-classical Rate-Equations Approach

Among different approaches at this novel problem [74–80], i.e. lasing emission based on plasmonic interaction, the most interesting uses Maxwell's equation for the em field while rate-equations for the gain medium and it was proposed by Dridi and Schatz in 2013 [79].

In this semi-classical approach, it is supposed that an optically pumped transition, between the state $|i\rangle$ and $|j\rangle$, induces to a microscopic polarization μ_{ij} of the molecules of the gain medium. The macroscopic polarization $\mathbf{P}_{ij}$ is therefore given by the contribution of every microscopic polarization. However, from a quantum-mechanical approach, results that $\mathbf{P}_{ij}$ depends on the difference of population density $N_{ij}(t) = N_j(t) - N_i(t)$ and not on the total population density N. Therefore, the variation in time is taken into account in order to include absorption, stimulated and spontaneous emission effects. Moreover, the variation in time of $\mathbf{P}_{ij}(t)$, which describes the interaction between the molecules of the gain medium and the em field, can be defined by the equations of motion for driven damped oscillators, as [43, 81]

$$\frac{d^2\mathbf{P}_{ij}(t)}{dt^2} + \Delta\omega_{ij}\frac{d\mathbf{P}_{ij}(t)}{dt} + \omega_{ij}^2\,\mathbf{P}_{ij}(t) = \frac{6\pi\varepsilon_0 c^3}{\omega_{ij}^2\gamma_{ij}}\,\Delta N_{ij}(t)\,\mathbf{E}(t) \tag{1.63}$$

where ω_{ij} is the angular frequency, $\Delta\omega_{ij}$ is the bandwidth due to radiative, non-radiative and collision effects and γ_{ij} is the damping coefficient of a specific transition.
The resulting $\mathbf{P}_{ij}(t)$ modifies the electric field by the internal current density (eq. 1.32) $\mathbf{J}_{int} = \partial\mathbf{P}/\partial t$ in the Maxwell's equations (1.30), writing it as

$$\nabla \times \mathbf{E}(t) = -\mu_0\,\frac{\partial\mathbf{H}(t)}{\partial t} \tag{1.64a}$$

$$\nabla \times \mathbf{H}(t) = \varepsilon\,\frac{\partial\mathbf{E}(t)}{\partial t} + \frac{\partial\sum_{ij}\mathbf{P}_{ij}(t)}{\partial t} \tag{1.64b}$$

In this classical approach, the energy-transfer rate between the em field and the gain medium molecules is [43, 82–84]

$$\frac{dU_{ij}(t)}{dt} = \mathbf{E}(t)\cdot\frac{d\mathbf{P}_{ij}(t)}{dt} = \frac{dN_i(t)}{dt}\,\hbar\omega_{ij} \tag{1.65}$$

that is equal to the transition rate per photon energy.

Taking into account a four-level system, to describe the energy state of gain medium,

as shown in Figure 1.13a, the system of rate equations (1.20) can be written as [79]

$$\frac{dN_0(t)}{dt} = \frac{N_1(t)}{\tau_{10}} + \frac{N_3(t)}{\tau_{30}} - \frac{1}{\hbar\omega_{30}}\mathbf{E}(t) \cdot \frac{d\mathbf{P}_{30}(t)}{dt} \tag{1.66a}$$

$$\frac{dN_1(t)}{dt} = \frac{N_2(t)}{\tau_{21}} - \frac{N_1(t)}{\tau_{10}} - \frac{1}{\hbar\omega_{21}}\mathbf{E}(t) \cdot \frac{d\mathbf{P}_{21}(t)}{dt} \tag{1.66b}$$

$$\frac{dN_2(t)}{dt} = \frac{N_3(t)}{\tau_{32}} - \frac{N_2(t)}{\tau_{21}} + \frac{1}{\hbar\omega_{21}}\mathbf{E}(t) \cdot \frac{d\mathbf{P}_{21}(t)}{dt} \tag{1.66c}$$

$$\frac{dN_3(t)}{dt} = -\frac{N_3(t)}{\tau_{32}} - \frac{N_3(t)}{\tau_{30}} + \frac{1}{\hbar\omega_{30}}\mathbf{E}(t) \cdot \frac{d\mathbf{P}_{30}(t)}{dt} \tag{1.66d}$$

The electric field $\mathbf{E}(t)$ included in the equation describes the total electric field, which is the result of the contribution given by the incident radiation, the emitted radiation from the molecules and the electric field given by the nanostructures.

Furthermore, it is possible to take into account the Purcell effect, by using the Purcell factor (1.52) to modify γ_{12} in particular.

Equations 1.66 are solved by 3D *Finite-Difference Time-Domain* (FDTD) numerical technique. As a result, the population inversion ($\Delta N_{12} = N_2 - N_1$) are determined as a function of time or pump intensity and the consequent lasing emission intensity.

Figure 1.13b shows FDTD simulated results of emission (above) and population inversion (below) as a function of incidence fluence, made by Dridi and Schatz [79], exhibiting the possibility to reach lasing emission by a plasmon nanolaser.

An extension of the previous semiclassical approach takes into account the treatment of coherence effects. These are one of the causes of the evolution description incompleteness of the rate equations of gain material. The quenching due to the nanoparticles or the transfer energy between the dye molecules could cause the dephase of the dye excitation. This dephasing of emitter states can be described by the Maxwell−Liouville approach,
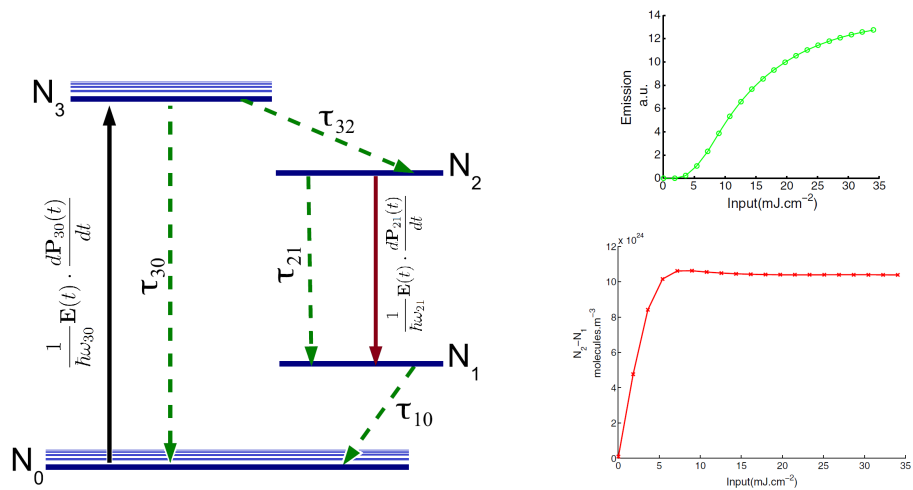
(a) Four-level diagram to describe dye molecules [79].

(b) FDTD results of emission (above) and population inversion (below) as a function of incident fluence [79].

Figure 1.13

which utilizes the time evolution of the quantum density matrix. This approach has been proposed by Trivedi et al. [72] for nanolasing plasmonic system.

Chapter 2

Samples Synthesis

In the previous chapter we have seen the possibility of creating laser emission from metallic nanostructures in a periodic lattice coupled to an active medium, in particular dye molecules. Now we proceed to evaluate the synthesis techniques that are used to realize plasmonic nanolaser devices.

The most used techniques to fabricate nanostructure arrays with high degree of control over shape, size and order of the nanostructures are *electron beam lithography* (EBL), *focused ion beam* (FIB) and *scanning probe microscopy* (SPM) *lithography* [85, 86]. However, these techniques have some drawbacks for a high throughput in a view of industrial fabrication: they require expensive instruments and long fabrication time, reducing the working area down to mm^2.

In the present work we adopted a cost-effective and high throughput technique, *nanosphere lithography* (NSL), first proposed and described by R. P. Van Duyne in 2001 [41]. NSL is based on the self-assembling of a monolayer of size-mono-dispersed polystyrene (PS) nanospheres (NSs) on a substrate. The wide diameter range of the PS NSs, from $40\,\text{nm}$ to few μm, gives large possibilities on various fabrications. The self-assembling
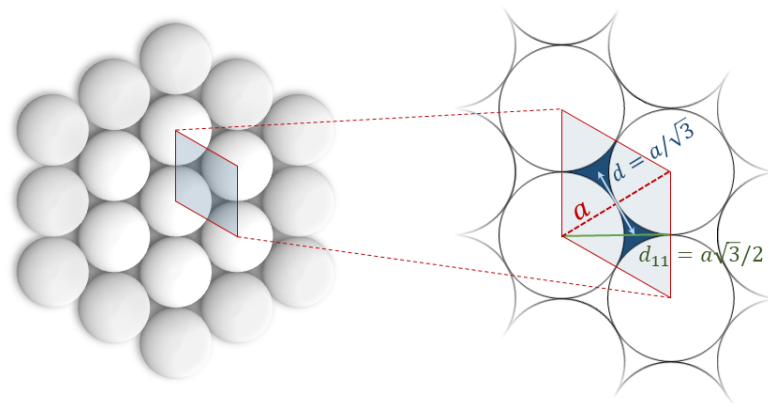
Figure 2.1: The lattice resulting from NSL: (left) two-dimensional hexagonal close-packed crystal, and the unit cell definition; (right) relevant parameters in the unit cell: (red dashed line) the lattice parameter $a = D$ (spheres' diameter), (sky blue line) the centre-centre distance $d = a/\sqrt{3}$ of interstices (identified by dark blue area) between nearby spheres and (green line) $d_{11} = a\sqrt{3}/2$ is a characteristic distance between two lattice line (in this case in the direction (1,1) (Miller indices)), that defines the diffraction properties of the lattice.

leads to the formation of a two-dimensional hexagonal close-packed crystal (shown in figure 2.1) over a substrate, covering large areas up to some cm^2 in which defectless domains can reach sizes of a hundred μm^2 [87].

As shown in figure 2.1, the NSs' dimension (diameter D) defines the lattice constant a of the hexagonal crystal. $d = a/\sqrt{3}$ represents the centre-centre distance i.e. to the distance between the interstices formed among the neighbouring spheres. The parameter $d_{11} = a\sqrt{3}/2$ is a characteristic distance between two lattice lines (in this case in the direction (1,1) (Miller indices)), which defines the diffraction properties of the lattice, as described in section 1.2.3.

The nanospheres self-assembled manolayer acts as lithographic mask to create different two-dimensional ordered nanostructure arrays. The combination of processes as *Reactive Ion Etching* (RIE) and *Physical Vapour Deposition* (PVD), in particular thermal evaporation and magnetron sputtering, allows us to synthesize different types of nanostructures. The most interesting structures for this project are *NanoDome*, *NanoDisk* and *NanoPrism* arrays; but other nanostructures can be created, such as *NanoHole* [88], *semi-NanoShell* [89], *split-NanoRing* [90] or *NanoRing* [91] arrays.

2.1 NanoSphere Lithography

Cleaning of Substrates

For a good assembling of the NSs crystal and to reduce, as far as possible, the formation of defects, a good cleaning of the substrates is needed to make them hydrophilic.

First an, *acid piranha* solution, which is composed of sulphuric acid (H_2SO_4) and hydrogen peroxide (H_2O_2) in proportion 3:1, is prepared. The strong oxidation process removes most of the organic impurities and simultaneously makes hydrophilic the substrate surface. The substrates immersed in this solution are left for one hour at $90\,^\circ$C.

After that, a *basic piranha* solution, which is composed of ammonium hydroxide (NH$_4$-OH) and hydrogen peroxide (H_2O_2) in proportion 3:1, is prepared. The substrates, after iterated rinses in Milli-Q water ($18.2\,$MΩ/cm resistivity at $25\,^\circ$C), are immersed for 20 minutes at $90\,^\circ$C in this basic solution. This guarantees a further level of cleaning and increases the surface hydrophilicity.

Finally the substrates are repeatedly washed and left in Milli-Q water before the use.

Cleaning of Polystyrene NanoSpheres

In this work, PS nanospheres with diameter $D = 522 \pm 12\,$nm and $340 \pm 10\,$nm are used. They are produced by Microparticles GmbH and preserved in a colloidal water solution at 5% in volume.

In general the chemical process of NS formation does not leave the particles really clean, surfactants are present to increase the stability of the spheres. However, during the self-assembling process, surfactants increase repulsive forces between the nanoparticles enhancing the probability of defect formation. For this reason, PS NSs are "*washed*" in alcohol, *2-Propanol* in this case.

Firstly, the colloidal solution is mixed 1:1 with 2-Propanol and centrifuged in order to separate the particles from the solution. Then the solution is substituted with the same quantity of Milli-Q water and 2-Propanol (1:1). With the help of a vortex and sonication, NSs are resuspended. This washing process is repeated three times and at the last filling,

the solution quantity is reduced to balance lost particles during the processes, restoring original number density of NSs.

Centrifugation is the critical step of washing: if it is too little the particles will be not enough aggregated and you will risk to loose a lot of particles; on the other hand if it is too much the resuspension will result difficult. In order to calculate the right time and centrifugation speed, Stokes' law has to be taken into account to extrapolate analytically the particles' speed v_{NS} (cm/s) during the centrifugation [92].

$$v_{NS} = \frac{1}{18} d^2 \frac{(\rho_s - \rho_0)}{\eta_0} 10^{-6} G$$

where d (μm) is the NS diameter and ρ_s (g/cm^2) their density, ρ_0 and η_0 (Poise) are density and viscosity of the solution, and $G = \text{RCF} \cdot g = 11.18 \cdot r \cdot (\text{RPM}/1000)^2 \cdot g$ is the acceleration due to the centrifugation, RCF is the Relative Centrifugal Force, g (cm/s^2)is the gravitational constant on the Earth, r (cm) is the radius of rotor and RPM is the revolution per minute.

Finally, the centrifugation time is $t = h/v_{NS}$ (s), where h (cm) is the cuvette height. For our system the optimized parameters are shown in table 2.1

Table 2.1: centrifugation parameters for the "washing" process of PS NSs.

NS Diameter (nm)	RPM ($\times 1000$)	time (min)
522	12	5
340	12	11

Self-Assembling

In order to form ordered monolayers of PS NSs, 20 μl of the previously prepared solution are taken and homogeneously deposited on a soda-lime glass (SLG) substrate, which is placed with a certain angle in a sample holder fixed on a motorized arm. This arm can drive the substrate into a crystallizer filled with high-purity Milli-Q water, as shown in figure 2.2, up to completely immersing it in water. In this procedure, PS NSs on the substrate surface detach from it and arrange themself on the water surface, forming a monolayer thanks to the presence of alcohol.

When the monolayer is formed, an iridescent colouration appears due to the diffractive behaviour of the monolayer and the sphere's size used in the range of visible wavelength. Moreover, if the monolayer is ordered iridescence appears stronger and homogeneous.

With another SLG or Si substrate, the mask is picked up manually or with the same motorized arm (figure 2.3), and left to dry. A hexagonal close-packed ordered structure is then formed by evaporation of the solvent on the surface's substrate.

When the solvent layer is lower than the spheres' size, the aggregation process starts to form an ordered monolayer (figure 2.4) due to lateral capillary forces. The attractive forces that lead the aggregation process are due to the spatial variation of the liquid surface slope that drives a superficial tension and the hydrostatic pressure. These forces compact the NSs into a hexagonal close-packed arrangement. Therefore, the growing of an ordered crystal is led by a primary ordered nucleus and the evaporation process tends to drive the other NSs by convective fluxes of surrounding liquid. When the particles are close to the nucleus, capillarity forces attract and attack the spheres to the nucleus in an
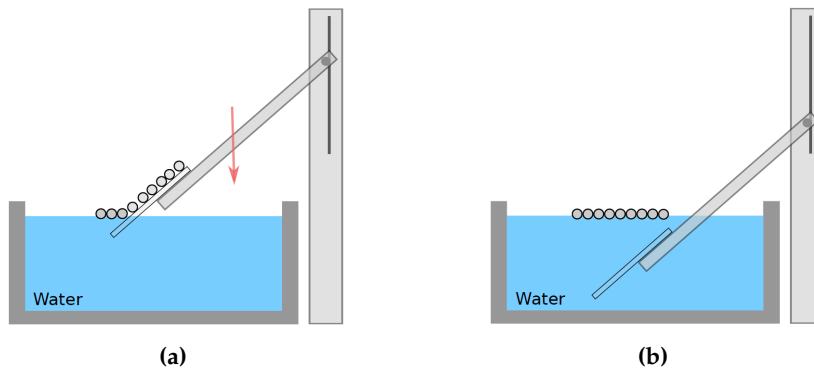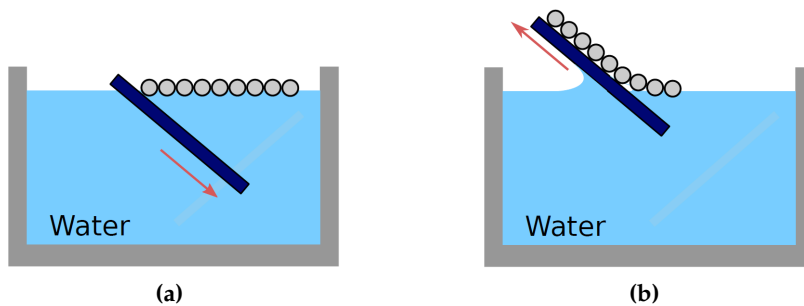
Figure 2.2: Schematic description of the device used for the mask self-assembling: the SLG substrate is fixed at the end of a motorized arm. PS nanospheres in colloidal solution are deposited on the glass. The glass is dipped in water **(a)** and the NSs float on the water surface **(b)** forming an ordered monolayer.

ordered position, driving an ordered growing of the crystal. The mask is then formed when the evaporation is completed [93].

In order to help this natural phenomenon all the process is made in a controlled atmosphere, where the humidity and temperature are optimized to reduce the defect formation controlling the evaporation time of the solvent. The chamber is kept at room temperature (around $25\,°C$) with a humidity in the range of $70\% -80\%$.

In figure 2.5 **(a)** we can see some examples of the synthesized masks with 340 (left) and $522 \pm 12\,nm$ (right) diameter polystyrene nanospheres. The high degree order of the two-dimensional lattice of PS nanospheres gives the distinctive iridescent color of the masks shown in the figure.

Different characterization technique have been used to investigate the mask's quality. An example of SEM and AFM measurements is reported in figure 2.5 **(b)** and **(c)**. However, this type of morphological characterization can explore a relatively small area (μm^2) compared to the size of the sample (cm^2), even if they give directly an estimation of defects such as vacations, dislocations, grain boundaries or poly-domains. Optical techniques are so preferred because allow to estimate quicker the quality of the mask on a large area. The optical techniques used in this work are optical diffraction and UV-VIS-NIR spectroscopy, which will be described below.

Figure 2.3: Procedure to pick up the PS monolayer formed on the water surface. First the substrate is dipped in water **(a)**, then it is carefully extracted bringing the mask with it **(b)**.
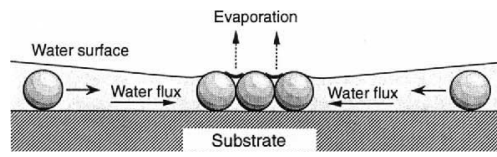
Figure 2.4: Schematic description of the nanospheres aggregation process.

Optical Diffraction

Optical diffraction technique is one of the most powerful technique in order to evaluate the order of a two-dimensional lattice. Since PS NSs' diameter is in the visible range, we can study the order of the lithographic mask by optical diffraction by using visible laser. The monolayer of nanospheres acts as a diffraction grating, where every single sphere diffuses the light according to Mie's description [51].

Figure 2.6a shows the scheme of the optical diffraction set-up. The beam of a cw diode laser source, at $\lambda = 405$ nm impinges at normal incidence on the sample and so on the lattice plane, and from the interaction with the grating maxima of diffraction arise with an angle which can be estimated by the Bragg condition that for a two-dimensional hexagonal grating becomes

$$\frac{\sqrt{3}}{2} a \sin \theta = \frac{\lambda_0}{n_{eff}} \qquad \Rightarrow \qquad \theta \simeq 41° \tag{2.1}$$

where $\lambda_0 = 405$ nm is the wavelength of the incident beam in free space, $\frac{\sqrt{3}}{2}a$ is the grating period and n_{eff} is the effective refractive index in the nanosphere layer that can

(a)

(b)

(c)
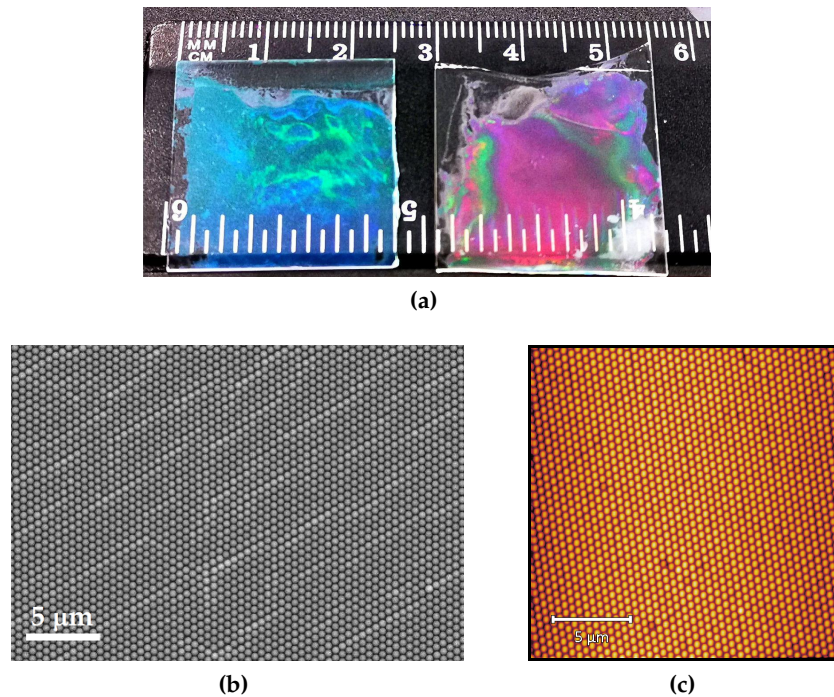
Figure 2.5: (a) Masks made of 340 (left) and 518 nm (right) diameter polystyrene nanospheres. **(b)** and **(c)** show SEM and AFM images of a 522 PS mask, respectively.

be calculated as

$$n_{eff} = n_{PS}\Phi_{PS} + n_{air}\Phi_{air} \simeq 1.36 \tag{2.2}$$

where $n_{air} \simeq 1$, $n_{PS} \simeq 1.59$ is the polystyrene refractive index and $\Phi_{PS} = 0.605$ and $\Phi_{air} = 0.395$ are the volume fractions occupied by PS nanospheres and air, respectively.

The outgoing beam from the mask is blocked by a sheet of paper placed close to the sample. The image formed on it is then projected by a lens on a CCD camera and recorded.

An example of diffraction pattern of a 2D hexagonal lattice of $522\,nm$ PS NSs is showed in figure 2.6b: the centre spot is obscured in order to enhance the contrast of the maxima. The image gives the possibility to investigate the order of the mask on the illuminated region. This is possible by evaluating the spots' intensity profile and their shape.

We know that a hypothetical infinite perfect lattice gives a diffraction pattern with narrow spots. The shape and intensity of the spots is modified by the presence of point or line defects. Moreover, domains with different orientation produce diffraction patterns with different orientation. Therefore, the presence of polydomains leads to see multiple points on the diffraction pattern, or the formation of textures around the main spots. Furthermore, if polydomains are completely randomly distributed Debay-Sherrer rings appear denoting a high degree of disorder of the lattice.

Figure 2.6b shows therefore an excellent arrangement of the PS NSs in a hexagonal lattice. In addition, we can identify the high symmetry axes of the lattice. In figure 2.6c, the first neighbours points of the reciprocal lattice, labelled with Miller notation, the first
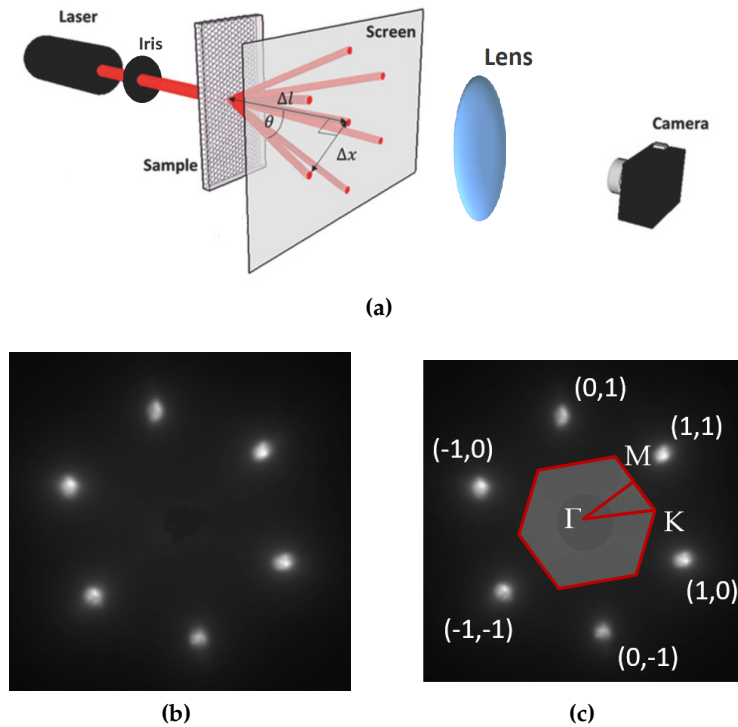
Figure 2.6: (a) Set-up for optical diffraction measurement [94]. **(b)** Diffraction pattern of a two-dimensional hexagonal lattice of $522\,nm$ PS nanospheres and in **(c)** superimposition of the first Brillouin zone and identification of reciprocal vectors.

Brillouin zone and so ΓK or ΓM direction of the reciprocal lattice are highlighted.

This method give us two important information: the quality of the arrangement and the direction of the lattice orientations in the laboratory reference system.

Furthermore diffraction is the cause of the mask iridescence, for this reason we can say qualitatively that a homogeneous iridescence corresponds to a high degree of lattice order in the long range.

UV-VIS-NIR spectroscopy

We can also evaluate the mask quality by absorbance spectra, evaluating the shape of the peak that apperas in the spectrum due to the interaction of the incident radiation with the mask, which can be considered as a photonic crystal with a specific band structure that determines this interaction [95].

For these measurements, a Jasco V-670 and an Ocean Optics (HR4000) spectrometer have been used. The principal difference of these instruments are the working spectral range and the operation mode: Jasco V-670 works from 190 to 2600 nm while the Ocean Optics spectrometer works from 190 to 1100 nm. Furthermore, while Jasco V-670 selects the working wavelength by two gratings and then drives the beam on the sample, the Ocean Optics spectrometer separates the spectral components of the light beam after the light has interacted with the sample, collecting them simultaneously from an array of detectors and so permitting to analyse at the same time each wavelength. In the Ocean Optics system used, the light beam is driven by optical fiber from the DH-2000 BAL source to the sample and from the sample to the HR4000 detector.

Finally we can say that Jasco V-670 has more sensitivity but Ocean Optics spectrometer is more versatile and faster. Since the spectral behaviour is the main characterization for our devices and their components, we have widely used this instrumentation, interchanging these spectrometers according to the measurement conditions.

In the specific case of PS NSs masks both of these instrumentations can be used. In Figure 2.7 it is shown, as an example, the absorbance spectra of 340 nm PS NSs mask (in **(a)**) and 522 nm PS NSs mask (in **(b)**) recorded with the Jasco V-670 spectrometer. For the used PS nanospheres with diameter of 340 nm, an absorbance peak arises at the wave-

(a)

(b)
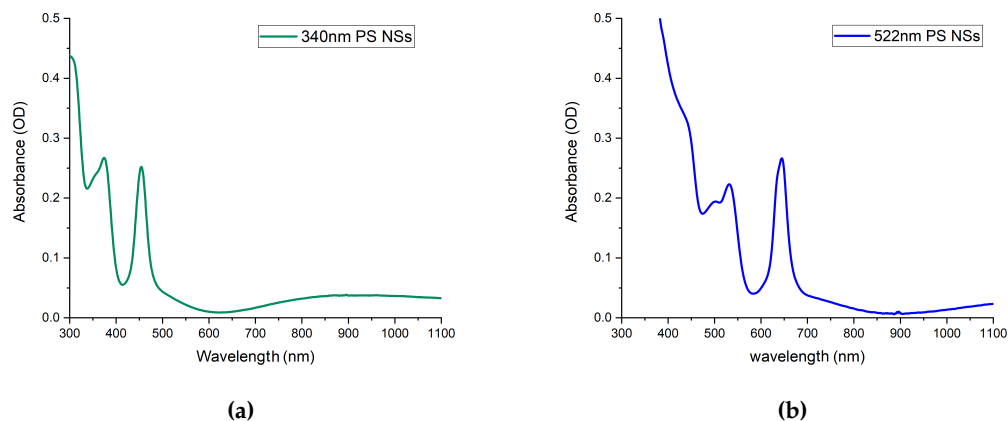
Figure 2.7: Absorbance spectrum of a PS masks: in **(a)** PS NSs with 340 nm diameter, in **(b)** PS NSs with 522 nm diameter made by Jasco V-670.

length of 455 nm, instead for 522 nm NSs the absorbance peak appears at 640 nm.

From this spectrum, it is possible to extract information about the quality of the synthesized mask. The spectral position of the peak can be associated to the PS nanospheres' size, whereas the intensity and bandwidth of the absorbance peak can be associated to the quality of the photonic crystal: the higher and narrower is the peak, the fewer defects are present in the photonic crystal, then the better the mask is [95]. In this case the absorbance spectra reported in figure 2.7 present absorbance peaks narrow enough and can be approximated by a Gaussian curve, which confirm the high order in the illuminated area of the lithographic masks obtained by NSL.

2.2   Reactive Ion Etching

A useful technique that helps us to modify materials at the nanoscale is *Reactive Ion Etching* (RIE) [96]. RIE consists in a dry ion-assisted chemical etching process which uses a chemical reactive plasma to erode several materials. Depending on the material to be etched, we have to choose the right type of gas to adopt.

This selective etching is used to reduce the PS NSs' dimension leaving unchanged the lattice structure and to erode sacrificial layers in the nanodisk formation process that will be discussed later. The PS NSs are etched by a gas mixture of oxygen (O_2) and argon (Ar). Argon, being a noble gas, is inert and etches the sample physically, i.e. the Ar ions hit the sample and the transfer of kinetic energy gives rise to the sputtering of the material. Instead, oxygen etches chemically the sample given its reactive nature.

An electrically isolated plate, which is thermalized by a water system, hosts the samples inside a vacuum chamber. The pressure is then decreased down to 10^{-3} mbar before inserting the gasses, and after this the plasma is generated by a radio-frequency (RF) electric field (13.56 MHz). Since the plate is negatively charged, the ions, forming the plasma, are accelerated toward the sample. This process results anisotropic, due to the vertical collisions of the ions on the NSs, which are etched principally in this direction.

The etching process depends on several factors, such as gas ratio, RF power and chamber pressure, which are directly linked with the gas flux and were previously cali-

(a) PS 340 nm

(b) PS 522 nm
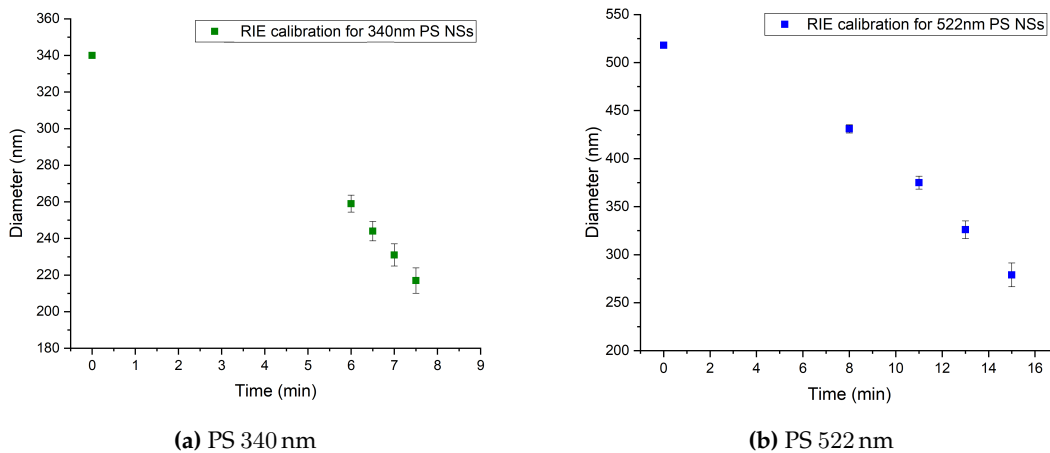
Figure 2.8: Calibration curve of PS NSs' diameter as a function of RIE time, **(a)** for NSs with 340 nm diameter while **(b)** for NSs with 522 nm diameter.

(a) Top view
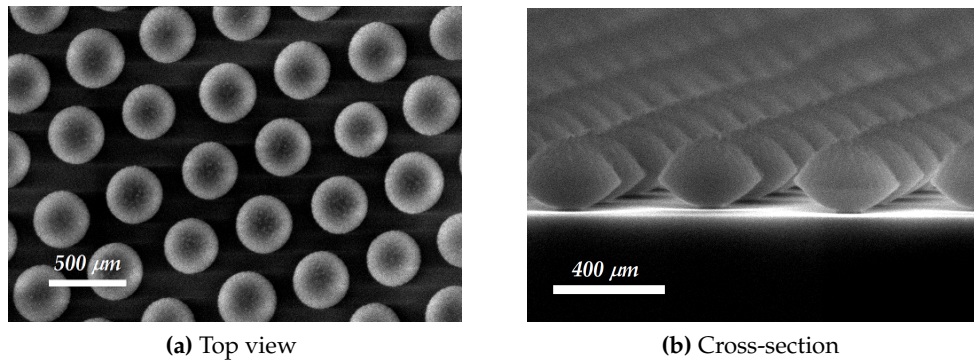
(b) Cross-section

Figure 2.9: SEM images of a $522\,$nm PS nanosphere array after 13 min RIE:**(a)** Top view and **(b)** cross-section. The final height of the nanospheres is of about $250\,$nm and the diameter of $335\,$nm.

brated. In table 2.2 the optimized parameters for the etching process are reported. The etching time is the free variable used to get the desired spheres' size: this dependence is shown in figure 2.8, in **(a)** for spheres with an initial diameter of $340\,$nm and in **(b)** of $522\,$nm.

Table 2.2: RIE parameters to reduce the PS NSs' size.

Pressure	O_2 flux	Ar flux	V bias	Power
$105 \cdot 10^{-3}$ mbar	9.2 sccm	3.6 sccm	55 V	15 W

A notably characteristic of the RIE process is the possibility etch PS NSs maintaining their initial positions, as can be seen in figure 2.9a. Furthermore, by changing the pressure the process works in different regimes: at low-pressure (fig. 2.10a) the mean free path of the ions is longer and they can reach the samples driven by the electric field, making the erosion more anisotropic and quicker due to the higher kinetic energy that the ions can reach; on the other hand, a high pressure (fig. 2.10b) leads to a more isotropic and slower etching, due to the lower mean free path of the ions. Therefore, in a image in cross-section as shown in figure 2.9b it can be recognized an high pressure regime for the setted values.

The roughness of the spheres is another detail that can be adjusted by means of the ratio between the different gases, changing the balance between physical and chemical etching: in figure 2.9b it is notable the low roughness on the surface.

Furthermore, in this etching condition the spheres can be eroded until the time comes when they collapse, by destructing the order; this thus imposes a maximum limit of the

(a) Low pressure

(b) High pressure
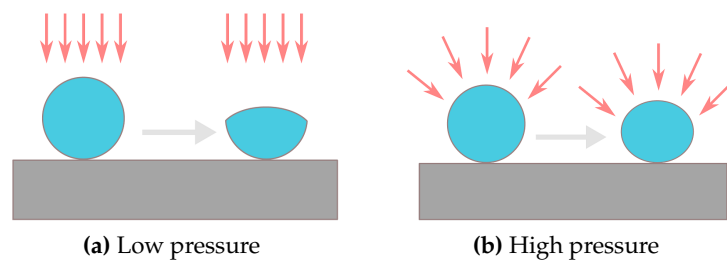
Figure 2.10: The two types of RIE etching.

final spheres' diameter which experimentally is placed at about half of the initial value.

2.3 Deposition Techniques

In order to obtain plasmonic nanostructures, metal has to be deposited. Two physical vapour deposition (PVD) methods were employed in the present: *magnetron sputtering* and *thermal evaporation*. Both of them allow us to deposit mono-elemental thin layers, e.g., Au, Ag, Ti and Cr, by finely controlling the thickness from a few nanometers up to hundreds of nanometers, whereas layers of multi-elemental materials, such as silica (SiO_2) or alloys, can be obtained only by magnetron sputtering.

Magnetron Sputtering

Magnetron sputtering, showen schematically in figure 2.11a and an image of the used one fig. 2.11b, is a deposition method in which the atoms or molecules that we want deposit on a substrate are ejected of a target that is bombarded by high-energy particles [97]. The bombardment is made by ions of a plasma gas which are accelerated by an electric field. In order to avoid reaction from the gases and the target or the growing film, noble gases (typically argon, krypton, xenon or radon) are used, oxygen to make a reactive environment is used instead.

The *sputtering yield* is defined as the number of target atoms ejected per incident ion. It describes the efficiency of ejecting atoms from ion collisions and depends on binding energy and mass of the target and the kinetic energy and mass of the incident ions. The deposition efficiency depends also on the chamber pressure, because the presence of the gas or atoms in general generates collisions during the diffusion toward the substrate of the sputtered target atoms, which decrease the number of atoms that reach the samples, as well as the degree collimation. On the other hand, low pressure in the chamber decreases the sputtering efficiency because the number of ions is low. A balance of the pressure is then needed, and in our system an optimized pressure of about $3.5 \cdot 10^{-3}$ mbar is set.
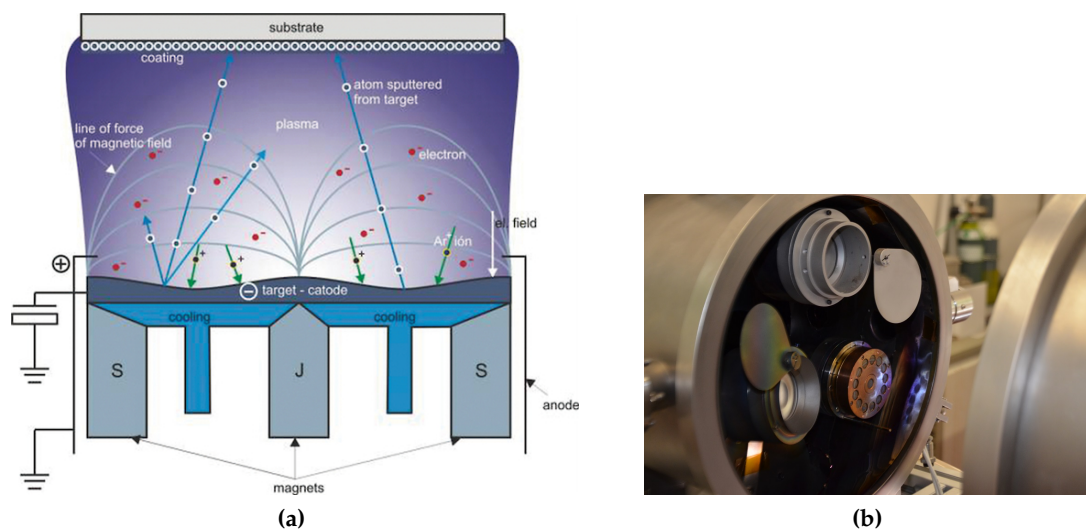
Figure 2.11: (a) Schematic representation of magnetron sputtering process. **(b)** Magnetron sputtering photo.

The target is a disk of the material to sputter and acts as the cathode of an electrical circuit having high negative voltage applied to it, while samples is placed at the anode. Before introducing the gases the chamber is brought to a pressure of about 10^{-6} mbar, in order to limit the presence of impurities, and then Ar is introduced at the optimized pressure. The plasma is created by an electric field that accelerates electrons which by collisions generate Ar^+ ions and more electrons. The ions are accelerated to the cathode, hit the target by causing the sputtering of the target atoms, which diffuse and deposit on the substrate.

In order to increase the sputtering yield and deposition rate, the *magnetron effect* is used. A series of magnets mounted below the target generate a magnetic field superimposed to the electrical one, with the field lines parallel to the target surface. This magnetic field confines the electrons in a region near the target, avoiding their loss outside the plasma and increasing collision frequency. This determines an enhancement of the ionization degree, i.e. an higher plasma density, which enhances the sputtering yield and the deposition rate.

If the target is a conductive material, a DC sputtering system can work. However, if the target is an insulator, the sputtering glow discharge cannot be sustained because of the rapidly accumulation of a positive charge of ions on the front side of the target. In order to sustain the glow discharge with an insulator target and to avoid the accumulation of the ions, the DC power supply is replaced by a Radio-Frequency (RF) power supply (at 13.56 MHz).

The sputtering system used in this work consist in a vacuum chamber where a rotary and a turbomolecular pump create and maintain the high vacuum in a dynamic condition with the Ar gas, whose flux is regulated by a fluximeter. Inside the chamber there are three torches that host the targets, two are RF sources and one is a DC. In front of the torches is placed the sample holder in a confocal configuration.
The sample holder distance between the targets and the sample holder can be varied from ~ 5 cm to ~ 20 cm and it is possible to use two configurations: one with the sample static in front of the target and the other, tilting the torches, in which the sample is placed in the middle of the three torches and with the possibility to set in rotation for a more uniform deposition. In general, samples are not placed too close from the target in order to avoid an excessive thermal radiation that can damage the PS nanospheres.

Thermal Evaporation

Thermal evaporation is based on in heating of material above its evaporation temperature. The evaporated atoms have to reach the sample placed above the target at a certain distance, without interact with other atoms. In order to satisfy this condition the process takes place in a vacuum chamber where the pressure has to be such that the mean free path of the atoms is greater than the distance between target and sample. In our case the distance is around 25 cm and the pressure is kept below $3 \cdot 10^{-5}$ mbar during the process. A scheme of the thermal evaporation chamber is shown in figure 2.12a. The metal to evaporate is placed on a tantalum (Ta) crucible, which is heated by Joule effect with a high current, up to the temperature necessary to obtain metal evaporation.

By controlling the current, the temperature can be tuned controlling in this way deposition rate. The deposition rate is monitored by a *quartz crystal microbalance* placed at the same height and close to the samples. The microbalance measures the thickness of the deposited material by the electrical resonance frequency variation of a quartz oscillator.
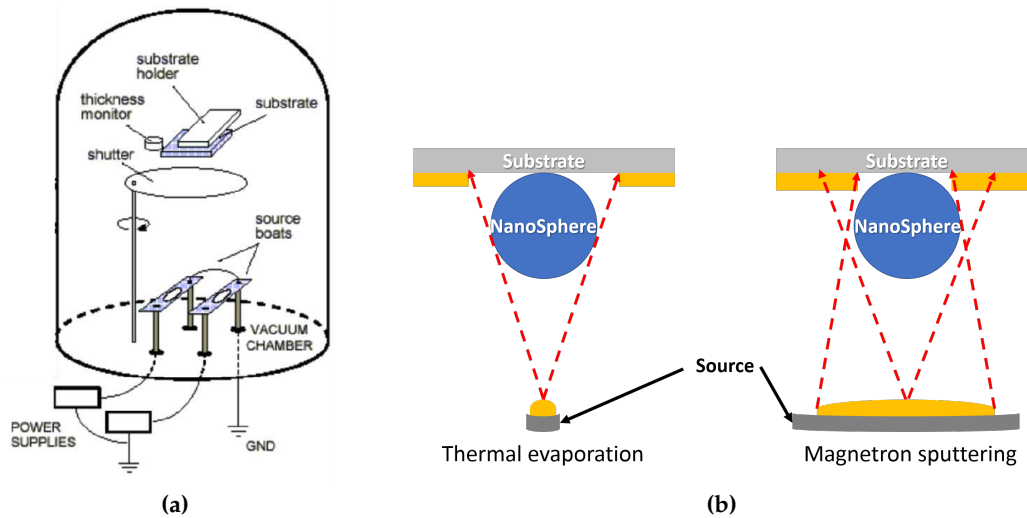
Figure 2.12: (a) Scheme of thermal evaporation chamber with two crucibles where pellets of two different elements could be placed. **(b)** The difference between the precursor sources for thermal evaporation and magnetron sputtering set-ups is depicted. The distances and the dimensions are not to scale.

Then the thickness of the deposited metal can be monitored in real-time and thus finely controlled. In our case, we mainly used the evaporator to deposit silver, which is places on the crucible and it is heated up to the evaporation. In particular, the current is kept in a range between $70\,A$ and $90\,A$ which corresponds to a deposition rate that ranges between 1 and $2\,nm/s$. The deposition time is therefore the variable that allows the control over the deposited thickness. For this purpose, a shutter above the crucible can be used to stop the deposition at the desired time.

Figure 2.12b highlights this difference between thermal evaporation and magnetron sputtering. Small differences occur when metal is deposited by thermal evaporation or magnetron sputtering due to the different geometry of the two deposition set-ups. The thermal evaporation crucible can be considered as a divergent point source since its dimensions (circular well with $\sim 1\,cm$ diameter) are much smaller than the distance between the crucible itself and the sample holder ($\sim 25\,cm$). Therefore, the divergence of the source produces a shadow effect, and the footprint left by an obstacle results larger than the obstacle itself. On the contrary, the source in the sputtering process is a plasma ring with $\sim 5\,cm$ diameter and samples are placed only $\sim 10\,cm$ far from the target. This ensures the uniformity of the sputtering deposition and produces an opposite effect with respect to the evaporation. Therefore, depositing through an obstacle yields a footprint smaller than the obstacle itself.

2.4 NanoDome Array

The first plasmonic nanostructure taken in to account is a continuous metallic film nanostructured by nanodomes placed in a hexagonal array. As shown in figure 2.13a, starting with NSL and obtained the mask over a SLG substrate, the PS NSs are subjected to a RIE process. The spheres are reduced, maintaining the lattice order, up to $\sim 330\,nm$. After that, (fig. 2.13b) by sputtering, a layer of SiO_2 is deposited in order to create a con-
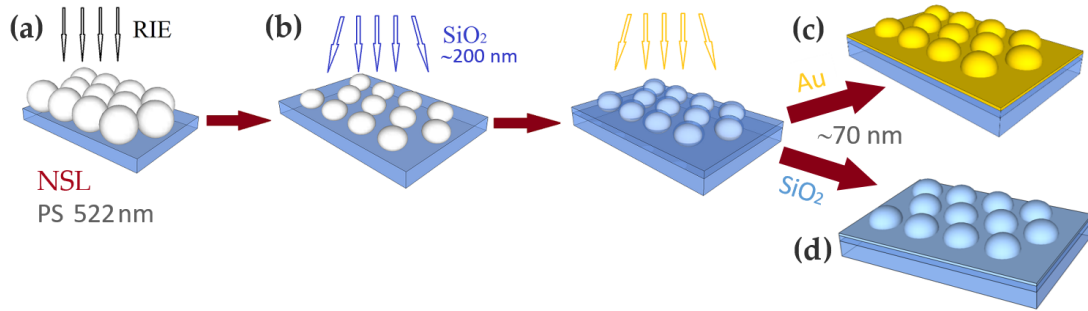
Figure 2.13: Schematic representation of the fabrication steps for the synthesis of the nanodome array. First, a close-packed array of PS nanospheres is formed by self-assembling, then a RIE process **(a)** is used to reduce the spheres' size. **(b)** A silica layer is deposited on the PS NSs by magnetron sputtering. A gold **(c)** or silica **(d)** layer is then deposited by a magnetron sputtering.

tinuous layer, making also the structure mechanically, chemically and physically more stable. A thin film of gold (about 70 nm thick) is then deposited by magnetron sputtering (fig. 2.13c). Another set of samples is also fabricated, depositing a further layer of SiO_2 with the same thickness of the metallic layer, **(d)**. This can allow to study optical properties which comes only from the geometric arrangement of the nanostructures without the plasmonic contribution of the metal.

The geometric parameters of the nanodome array are fixed by the lattice constant a defined by the initial spheres' diameter. However, it is possible to tune the plasmonic properties of nanodome array by changing the dimension of the nanodomes, by different RIE time or SiO_2 layer thickness, and the metal thickness. For this type of samples the PS NSs are reduced up to a diameter of about ~ 330 nm, covered by ~ 200 nm of SiO_2 and ~ 70 nm of gold, resulting with a final nanodomes' diameter of about ~ 490 nm.

Figure 2.13 shows SEM images of typical nanodome array synthesized in this work: **(a)** a top view of Au nanodome array of about $16 \times 13\,\mu$m in order to understand the order of lattice, **(b)** is a zoom in order to investigate morphological characteristic of a nanodome, where is superimposed the primitive cell of the lattice with the lattice con-
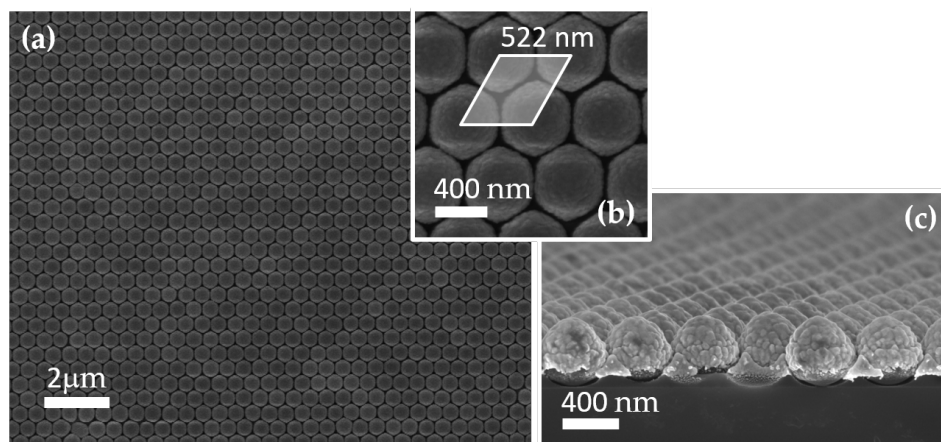
Figure 2.14: (a) SEM image in top view of a typical Au nanodome array synthesized, using PS nanospheres of 522 nm diameter. **(b)** Close-up view of the nanoarry with the primitive cell superimposed. **(c)** SEM image in cross-section.

stant; and in *(c)* a cross image.

2.5 NanoDisk Array

Another fabricated structure is the nanodisk array.

The scheme of synthesis is reported in figure 2.15. **(a)** A PMMA sacrificial layer is placed before the formation PS mask. However, since the lithographic mask has to undergo a RIE process, the sacrificial layer has to be covered by SiO_2 to preserve it from this step. The sacrificial layer is made by PMMA (Polymethyl methacrylate) deposited by spin coating: a PMMA powder is diluted in toluene in 5% w/w concentration; two spin steps are performed, one with 3500 RPM for 60 s and the second with 5000 RPM for 10 s; finally the sample are placed on a hot-plate at 170 °C for 10 minutes to let the solvent evaporate. 180 nm of PMMA are prepared and covered by 25 nm of SiO_2 made by magnetron sputtering, completing thus the sacrificial layer.

(b) A monolayer of PS NSs is formed over the silica layer and then subjected to RIE **(c)**. After that 20 nm of Cr is deposited by magnetron sputtering **(d)** and the PS NSs are removed by an adhesive tape **(e)**. In this way Cr nanohole array is formed as negative mask for the nanodisks. At this point two RIE processes are needed, **(f)**: one to etch the silica layer by CF_4 gas and the other with Ar and O_2 to erode PMMA layer. The RIE parameters are reported in table 2.3.

Silver deposition is performed by thermal evaporation **(g)** owing to the better collimation of the deposition. **(h)** Finally, the nanodisk array is obtained by removing the sacrificial layer by sonication in toluene. An example of Ag nanodisk array is shown in figure 2.16 with different magnifications.

As for nanodome array, the lattice constant a of nanodisk array is defined by the initial PS NSs' diameter. In any case, the plasmonic properties of the nanoarray can be tuned by varying diameter and height of the disks. It is worth noting that using sputtering to deposit Cr nanohole array as a mask helps to reduce the minimum diameter reachable
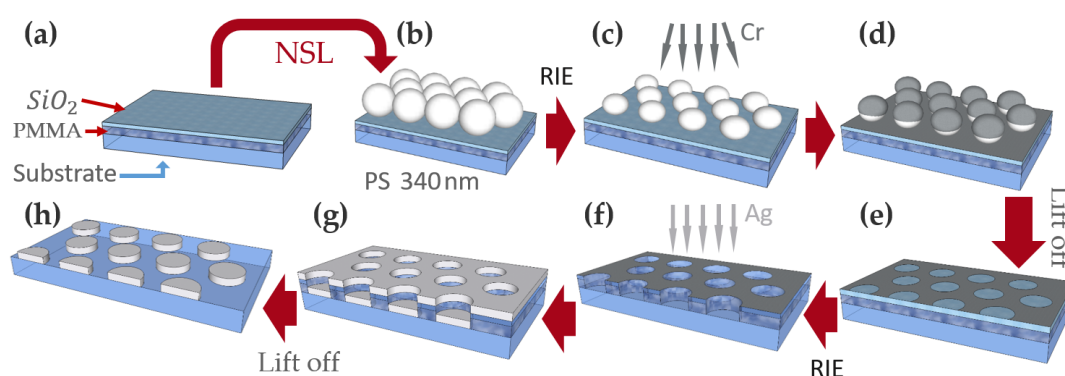
Figure 2.15: Schematic representation of the fabrication steps for the synthesis of the nanodisk array. **(a)** Sacrificial layers (PMMA and SiO_2) are deposited. **(b)** A two-dimensional close-packed hexagonal lattice of 340 nm PS NSs is formed. **(c)** A RIE process is made to reduce NSs' diameter. **(d)** A Cr layer is deposited by magnetron sputtering to form a nanohole array negative mask after **(e)** the removal PS NSs. **(f)** RIE processes to etch silica and PMMA up to the substrate. **(g)** Ag is deposited by thermal evaporation. **(h)** The nanodisk array is formed after the removal of the sacrificial layers by sonication in toluene.
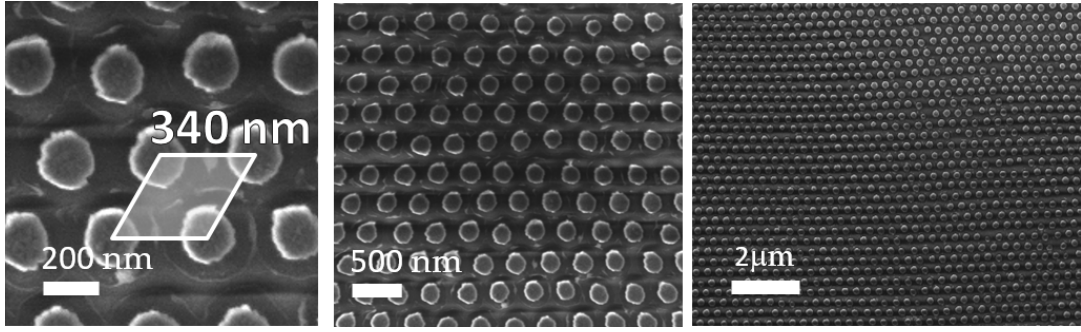
Figure 2.16: SEM images with different magnifications of an Ag nanodisk array synthesized by NSL with $340\,nm$ PS NSs.

Table 2.3: RIE parameters to etch silica and PMMA layers.

Step 1			
Pressure	CF$_4$ flux	V bias	Power
70×10^{-3} mbar	15 sccm	150 V	50 W

Step 2				
Pressure	O$_2$ flux	Ar flux	V bias	Power
105×10^{-3} mbar	9.2 sccm	3.6 sccm	55 V	10 W

with the RIE process of the NSs, limited by the collapse of the etched PS NSs that destroys the order of them. The height of the nanodisks is controlled by the last metal deposition and the only constrain is that it has to be much smaller than the thickness of the PMMA layer in order to allow the lift off.

2.6 NanoSphere Array

The last structure fabricated is the nanosphere array, which consists in a honeycomb array of nanospheres. The synthesis starts creating the lithographic mask of PS NSs with a diameter of $522\,nm$ over the substrate. Metal is deposited by thermal evaporation over the mask. The metal atoms reach the substrate only through the interstices between the spheres and thus, removing the mask by peeling off an with adhesive tape, triangular nanoprisms are produced, as shown in figure 2.17.

It can be shown that interparticle distance d between triangles is linked to the nanospheres diameter a by

$$d = \frac{1}{\sqrt{3}}a \tag{2.3}$$

Moreover, the perpendicular bisector of the nanotriangle (b) and the width L are correlated to the diameter a of the nanosphere by the expression:

$$b = \frac{3}{2}\left(\sqrt{3} - 1 - \frac{1}{\sqrt{3}}\right)a \approx 0.233\,a \qquad L = (2 - \sqrt{3})\,a \tag{2.4}$$

The height of the prisms is set by the evaporation parameters, in this case $200\,nm$ of Ag is deposited. However, there is a maximum height that can be reached for each
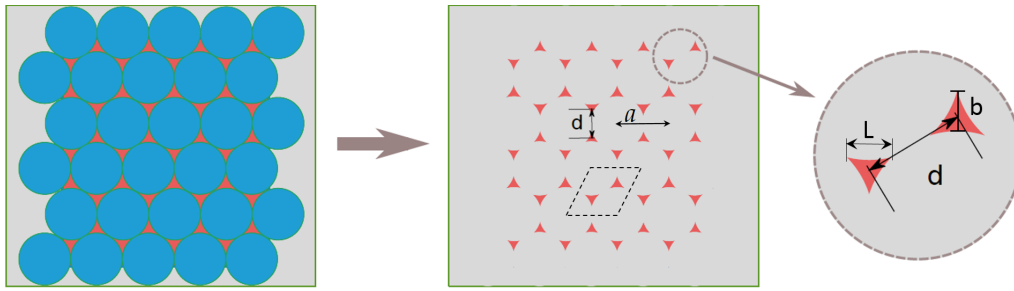
Figure 2.17: Nano prism array from NSL method. First metal is deposited (left) then mask is removed (right). The dashed parallelogram represents the unit cell of the ordered array of nanoprisms. The main geometrical parameters are showed: a is the periodicity, d the distance between the two nanoprisms in the unit cell and b the height of the triangular shape and L the width.

nanoparticle due to the shrinking of the interstitial area among the nanospheres during the evaporation process. As the metal is deposited through the nanospheres mask, material accumulates at the edge of the triangular shaped interstitial area. When aperture closes the maximum height of the nanoprism is reached.

In order to create nanoshere arrays, thermal annealing has been used to reshape the particles from triangular nanoprisms to nanospheres.

Since LSPR strongly depends on the nanostructures shape [98], the plasmonic properties change when the shape change by the thermal annealing process. This process is made by a tubular oven (Carbolite CTF 12/75/700) in air.

In figure 2.18 the effect of three thermal treatments at different temperature (100, 110, 120 °C) on the nanoprism shape is shown. Figure 2.18e reports the absorbance spectra of the nanoarrays at each annealing step. It can be noted how by increasing the annealing temperature, LSPR blue-shifts. This is due to the change of the nanoprism shape toward the spherical shape: in fact every change of shape from the ideal situation of the sphere red-shifts the LSPR peak [98], as said in the section 1.2. The trend of the LSPR peak wavelength as a function of the annealing temperature is shown in figure 2.18f and the data are reported in table 2.4.

Table 2.4: annealing temperature and LSPR peak wavelength of Ag nanoprism arrays made by PS NSs with 522 nm diameter.

Annealing Temperature (°C)	λ_{LSPR} (nm)
-	665
100	564
110	538
120	517

2.7 Gain Medium

In the present work organic laser dyes are used as gain media and they are chosen for their very high quantum yield. They are made by *Lambda Physik* and conserved in form of little solid crystals. These dyes have an easy processability thanks to their solubility in

(a) As deposited

(b) 100 °C

(c) 110 °C

(d) 120 °C

(e) Absorbance spectra

(f) Plot of λ_{LSPR} vs Annealing Temperature
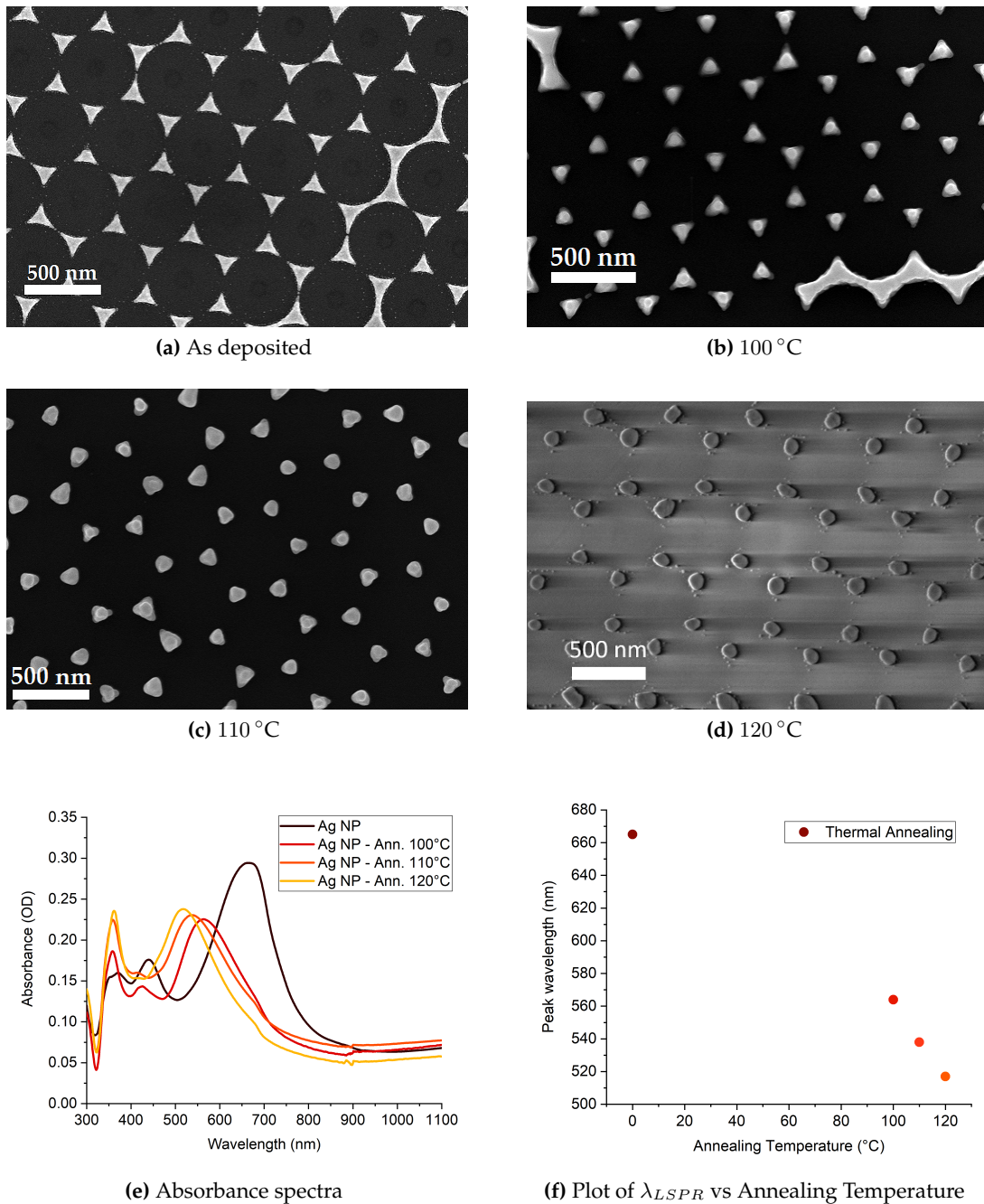
Figure 2.18: SEM images of Ag nanoprism array with 522 nm constant lattice: **(a)** as-deposited and annealed **(b)** at 100 °C, **(c)** at 110 °C and **(d)** at 120 °C. In **(e)** the corresponding absorbance spectra are shown. **(f)** LSPR peak wavelength as a function of the annealing temperature.

(a) Pyridine 2   **(b)** Styryl 9M
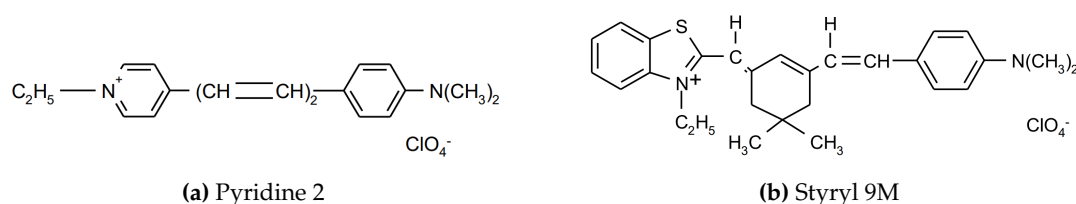
Figure 2.19: Molecular structure of **(a)** Pyridine 2 and **(b)** Styryl 9M

most of common solvents, such as ethanol, methanol, acetone or DMSO. This helps also an easy integration in a polymer matrix for a solid state device.

The dyes were selected based on their emission spectral region in which the plasmonic structures also work. In fact, in order to switch on the coupling between the gain medium and our nanostructure arrays, the emission spectrum of the dye molecules has to be spatially and spectrally matched with the plasmonic resonance of the metal nanostructure arrays. Therefore, after the characterization of the optical properties of our plasmonic nanoarrays, showed in the next chapter 3, we are able to evaluate the spectral working region of the metal nanostructures. Then, a suitable dye can be chosen in order to coupled the spectral region of its emission with the plasmon resonance, as section 4.2 shown. So, after these considerations, we are able to choose proper laser dyes, which, for this work, result to be*Pyridine 2* and *Styryl 9M*. Their molecular structures are drawn in figure 2.19 and their features are listed in table 2.5. From the molecular structures, we can note how these systems are complex respect to a single atom, making a detailed analysis of their properties difficult. The absorption and emission spectra of the used dyes are shown in figure 2.20. The dye molecules are diluted in ethanol with a concentration of about $1\,\text{mM}$ and the solution is illuminated by the second harmonic ($\lambda = 532\,\text{nm}$) of Q-switched ns pulsed Nd:YAG laser. Pyridine 2 (figure 2.20a) presents an absorption peak at $505\,\text{nm}$, while an emission peak in ethanol at $694\,\text{nm}$. Styryl 9M (figure 2.20b) has an absorption peak at $583\,\text{nm}$, while an emission peak in ethanol at $808\,\text{nm}$. Both work in the visible range and show a wide *Stokes shift*, which is the difference between the positions of maximum absorption and maximum emission. This shift results from two actions: vibrational relaxation or dissipation and solvent reorganisation [99]. Due to this large Stokes shift, the self-absorption of its own emission radiation is very low, increasing thus the quantum yield (eq. 1.5).

Table 2.5: main properties of the used laser dyes.

	Pyridine 2	**Styryl 9M**
Chemical Formula	$C_{19}H_{23}N_2.ClO_4$	$C_{28}H_{33}N_2S.ClO_4$
Molecular Weight (g/mol)	378.85	529.09
Maximum absorption wavelength (nm)	505	583
Maximum emission wavelength in EtOH (nm)	694	806

Even if the molecular structures are complex, it is possible to describe molecules by the so-called *free electron model* [100]. The model considers the molecule as a potential well with its electrons inside, where the length of the molecule L is equal to the width of the well. This well can be approximated by a rectangular well and the energy levels are

well known

$$E_n = \frac{h^2 n^2}{8 m_e L^2} \tag{2.5}$$

where n is an integer, m_e is the electron mass and L is the width of the well. It should be noted that stable dye molecules have even number $2N$ of electrons due to the π orbitals of the carbon bonds. The lowest energy state of the molecule corresponds to the situation in which electrons occupy the lowest N electronic energy levels; each level is occupied by two electrons with opposite spins. This molecular state has, however, total zero spin, i.e. it is a singlet state, denoted by S_0 in fig. 2.21 [101]. An approximate value of the energy of the most external electrons of this state, E_N, can be obtained from eq. 2.5 with $n = N$.

The state S_0 corresponds to the situation in which two electrons are paired in the E_N energetic state with opposite spin. The first excited state of the singlet, indicated with S_1, corresponds to the situation in which an electron is promoted to the E_{N+1} level without a spin flip. The energy difference will be $E_{N+1} - E_N$, according to eq. 2.5, and this value decreases increasing the length L of the molecule. If the spin of the electron that is promoted to the first excited level is flipped, the molecule will have a total spin of one and will be in a triplet state, indicated by T_1. Excited states of singlet S_2 and triplet T_2 are produced if the electron is promoted to the next energy levels and so on. It should be noted that in figure 2.21 the sets of close lines in each energy level represent the vibrational energy levels of the molecule. In this figure the scheme of the electronic and vibrational energy states of the molecule is reported as a function of the configuration coordinate, which describes one of the many vibrational modes that a long-chain dye molecule has. Due to the presence of a very high number of both vibrational and rotational modes of the molecule, and also of line enlargement mechanisms, the rotational-vibrational structure is in fact not solvable at room temperature.

Let's consider what happens when the molecule interacts with an em wave. It must be remembered that the selection rules involving the absorption and/or photon emission require that $\Delta S = 0$ in the transition: therefore only singlet-singlet and triplet-triplet transitions are allowed, while those of singlet-triplet are prohibited. So the interaction with a photon can bring the molecule from the ground state S_0 to some vibrational state of S_1. For dyes the dipole moment matrix element μ is very large, because the external elec-

(a) Pyridine 2   **(b)** Styryl 9M
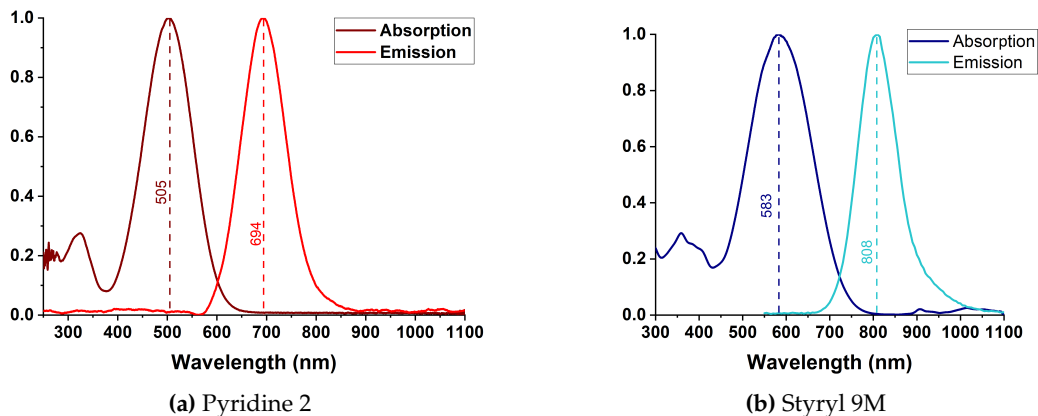
Figure 2.20: Emission spectra of laser dyes diluted in ethanol with a concentration of about $1\,\text{mM}$ and illuminated by second harmonic ($\lambda = 532\,\text{nm}$) of Q-Switched ns pulsed Nd:YAG laser.

trons move on the whole dimension of the molecular chain, L, which is very long. Given that $\mu \sim eL$, the absorption cross-section σ_a, which is proportional to $|\mu|^2$, is also high ($\sim 10^{-16}\,\mathrm{cm}^2$). Once promoted to the excited state, the molecule decays non-radiatively in a very short time ($\tau_{nr} \simeq 100\,\mathrm{fs}$), due to collisions, to the lowest vibrational level of S_1. From here, then, it falls to some vibrational level of S_0, always respecting the selection rules, with emission of photons. Due to the small spacing between the vibrational levels (at the order of $K_B T$ at room temperature), the fluorescent emission shows a spectrum with a wide band and without structures. This occurs at wavelengths greater than the absorption band (Stokes shift), for the non-radiative decay in S_1. Then, the system in an exited vibrational state of S_0 will then return to its fundamental state with another very fast non-radiative decay, ($\tau_{nr} \simeq 100\,\mathrm{fs}$). Moreover, due to the high value of the matrix element of the dipole moment, μ, the transition $S_1 \to S_0$ has a high cross-section, which increases the probability of the stimulated emission process.

It should be noted that when the molecule is on the lowest level of S_1, it can also decay to the state T_1. This process is indicated as *intersystem crossing*, prohibited for radiative transitions by selection rules, but molecules can decay in state T_1 by collisions, which preserve the spin total number of participants. Similarly, the transition $T_1 \to S_0$ starts for resonant energy transfer in collisions with species present in solution, e.g. oxygen. When the molecule is on the T_1 level it can absorb radiation and transit at the T_2 level. This absorption tends to occur at the same wavelength region of the stimulated emission and, therefore, constitutes a serious obstacle to laser action. The three decay processes considered ($S_1 \to S_0$, $S_1 \to T_1$, $T_1 \to S_0$), which occur from the exited states of the molecules can be characterized by the following constants: τ_{sp} is the lifetime of spontaneous emission for $S_1 \to S_0$; k_{ST} is the rate of the intersystem crossing transitions $S_1 \to T_1$ and τ_T is the lifetime of the state $T_1 \to S_0$. Indicating with τ the total lifetime of the state S_1, we have:

$$\frac{1}{\tau} = \frac{1}{\tau_{sp}} + k_{ST} + \frac{1}{\tau_T} \tag{2.6}$$

Due to the high value of μ, τ_{sp} falls in the region of ns. Given that k_{ST}^{-1} is generally longer ($\sim 100\,\mathrm{ns}$), most of the molecules decay from S_1 as fluorescence. The average triplet state lifetime, τ_T, depends on the dye solution and, in particular, on the amount of dissolved oxygen: it varies from $10^{-7}\,\mathrm{s}$ in oxygen-saturated solutions, to $10^{-3}\,\mathrm{s}$ in deoxygenated
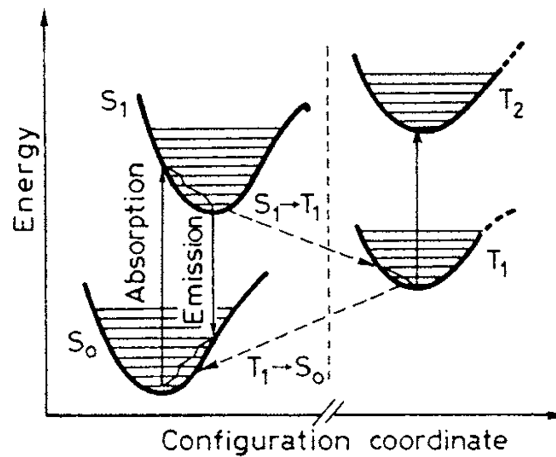
Figure 2.21: Schematic representation of energy levels of a laser dye [101].

solutions.

Bleaching

Another phenomenon that affects dye molecules is *bleaching*. This is due to the change in the molecular structure that leads to become transparent to the visible radiation, and then the decrease of quantum yield (eq. 1.5). The environment in which the molecules are embedded, such as the solvent or the matrix that hosts them and the impurities that may be present in the surrounding environment is responsible for bleaching.

In our case, as the dye molecules are subjected to a relatively high photon flux, the bleaching process that becomes important is that of *photobleaching*. The incident photon flux can activate photochemical reactions of the dyes with the surrounding environment.

It has been experimentally verified that this phenomenon is mediated by a single photon and occurs in the case in which the molecules are in the excited singlet or triplet state [102]. Furthermore, the oxygen present as an impurity in the environment, due to the porosity of the matrix or the polymerization process, is the main cause of photobleaching. In particular, the probability of a molecule that is in a triplet excitation state to interact with the surrounding environment is high due to its long lifetime, for example via the reaction $T_1 +^3 O_2 \rightarrow S_1 +^1 O_2$ [103, 104].

In order to make sure that the photobleaching phenomenon is not a problem in our devices, we perform long exposure measurements on the dyes used, reported in section 4.2. In particular we pay attention to the dye doped film where this phenomenon can become so important as to preclude the operation of the device.

Liquid State System

The dye is diluted in a solvent with a concentration of $\sim 1\,\mathrm{mM}$ in order to avoid the quenching of the emission. This quenching is due to the non-radiative energy transfer between dye molecules. The major contribution is made by Förster resonance energy transfer (FRET) and Dexter energy transfer (DET). FRET is based on classical dipole-dipole interactions between the transition dipoles of the molecules and is extremely dependent on their distance, R, falling off at a rate of $1/R^6$. DET is a short-range phenomenon that falls off exponentially with distance $\propto e^{-cR}$ and depends on spatial overlap of molecular orbitals. Generally, Dexter mechanism is less important than the Förster mechanism which can typically occur over distances up to a few nm [105]. With a concentration of $1\,\mathrm{mM}$ the average distance between dye molecules results $\sim 12\,\mathrm{nm}$, over the limit of quenching distance, due to the Förster or Dexter mechanisms.

In order to contain the dye solution on the nanoarray, a small chamber formed by a double-sided adhesive tape and a coverslip was created over each samples. The tape (Scotch$^{®}$ 3M) has a thickness of about $200\,\mu$m and defines the thickness of the chamber and consequently that of the active medium. One side of the chamber is open so as to allow the filling of the dye.

Solid State System

We also took into account the possibility to synthesize solid state devices, by embedding dye molecules in a polymer matrix. A solid state system is very useful in terms of integrability in optical circuits, and makes the devices more stable and compact with respect to a liquid state system. In order to synthesized a polymer film above the nanostructures,
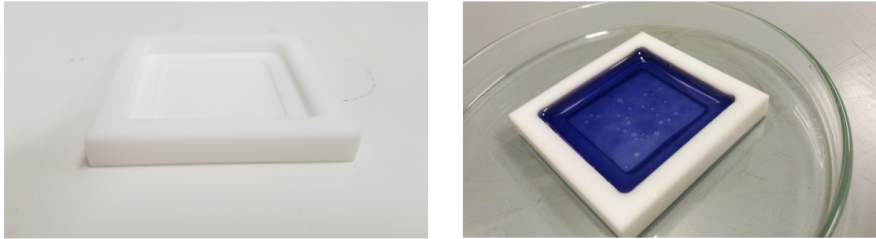
Figure 2.22: Photos of the deposition pool used to form the dye-doped polymer film.

dye is dissolved in acetone at the concentration of $\sim 4 \times 10^{-4}$ M. Polymethyl methacrylate (PMMA) with average Molecular weight (MW) of 35000 g/mol produced in beads by *Sigma-Aldrich*, is dissolved in acetone at 10% in weight.
The two solutions are mixed in proportion 1:3 in order to create a solution of Styryl 9M molecules and PMMA monomers dissolved in acetone with a dye concentration of about 10^{-4} M.

A teflon little pool with a volumetric capacity of 3 ml is fabricated in order to contain the solution during the solidification of the dye-doped film. The sample is then placed into the pool with 2 ml of the liquid solution by a microlitre pipette and left to dry for about 12 hours at room temperature. High temperature or UV exposure could damage the nanostructures or the dye molecules, for this reason room temperature evaporation of the solvent was chosen.

Homogeneous dye-doped films with a thickness of about 100 μm and a concentration of the order of mM are formed in contact to the plasmonic nanostructures. Obviously, the larger it is the volume of solution that is poured on the sample, the thicker becomes the thickness of the dye-doped film.

Furthermore, it is possible to create self-standing samples by carefully lifting the dye-doped polymeric film: detaches from the substrate bringing with it the nanostructures, thus maintaining the system's plasmonic properties.

Chapter 3

Characterisation of Nanostructured Arrays

In this chapter we will present the main morphological and linear optical properties of the nanostructured samples, synthesized as described in the previous chapter. Firstly, we will present the used instrumentations and setups, then a discussion of the used simulation techniques will be given, and finally we will present and discuss the result obtained for this characterization part.

From this point, the measurements display are referred to a specific sample with the characteristic reported in table 3.1. Moreover, we label this sample with an acronym as

- **NDoA**: nanodome array

- **NDiA**: nanodisk array

Table 3.1: Parameters of the samples

	Lattice constant (nm)	Diameter (nm)	Thickness (nm)
NDoA	522	490	70
NDiA	340	150	70

3.1 Morphological Characterization

Morphological investigation is performed by *Scanning Electron Microscopy* (SEM) and *Atomic Force Microscopy* (AFM).

SEM is a microscope that uses electrons instead of photons as in normal optical microscopy. We used a Zeiss *Field-emission SEM (FE-SEM)*, figure 3.1a, whose resolution can range from 2.5 to 0.8 nm depending on the acceleration voltage that varies from 200 V to 30 kV. By a cold field effect gun, electron beam is generated, then a series of apertures and electromagnetic lenses directs and focuses the electron beam on the sample. The electrons are also accelerate at a certain energy, which set the resolution, by a voltage imposed in the acceleration column where also lenses work. The image is then reconstructed by the electrons that come from the interaction with the sample. First, back-scattered electrons (BSE) are produced by the elastic scattering with atomic nuclei of the sample. These electrons carry information about atomic Number Z of the sample. Moreover, secondary
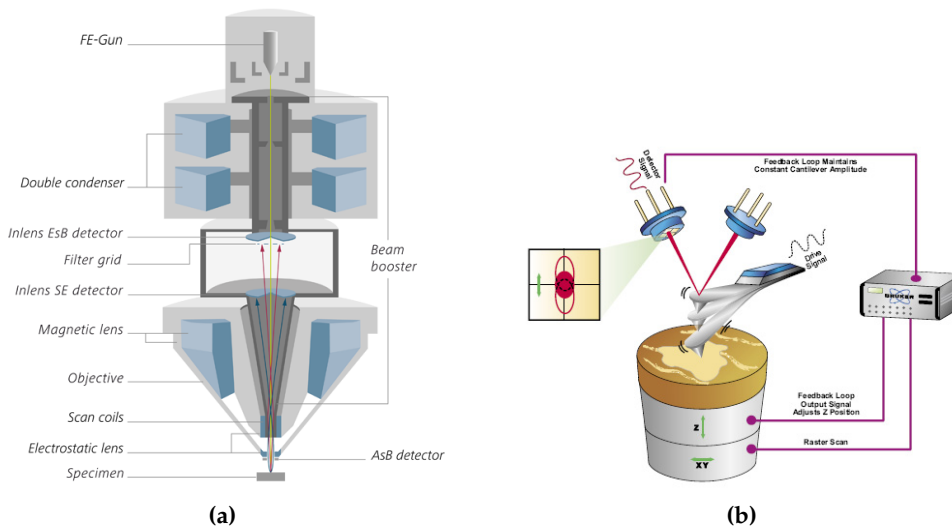
Figure 3.1: (a) configuration of the used SEM [106]. **(b)** Sketch of the AMF in semi-contact mode [107].

electrons (SE) that come from the sample surface atoms are created by inelastic scattering: they are less energetic than the back-scattered ones and give information from the firsts nm of the sample surface. Thus, they are used to form morphologically-sensitive or topographical images. Others phenomena occur in the interaction process, whose decay produces other signals, such as X-rays that come from the transitions of the electrons in the sample atoms upon inner shell ionization or the emission of Auger electrons, more likely to occur in lighter elements. X-rays are used for compositional analysis, whereas Auger electrons are typically not used in SEM.

Secondary electrons that come from the interaction are collected primarily by the in-lens detector placed in the acceleration column and by an additional electron detector, the Everhart-Thornley detector, placed in the SEM chamber and generally tilted at $45°$. The in-lens detector collects the secondary electrons which are generated by the direct interaction with the incident beam and so they carry the highest spatially risolved information. Therefore, the in-lens detector is generally the most used for imaging. An X-ray detector is also present together with a BSE detector exactly at the exit of the objective lens as in figure 3.1a. Furthermore, columns and the camber are kept in a high vacuum of $\sim 10^{-6}$ mbar during the measurements, while the gun is always kept at $\sim 10^{-9}$ mbar in order not to damage the gun and to allow the electrons to reach the sample and detectors.

Additional three-dimensional information about the morphological sample surface structure was obtained by using a *NT-MTD Solver PRO AFM*. This is a type of scanning probe microscopy (SPM) and acquires information about surface morphology by a nanometric sharp tip placed in a cantilever. In the semi-contact mode, figure 3.1b, as the one we work with, the cantilever is forced by a piezoelectric system to oscillate, showing a resonant response as a function of the frequency. Placed in the natural resonance frequency, the measurements are acquired by recording magnitude or phase change in the resonance frequency due to the Van der Waals forces between tip and the sample.

Data are then elaborated by Gwyddion software [108], which is a modular program for scanning probe microscopy data visualization and analysis. AFM is widely used in combination with SEM because it gives information on the depth of images, i.e. on the height

Source →

Sample

Beam
stopper

Beamsplitter

Detector
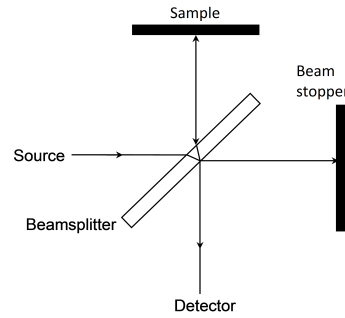
Figure 3.2: Scheme of the reflection measurements made with normal incidence and collection.

of the nanostructures. Therefore, when required, SEM and AFM are used together to obtain accurate three-dimensional information.

3.2   Optical Characterization

Optical characterizations are particular relevant in our case, because they give information on the interaction with the radiation, and allow us to investigate plasmonic properties of the samples and characterize them with the support of numerical simulations. Optical investigation is done to study LSPRs of the nanostructures and the SLR of the plasmonic arrays considered. These two phenomena are responsible for the near field enhancement that we are looking for, which is coupled with the dye molecules in order to enhance the stimulated emission and to promote the lasing emission.

For the optical investigation a Jasco V-670 and an Ocean Optics spectrometer have been used. Thanks to the versatility of Ocean Optics spectrometer we can perform also reflectance measurements at normal incidence in an easy way with the help of a beam-splitter as described in figure 3.2. A silver mirror is used as reference for these measurements. Generally, these types of measurements are useful for nanodome arrays that exhibit a stronger response in reflection (R) than in transmission (T), even if information can be extrapolated from both as we will see later.

Furthermore, in order to study the dispersion behaviour of lattice modes in the reciprocal space (section 1.2.3), i.e., Rayleigh anomalies and SLRs of metal nanoparticle arrays, angle-dependent measurements are needed. Changing the incident angle, θ, implies changing the parallel component of the incident wavevector $k_{//inc} = k_{inc}\sin(\theta)$ on the Bragg condition (eq. 1.53). Transmittance or reflectance spectra, as a function of θ, give the possibility to reconstruct the dispersion of the diffractive modes, from the coupling of the beam with the plasmonic lattice, also showing the coupling with the SLR mode. To this aim, different instrumentations have been used.

Thanks to the collaboration with UNAM (National Autonomous University of Mexico, Mexico City, Mexico), a high precision angular instrument composed of two motorized goniometers has been used, showed in figure 3.3a. The two motorized goniometers are mechanically disjointed and placed one above the other. One controls the rotation of the sample holder, the other the collection setup. As a sample holder, we used a manual goniometer placed in the rotation pivot of the two motorized goniometers, with the rotation axis in the direction of the incident beam.
For the sake of clarity, we define the axis $\hat{z}$ as the propagation axis of the light beam;

the sample placed orthogonally to the beam and in the rotation plane of the manual go-niometer is therefore in the plane $\hat{x}\hat{y}$ and can rotate on this plane of the angle ϕ. This degree of freedom is chosen in order to orient the sample along the lattice symmetry directions. The motorized goniometer then lies on the plane $\hat{x}\hat{z}$. This allows the rotation of the tilt angle θ of the sample with respect to the incident beam axis, controlling the projection of the wave vector k_{inc} on the lattice plane. The other motorized goniometer supports an arm on which the collection setup is mounted. It consists of a polarizer, an iris and a lens, which focuss the beam on the head of an optical fiber that carries the signal to the detector (Ocean Optics 2000+). The arm is free to rotate independently, allowing it to be held in place during transmission measurements and to move during reflection measurements.

The white light, produced by a lamp source, is driven to the sample by two mirrors after passing through a polarizer and a pinhole. This defines the dimensions of the light beam at a diameter of about 2 mm.

The other measurement setup, showed in figure 3.3b, is similar to the previous one and installed at our lab at DFA. The operating principle is the same, however this one doesn't allow measurements in reflection due the lack of the second goniometer which should host the collection setup. By using DH-2000 BAL Ocean Optics source, the light from the output fiber is collimated by lenses and polarized before reaching the sample. After the interaction with this one, the transmitted light is collected by a lens and focused into an optical fiber that drives the beam in the HR4000 Ocean Optics detector.

To reconstruct Rayleigh anomalies in our ordered arrays we used also a RC2® Ellipsometer produced by J.A. Woollam Co. Even if this is an ellipsometer, its accurate management of angles for reflection measurements gives the possibility of being used to identify the diffractive properties of a periodic system.
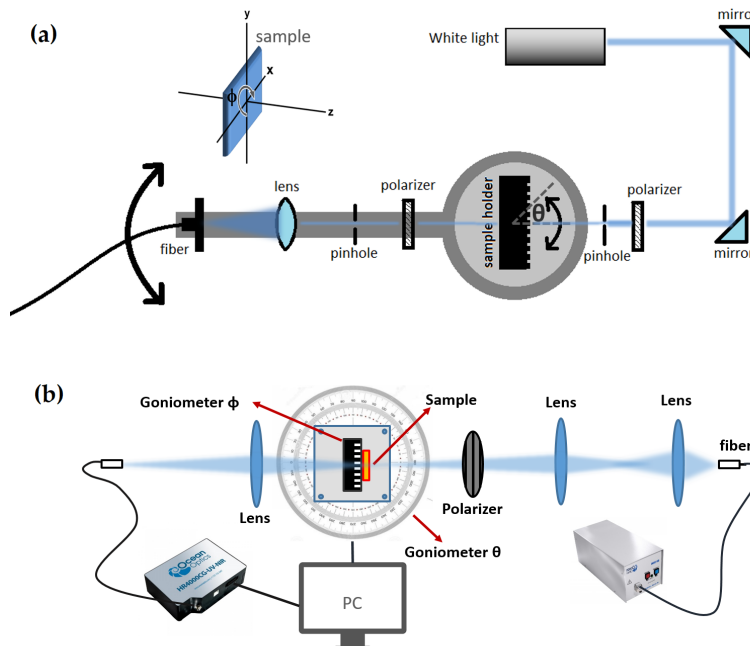
Figure 3.3: Schematic setup for angle-resolved optical characterization: **(a)** two goniometers version used at UNAM and **(b)** single-goniometer version installed and used at DFA.

3.3 Numerical Simulations of the Optical Properties

To better interpret the experimental results, the *finite element method* (FEM) technique has been adopted to study the interaction between EM field and the naoarrays. In fact, analytical solutions to the problem of the interaction between light and nanostructures can only be found for simple and highly-symmetric geometries, such as spheres [51] or ellipsoids [109] but also multilayer films [110, 111], but not for the more complex nanostructures investigated in this work.

The FEM technique [112] discretizes a space domain in small cells, called finite elements, and solves for every node of the cells the equations. In this work, FEM works in the frequency domain (*Finite Difference Frequency Domain* (FDFD)) because the computational speed is faster than the time domain (FDTD) one for the considered problems. In the FDFD the *Helmholtz equation* is solved with standard boundary conditions. Helmholtz equation derives directly from the wave equation, assuming, in all generality, a harmonic dependence of the electric field $\mathbf{E}$, i.e., $\mathbf{E}(\mathbf{r}, t) = \mathbf{E}(\mathbf{r})e^{-i\omega t}$, so

$$\nabla^2 \mathbf{E} + k_0^2 \, \varepsilon \, \mathbf{E} = 0 \tag{3.1}$$

where $k_0 = \omega/c$ is the wave vector of the propagating wave in vacuum and ε is the frequency dependent dielectric function.
The method transforms the problem in a linear system or matrix, with a Helmholtz equation for each node, and solves this system with a linear solver. The computational effort is limited by the fact that a node is influenced only by nearby nodes.

To this aim, a commercial software platform for 3D finite element simulations is used: COMSOL Multiphysics®. This allows to study both near-field and far-field responses of the nanostructure undergoing to a monochromatic EM wave. Different wavelengths imply different and independent FEM computations, giving the possibility to parallelize the simulation by computing independently different wavelengths on different CPU cores. Therefore, a dedicated server, AMD Opteron 6274 server (4 CPU, 32 cores, 128 GB RAM) is used for FEM simulations. Moreover, for this work, a direct liner solver, PARDISO [113], is chosen, thanks to its sequential and parallel sparse numerical factorization performance, which is the most indicated for single machine computations, as in our cases.

For this work, this powerful resource is used principally as a support to experimental measurements, in order to study the near-field behaviour of the main plasmonic resonances which occur in our systems. Furthermore, FEM simulations are used to design a new sample generation that we will discuss after some considerations on the principally studied samples.

3.4 Au NanoDome Array

Morphological characterization of Au nanodome arrays (Au NDoA), whose nanofabrication was made by PS NSs with diameter $D = 522$ nm and described in section 2.4, is generally made by SEM. Due to Au nanodomes morphology, AFM measurements do not give us too much information, since the gap between neighbour domes is around 30 nm and the AFM tip cannot reach the bottom even in the interstices. However, AFM results very useful to measure nm-thick deposited films with a high precision of about 1 nm.
The thickness of silica layer is estimated around 200 nm, while for gold it varies between $50 - 70$ nm, depending on the sample. The gap between neighbour domes is measured
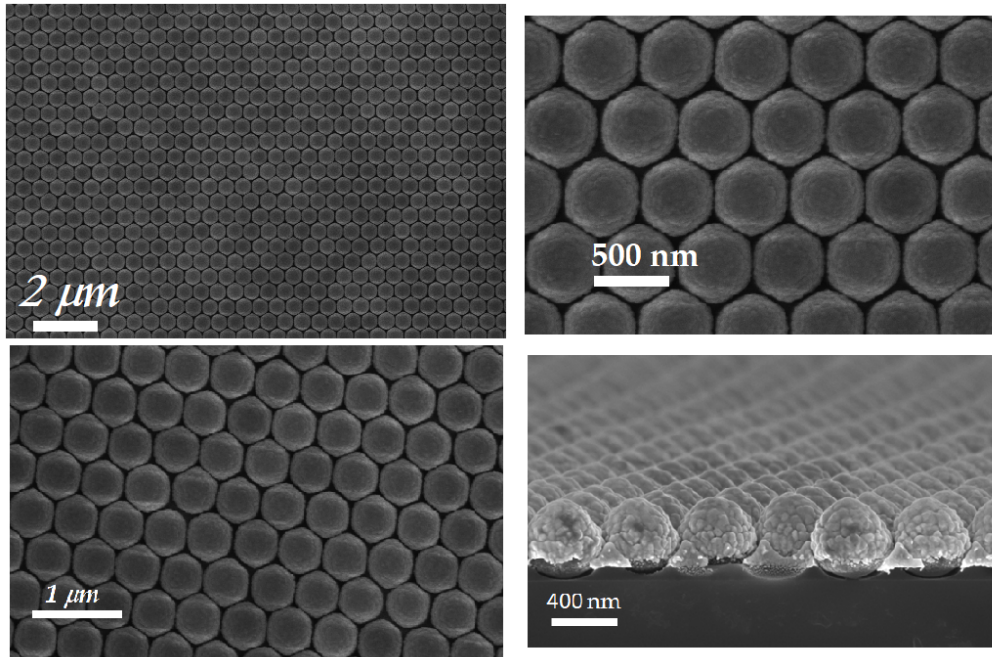
Figure 3.4: SEM images of Au NDoAs synthesized in top view and cross section.

by SEM images, and some examples are shown in figure 3.4. Using ImageJ software, the average radius of Au nanodomes is estimated around 490 nm for our samples.

More interesting measurements for our purpose are the optical ones, in particular the angle-dependent ones. An example of measurements made by Jasco and Ocean Optics in the configuration showed in figure 3.2 are reported in figure 3.5.

Since the nanostructures have to be coupled with a gain medium, which has a certain refractive index, the optical measurements are performed with various media upon the nanoarrays. The results show different responses with different refractive index of the media, as predicted from the polarizzability (eq. 1.46).

Since wavenumber in a medium with refractive index n is $k = k_0 n$, where k_0 is the wave number in the free-space, the Rayleigh anomalies are modified by n which goes in the Bragg condition. In this case with a constant lattice of $a = 522$ nm, considering the first neighbours distance at normal incidence, the Rayleigh anomaly comes for $\lambda = \frac{\sqrt{3}}{2} a = 452$ nm in air or vacuum. If we consider ethanol (EtOH) $n_{EtOH} \sim 1.36$ and PMMA $n_{PMMA} \sim 1.49$, the wavelength of the anomaly will be at 615 nm and 674 nm, respectively.

In figure 3.5a absorbance spectra are showed with different media. The black line represents the spectrum with Au NDoA in air, blue line in ethanol and red with a PMMA film. In the spectra blue and red, the Rayleigh anomalies can be connected to the minima of absorbance corresponding to $\lambda = 618$ and 678 nm, respectively. Peaks at $\lambda = 727$ and 763 nm, respectively, could be linked with SLRs considering also their asymmetric shape. Furthermore, reflection measurements are reported in figure 3.5b as $1 - R$. Considering the sample in ethanol (blue curve), we note a peak at 697 nm, that can be interpreted with further investigation. In fact, the simple spectrum at normal incidence does not give enough information to optically characterize the structure. For this reason, angle-dependent measurements are performed. Figure 3.6 shows the results obtained. Here
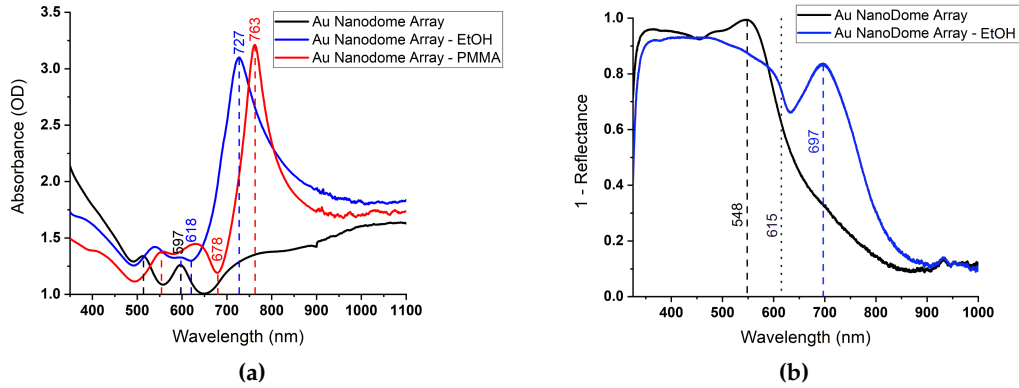
Figure 3.5: Au NDoA: **(a)** absorbance spetra in different media: air (black), ethanol (blue), PMMA (red). **(b)** $1-$ reflectance in air (black) and ethanol (blue) at normal incidence.

measurements are reported as extinction $Ext = 1 - T$ and show the contribution of scattering and absorption of the sample. Moreover, measurements are performed in transverse magnetic (TM) (p-polarization) and transverse electric (TE) (s-polarization) (fig. 3.6a) modes, in different symmetry directions ΓK (fig. 3.6b) and ΓM (fig. 3.6c) of the reciprocal space hexagonal unit cell and with ethanol (fig. 3.6d) as a medium.

By comparing TE and TM modes, figure 3.6a and figure 3.6c for example, it is clear that the system interacts mainly with the incident light in TM than in TE mode. The different symmetry directions ΓK, in figure 3.6b, and ΓM, in figure 3.6a, are characterized by different slopes of the Rayleigh anomalies, well recognizable in figures. Furthermore in ΓM direction, the interaction generates narrower features with respect to ΓK direction.

If ethanol is placed over the Au NDoA, in figure 3.6d, the anomalies redshift of a factor n, and interesting features arise from the coupling between lattice and plasmonic properties. The spectrum (blue line) in figure 3.5a is the equivalent measurement done at 0 degree in the map, and we can recognize some features, such as the dip (blue zone) and the peak (red zone). From this, we can deduce the hybrid nature of the resonant mode due to the interaction with the anomalies (photonic) and plasmonic mode of the particles. Figure 3.6e shows the extinction measurement with ethanol in TM mode and in ΓM direction in energy ($E = \frac{\hbar c}{n} k_{//}$) as a function of the parallel component of the incident wavevector $k_{//i}$. Over the map, the Rayleigh anomalies are plotted and labelled by the corresponding Miller indices, showing a good matching with the theoretical lattice mode derived by the dispersion law.

Reflection measurements are also performed by ellipsometry in TM mode with the sample in air and in ethanol and the results are showed as $1-$ reflectance in figure 3.6f and 3.6g, respectively.
The maps are plotted in energy versus parallel wavevector and the Rayleigh anomalies are superimposed. Ellipsometry can measure the specular reflection from the sample and not all the scattering, and in our system the minimum angle measurable is 15 deg from the sample normal.
Similarly to the extinction measurements, $1 - R$ maps show minima following the lattice modes and a close redshifted peak follows these modes showing an interaction with them. Therefore the peak showed in figure 3.5b at $\lambda = 697$ nm in the sample in ethanol (blue curve) can be linked with the hybrid mode shown in the reflection map (fig. 3.6g).

(a) Extinction TE ΓM

(b) Extinction TM ΓK

(c) Extinction TM ΓM

(d) Extinction TM ΓM in EtOH

(e) Extinction TM ΓM in EtOH, Energy vs $k_{//i}$

(f) $(1-$ Reflectance$)$ TM $K\Gamma$ and ΓM

(g) $(1-$ Reflectance$)$ TM $K\Gamma$ and ΓM in EtOH
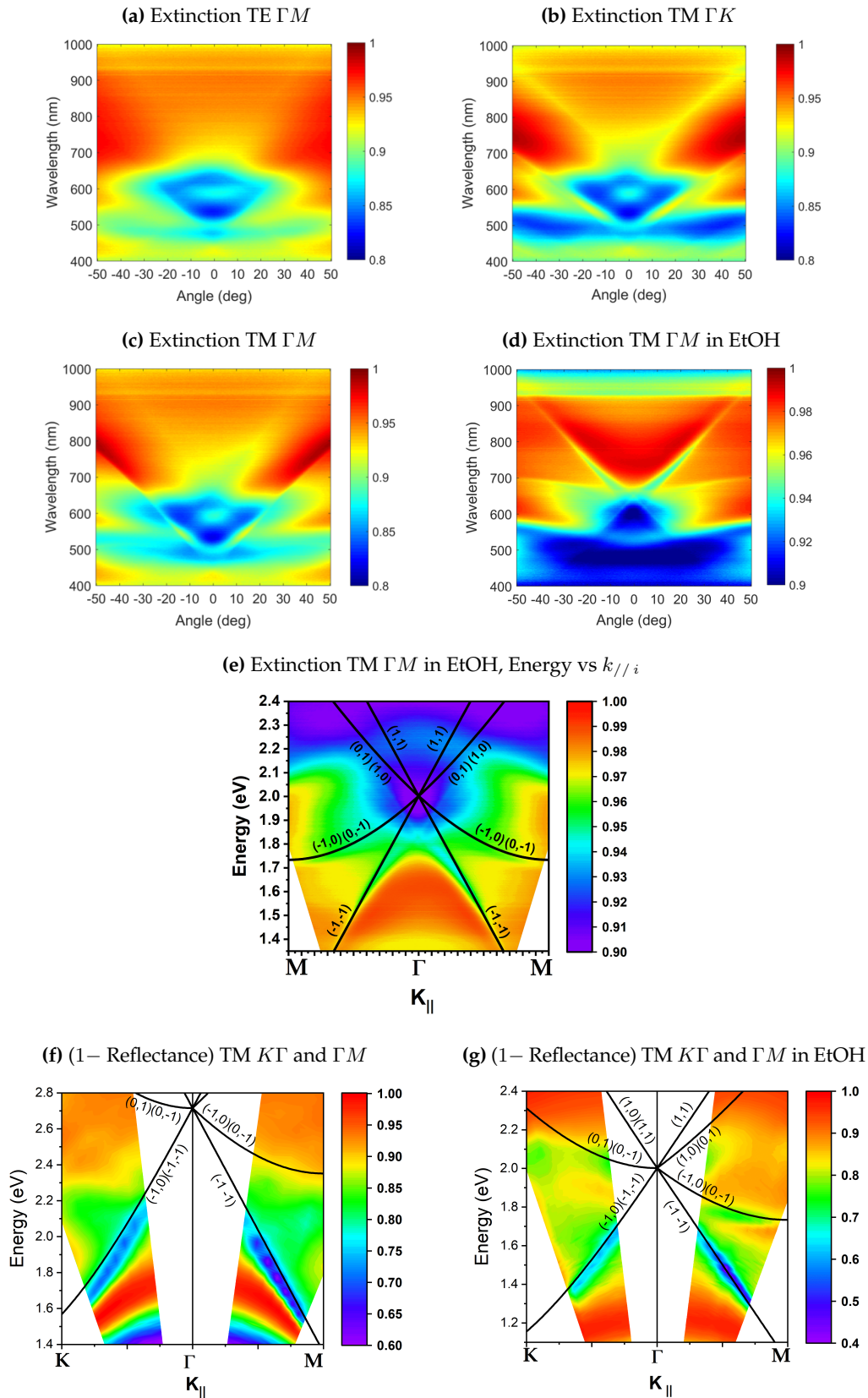
Figure 3.6: Au NDoAs: Extinction spectra as a function of angle of incident beam in TE (**a**) and TM modes, in different symmetry directions ΓK (**b**) and ΓM (**c**), in air and in ethanol (**d**). (**e**) Extinction map in TM mode, ΓM direction in ethanol represented in diffracted photon energy as a function of parallel component of incident wave vector $k_{//i}$, Rayleigh anomalies are superimposed and labelled by respective Miller indices. $1-$ Reflectance in TM mode made by ellipsometer in air (**f**) and in ethanol (**g**) in the direction ΓK and ΓM, the Rayleigh anomalies are superimposed.

In order to better characterize the resonance modes, numerical simulations are performed.

3.4.1 FEM Simulation Results

The numerical simulations are performed with the software COMSOL Multiphysics$^{\circledR}$. The used 3D model is sketched in figure 3.7. For modelling simplicity a hexagonal prism is chosen, instead of rhombic primitive cell, to simulate the two-dimensional lattice of nanostructures, with periodic boundary condition (PBC) on the six lateral faces: each face has a PBC condition with its opposite. The model has *perfectly matched layers* (PMLs) on the top and bottom, in the $\hat{z}$ direction. PML is an artificial absorbing layer placed on open borders in order to avoid numerical reflection during the computational process [81].

Geometric parameters used in the simulations are reported in figure 3.7b. The distance between two opposite lateral faces is equal to the lattice constant $a = 522\,\text{nm}$, while the hexagonal unit cell has a side length $L_{hex} = a/\sqrt{3}$. The dome geometry is simplified by a silica semi-sphere centered at $(0, 0, 50\,\text{nm})$ with a diameter of $390\,\text{nm}$ and covered with a $50\,\text{nm}$ thick Au layer with a final diameter of $490\,\text{nm}$. In order to model the real structure, the space between domes is filled by a Au layer $50\,\text{nm}$ thick that creates a single continuous metallic layer of Au as shown in figure 3.7.

Under the dome, the substrate is modelled as $400\,\text{nm}$ thick SiO_2 layer and, on the upper semispace, the medium is modelled by $1\,\mu\text{m}$ thick non-absorbing material with a certain refractive index.

Furthermore, the edges of Au domains are slightlyrounded in order to avoid unphysical EM hot spots in the geometry that can distort the simulation result. The dielectric function of Au used in these simulations is derived experimentally by ellipsometric measurements. SiO_2 is modelled by a non dissipative material with a refractive index $n = 1.45$.

The simulation is performed in the wavelength range from 400 to $1200\,\text{nm}$. The incident beam is a plane wave with amplitude $E_0 = 1\,\text{V/m}$.

The absorbance spectrum, showed in figure 3.8a, exhibits a minimum at $\lambda = 615\,\text{nm}$

(a)   **(b)**
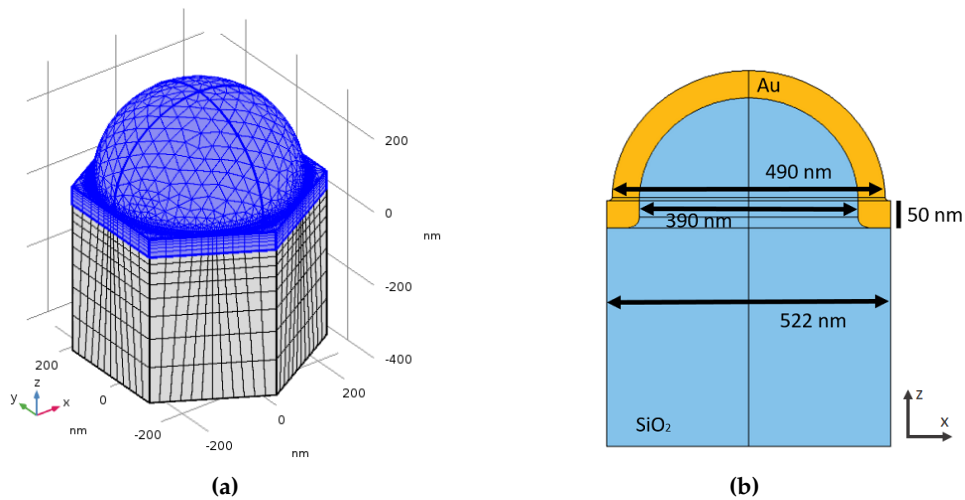
Figure 3.7: (a) 3D model used for Au nanodome array FEM simulations: the nanodome is highlighted and the mesh is also shown. **(b)** Main geometric parameters used in the simulation: the sketch shows the $\hat{x}\hat{z}$ plane at $y = 0$.
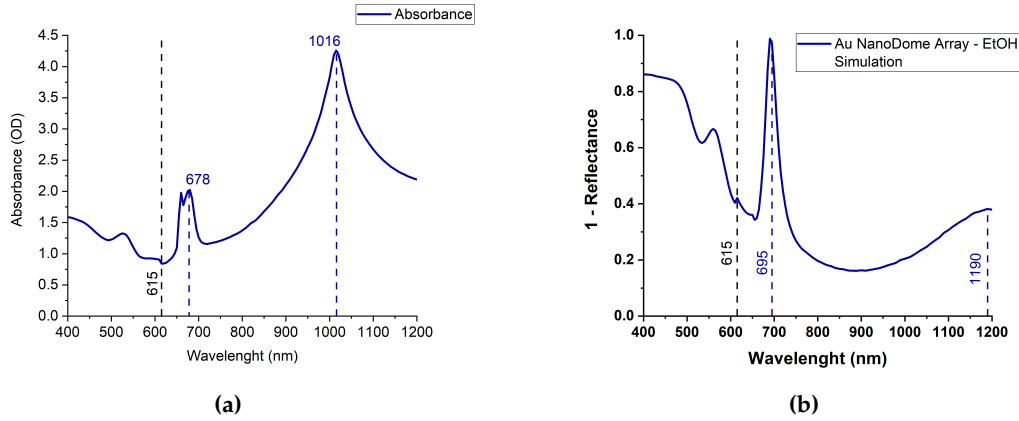
Figure 3.8: Normal absorbance (**a**) and $1-$ Reflectance (**b**) spectra resulted from numerical simulation of Au NDoA.

and the next peak at $680\,\mathrm{nm}$ that can be linked with the peak in the absorbance spectra even if is very redshifted.

The simulated spectrum reproduces qualitatively the main features showed in the experimental spectra, although the simplified geometry used in the simulation with respect to the real one does not allow a quantitative agreement. The reflectance response gives more interesting results because it can be directly compared with the experimental results. In fact, a peak arises at $695\,\mathrm{nm}$ very close to the experimental peak. Moreover, another peak at $1190\,\mathrm{nm}$ is present and can be associated with dipole plasmon resonance of single nanoparticle. This can be deduced by the field distribution near to the metallic nanostructure.

Figure 3.9 shows the electric field distribution for normal incidence $\mathbf{k} = (0, 0, k)$ and $\mathbf{E} = (E_0, 0, 0)$ in the planes $\hat{x}\hat{z}$ at $y = 0$ and $\hat{x}\hat{y}$ at $z = 80\,\mathrm{nm}$ in order to avoid edge. In particular, the field enhancement $|\mathbf{E}|/E_0$ and the component $\hat{z}$ of the electric field E_z/E_0, perpendicular to the lattice plane, are plotted. The interest in the field component, E_z arises because it is generated by plasmon resonances at the dome interface.

Figures 3.9a (plane $\hat{x}\hat{z}$) and 3.9c ($\hat{x}\hat{y}$) show the field enhancement due to the surface lattice resonance associated to the peak at $\lambda = 695\,\mathrm{nm}$. Figures 3.9b ($\hat{x}\hat{z}$) and 3.9d ($\hat{x}\hat{y}$) show E_z at the same wavelength.

In the same configuration figures 3.9e, f, g and h show the field enhancement and E_z respectively, at $\lambda = 1190\,\mathrm{nm}$.

By looking at the field distribution we note a field confinement close to the nanostructure, and a difference between the two resonances. The first one has less confinement, confirming the hybrid nature of this plasmonic resonance and can be thus linked to the SLR of the plasmonic lattice. On the other hand, the second one is more confined and the field distribution confirms the association with dipole plasmon resonance of the plasmonic structure.

3.5 SiO$_2$ NanoDome Array

SiO$_2$ nanodome arrays (SiO$_2$ NDoAs), whose nanofabrication is described in section 2.4, are made in order to study the lattice contribution switching off the plasmonic properties

(a) Side view ($\hat{xz}$, $y = 0$) of near field enhancement $|\mathbf{E}|/E_0$ at $\lambda = 695\,\text{nm}$
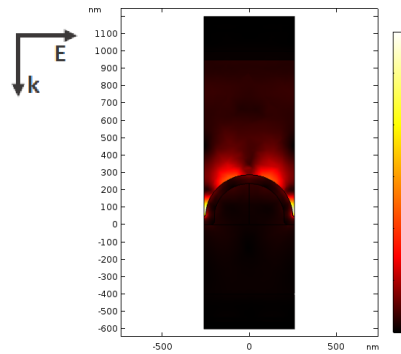
(b) Side view ($\hat{xz}$, $y = 0$) of E_z/E_0 at $\lambda = 695\,\text{nm}$
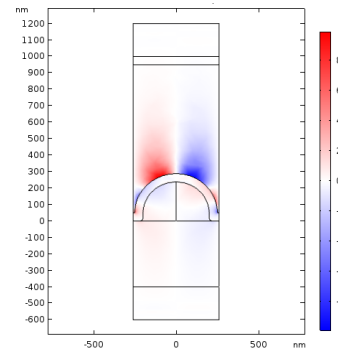
(c) Top view ($\hat{xy}$, $z = 80\,\text{nm}$) of near field enhancement $|\mathbf{E}|/E_0$ at $\lambda = 695\,\text{nm}$
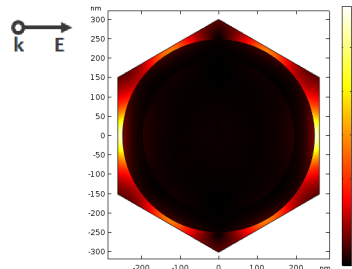
(d) Top view ($\hat{xy}$, $z = 80\,\text{nm}$) of E_z/E_0 at $\lambda = 695\,\text{nm}$
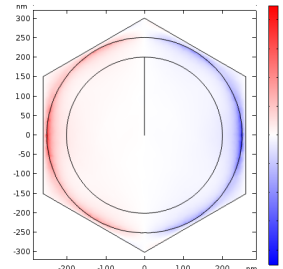
(e) Side view ($\hat{xz}$, $y = 0$) of near field enhancement $|\mathbf{E}|/E_0$ at $\lambda = 1190\,\text{nm}$
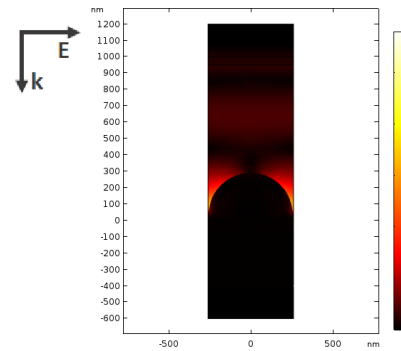
(f) Side view ($\hat{xz}$, $y = 0$) of E_z/E_0 at $\lambda = 1190\,\text{nm}$
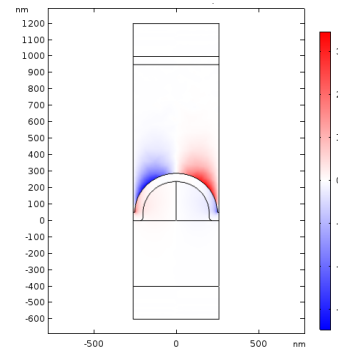
(g) Top view ($\hat{xy}$, $z = 80\,\text{nm}$) of near field enhancement $|\mathbf{E}|/E_0$ at $\lambda = 1190\,\text{nm}$
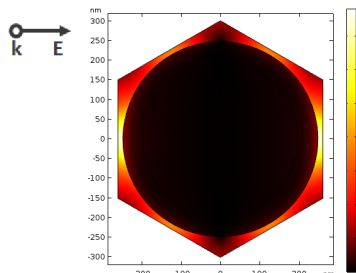
(h) Top view ($\hat{xy}$, $z = 80\,\text{nm}$) of E_z/E_0 at $\lambda = 1190\,\text{nm}$
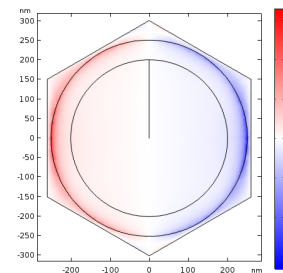
Figure 3.9: Simulation of electric near-field distribution of an Au nanodome array.
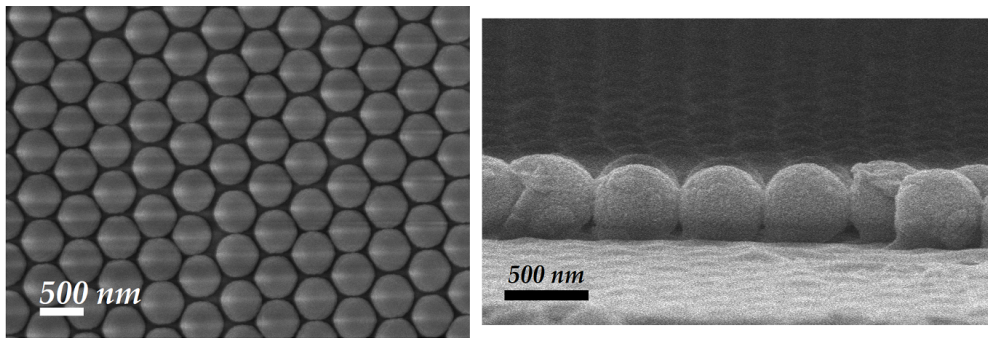
Figure 3.10: Various SEM images of different SiO$_2$ nanodome arrays synthesized in top view and cross section.

of the metallic structure. The shape and dimensions of SiO$_2$ nanodomes are similar to the Au nanodomes in order to give a response as similar as possible to the geometrical contribution of the Au nanodome array. For this reason, only the last step of the nanofabrication is changed, by depositing a SiO$_2$ layer with the same thickness of the Au layer. SEM images of the resulting SiO$_2$ NDoAs are shown in figure 3.10 in top and cross view. From these, by ImageJ software, a mean diameter of SiO$_2$ domes is estimated and has to result near to 490 nm.

On the other hand, optical measurements are important to understand the behaviour
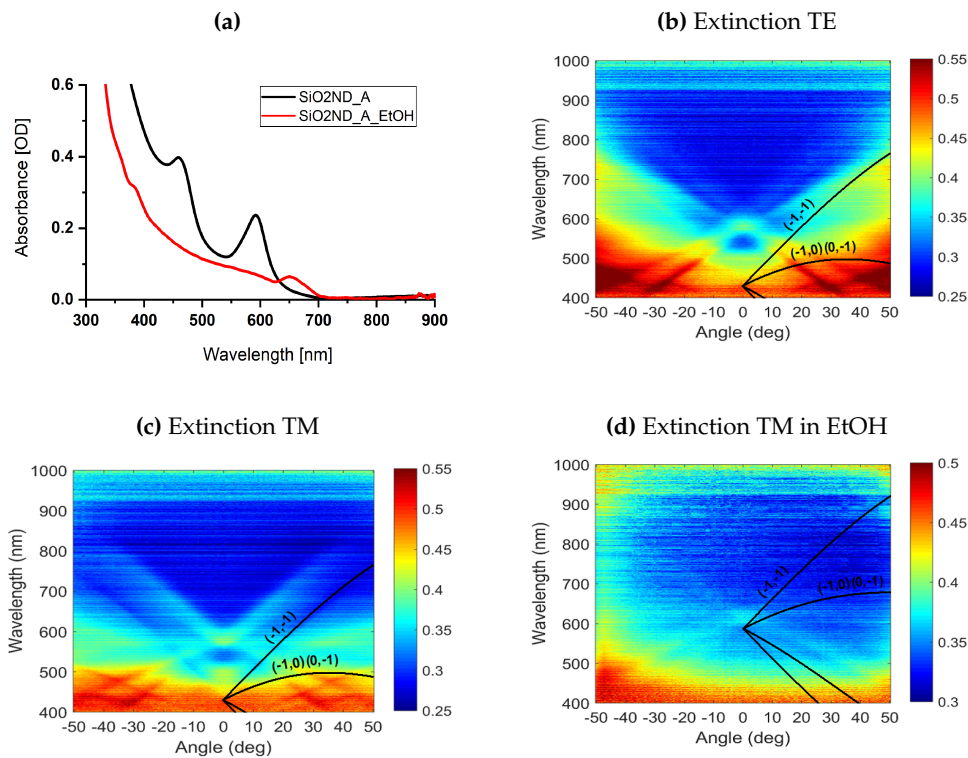
Figure 3.11: SiO$_2$ NDoA: **(a)** absorbance spectra in air (black curve) and in ethanol (red curve). The other figures are Extinction maps, with Rayleigh anomalies superimposed: **(b)** in TE mode, **(c)** in TM mode and **(d)** in TM mode with ethanol over the nanodomes.

of the lattice part. The results are shown in figure 3.11.

Figure 3.11a shows absorbance spectra of a SiO_2 nanodome array in air and ethanol. SiO_2 NDoAs present a peak in absorbance due to the ordered arrangement so that they can be considered as a photonic crystal. The band structure of these photonic crystals determines thus the interaction with the incident radiation. The red line in figure 3.11a is the normal absorbance of SiO_2 NDoA immersed in ethanol: we see a suppression of the peak due to the reduced difference between the refractive indices of the medium (EtOH, $n_{EtOH} = 1.36$) and nanostructure array (SiO_2, $n_{SiO_2} = 1.45$) in comparison with the sample in air [114, 115].

Moreover, angle-dependent measurements are performed and reported in figure 3.11b, c and d. Figure 3.11b shows an extinction map in TE mode, while figure 3.11c in TM mode. By comparing these two maps, as for the Au NDoAs, TE mode does not present strong Rayleigh anomalies, whereas in TM mode the anomalies are visible as blue line that represent a minimum in the spectra. The other features visible in the maps are due to the interactions with the photonic band structures, and their dispersion follows the Rayleigh anomalies, confirming the interaction with the periodicity of the system.

Figure 3.11d shows the map made in TM mode with the sample in ethanol: as noted before the interaction is weaker and the features in the map are much less visible with respect to the samples in. However the weak features visible can be associated to the Rayleigh anomalies.

Therefore, by angular-dependent measurement we see how the geometrical behaviour, related to the Rayleigh anomalies, can be compared in both Au and SiO_2 NDoAs, by showing the possibility to use SiO_2 NDoAs to discern lattice and plasmonic contribution in the lasing processes, as it will be discussed in the following.

3.6 Ag NanoDisk Array

The other class of nanoarrays investigated is the nanodisk array, which sustaains localized SPR resonances since the metallic disks are well separated. The disks are arranged in a hexagonal lattice, whose constant lattice is of $340\,nm$ given by the initial diameter of the PS NSs used during the synthesis process, which is explained in the section 2.5. Figure 3.12 shows some SEM images at different magnitude of Ag NDiAs in top view. From these measurements we can obtain the mean diameter of the disks, by ImageJ software, as well as checking the order of the structures. The mean diameter varies between $150\,and\,200\,nm$ depending on the RIE treatment.

Figure 3.13a shows an example of an AFM image of Ag NDiA and a profile scan from
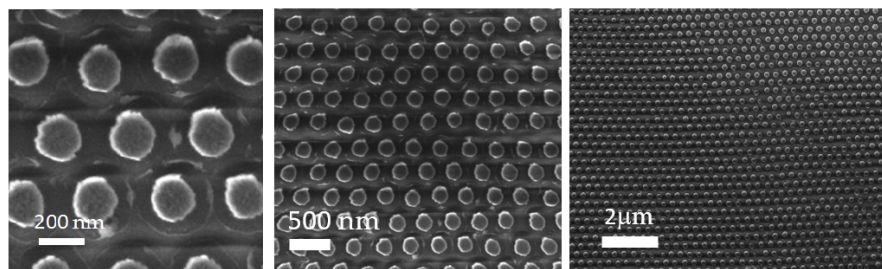
Figure 3.12: Ag NDiA: SEM images at different magnitudes.
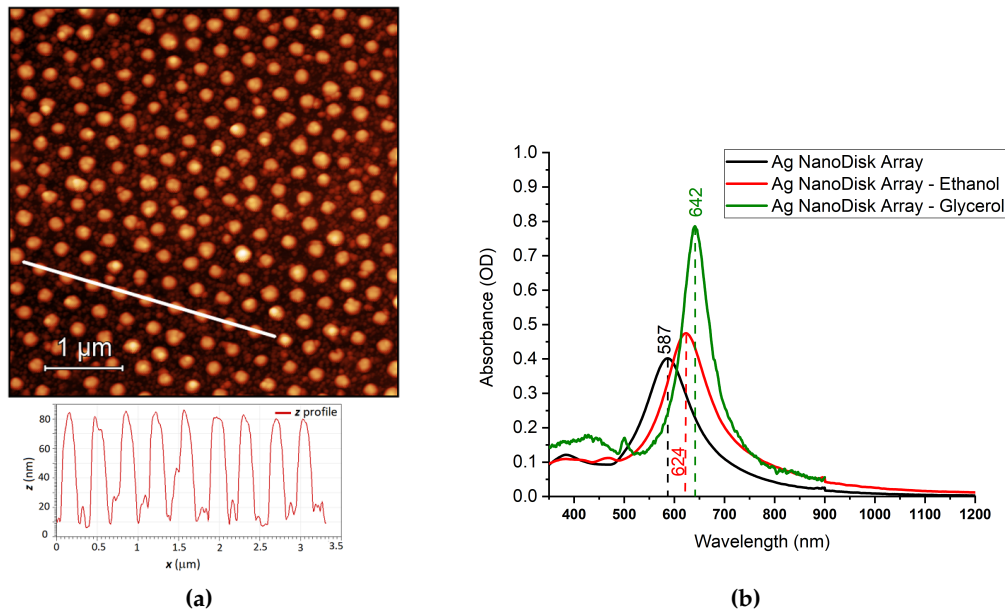
Figure 3.13: Ag NDiA: **(a)** example of AFM measurement, with inset a profile extrapolate from the map above along the white line. (b) Absorbance spectra in air (black curve), ethanol (red curve) and glycerol (green curve).

the map along the white. The mean height of this kind of samples is of about $74\,\mathrm{nm}$.

Absorbance spectra shown in figure 3.13bnare related to Ag NDiA in air (black curve), in ethanol (red curve) and in glycerol ($n_{gly} \sim 1.47$, green curve). The peak, that occurs at $587\,\mathrm{nm}$ in air, $624\,\mathrm{nm}$ in ethanol and $642\,\mathrm{nm}$ in glycerol, can be associated to the LSPR of the nanodisks. No evident interaction with the lattice is present at normal incidence, probably due to the large spectral separation of the two modes. Anyway, the dispersion of the lattice mode can lead to spectrally cross the plasmonic mode generating a spectral range of interaction between photonic and plasmonic modes creating hybrid modes.

Figure 3.14 presents the results of angle-dependent measurements, showing absorbance maps of Ag NDiAs. Similarly to the Au NDoAs, the map in figure 3.14a performed in TE mode exhibits weaker interaction with the lattice, compared with TM mode in figure 3.14b and 3.14c. The two maps in TM mode differ by the symmetry direction where lattice is oriented: in particular figure 3.14b shows a measurement with the sample oriented in the symmetry direction ΓK, while 3.14c in ΓM. As for Au NDoAs ΓM direction shows a sharper and more intense response compared to ΓK.

However, the most interesting result is obtained when Ag NDiA is immersed in a medium, in this case glycerol. The absorbance map with the sample in glycerol in TM mode and oriented in ΓM direction is showed in figure 3.14d. Moreover, figure 3.14e shows the absorbance map in the two different directions ΓK and ΓM, by plotting the energy of the diffracted radiation as a function of the parallel component of the incident wavevector $k_{//i}$, with Rayleigh anomalies superimposed and labeled by their Miller indices.

In ΓM direction around $30°$ an interaction between photonic and plasmonic modes arises showing an anticrossing phenomenon of the two modes. *Anticrossing* or *avoided crossing* is a quantum phenomenon that arises when two eigenvlues of the system, in our case for the state associated to the photonic lattice mode and the plasmonic resonance, assume the

(a) Absorbance TE ΓK

(b) Absorbance TM ΓK

(c) Absorbance TM ΓM

(d) Absorbance TM ΓM in glycerol

(e) Absorbance TM in glycerol
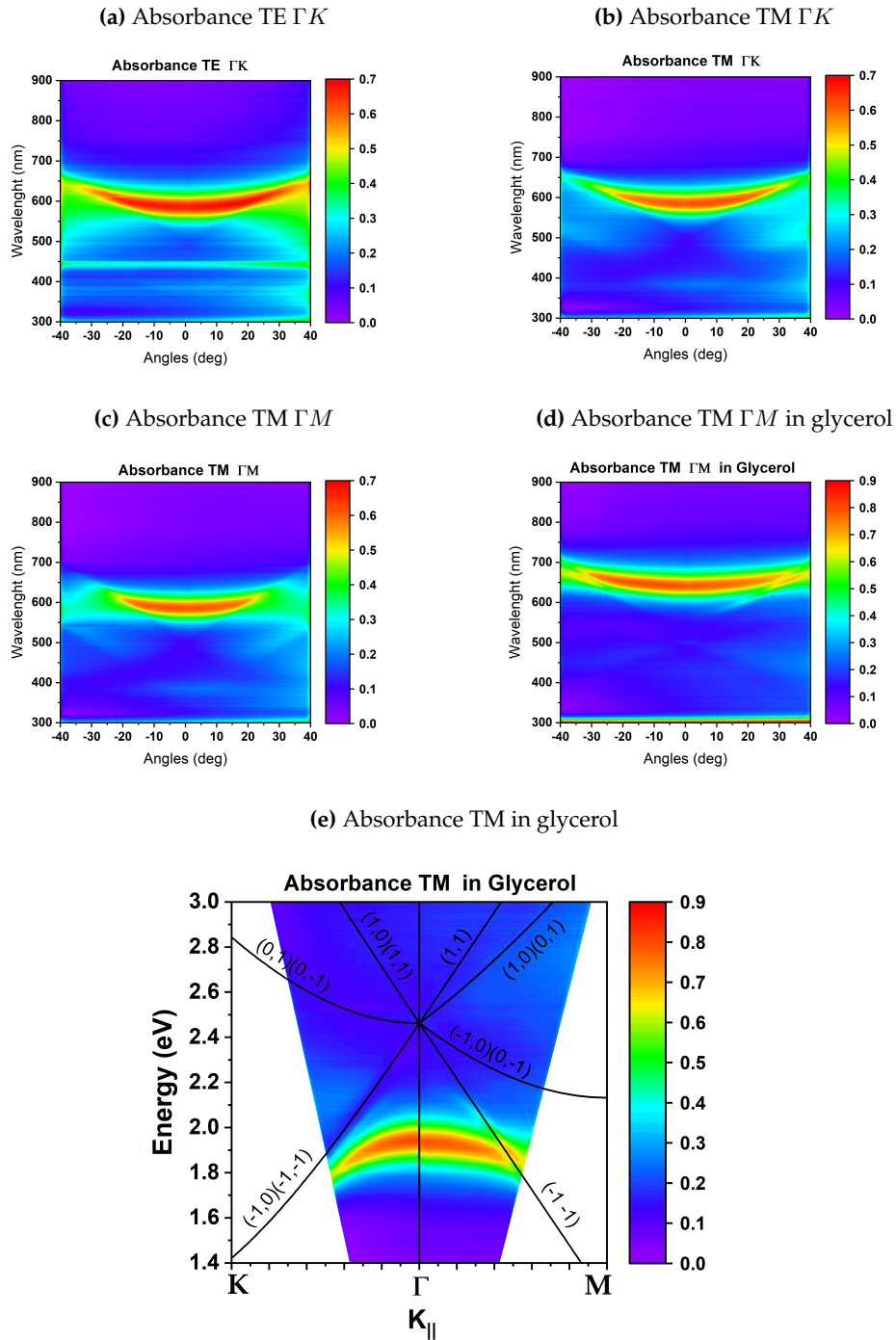
Figure 3.14: Absorbance maps of Ag NDiAs as a function of incident angle: **(a)** is performed in TE mode with the sample oriented in ΓK direction; **(b)** TM mode in ΓK symmetry direction; **(c)** TM mode in ΓM orientation;**(d)** TM mode in ΓM direction with sample immersed in glycerol. **(e)** Absorbance map in TM mode with sample in glycerol, both $K\Gamma$ and ΓM direction are represented in diffracted photon energy as a function of parallel component of incident wave vector $k_{//i}$. Rayleigh anomalies are superimposed and labeled with the respective Miller indices.

same value [116]. This means a strong interaction between the modes with the resulting formation of hybrid modes, such as SLRs.

3.6.1 FEM simulations

As for Au nanodome array, in order to complete the characterization of the samples, numerical calculations are used to study the local electric field distribution near to nanoparticles. We performed
this simulation with COMSOL Multiphysics® software.

The geometric parameters of these simulations are reported in figure 3.15. In figure 3.15a the 3D model is shown: a cell formed by a hexagonal prism is modelled with periodic boundary condition on the lateral face and PMLs on the top and the bottom in order to simulate the two-dimensional hexagonal lattice, as the previous model used for the Au nanodome array. Figure 3.15b shows the parameters of the model: in particular, the distance between two opposite lateral faces, that define the periodicity, is equal to the lattice constant $a = 340\,\text{nm}$. Ag nanodisk is modelled as a cylinder with diameter of $150\,\text{nm}$ and height of $70\,\text{nm}$ where the edges are rounded with a curvature radius of $5\,\text{nm}$ in order to avoid unphysical numerical hot spots during the calculation.
Furthermore, the substrate is modeled with $350\,\text{nm}$ thick SiO_2 substrate, i.e., a non absorptive material with refractive index of $n_{sub} = 1.45$. Similarly, the medium is modeled as a non dissipative material with $450\,\text{nm}$ thickness and a refractive index of $n_{med} = 1.47$ (to be compared to the glycerol case).

The FEM simulation in FDFD is then performed from 400 to $900\,\text{nm}$ wavelength. For normal incidence we uesed $\mathbf{k} = (0, 0, k)$ with the incident EM plane wave electric field $\mathbf{E}_i = (E_0, 0, 0)$, where $E_0 = 1\,\text{V/m}$, and frequency $\nu = c/\lambda$.

Figure 3.16a shows the simulated absorbance spectrum, while figure 3.16b reports the experimental absorbance spectrum of Ag NDiA in glycerol, as a comparison with the simulated spectrum. In this one, two peaks can be identified, one at $\lambda = 505\,\text{nm}$

(a)   (b)
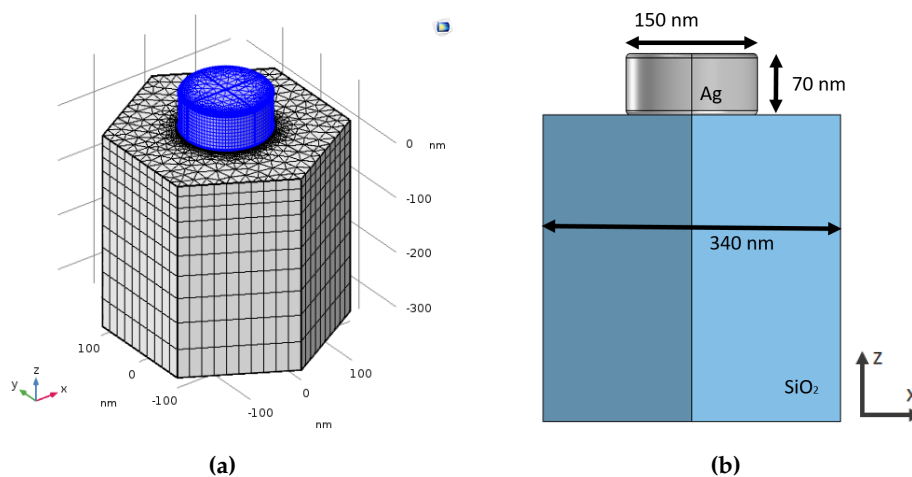
Figure 3.15: (a) 3D view model used for Ag nanodisk array simulations: the disk is highlighted in blue and the used mesh is shown. **(b)** Main geometric parameters used in the simulation (the sketch shows the $\hat{x}z$ plane at $y = 0$

).

(a) Simulation   **(b)** Experiment
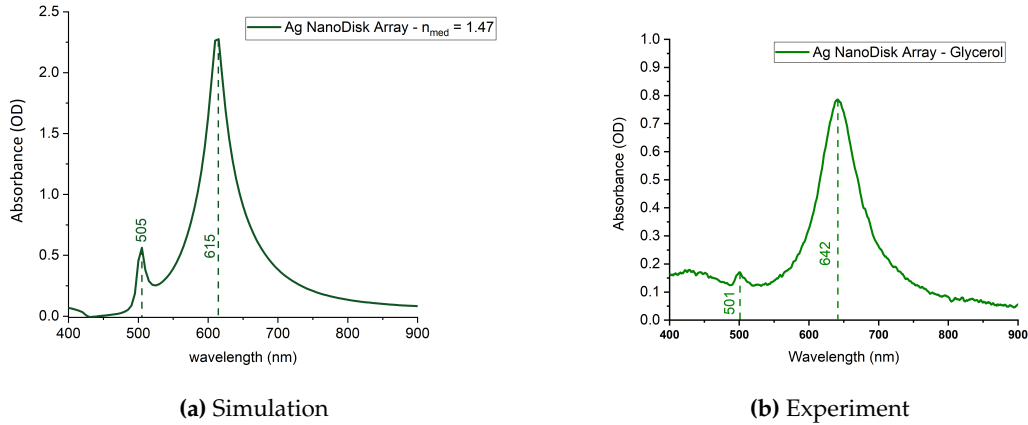
Figure 3.16: FEM simulated Absorbance under normal incidence (**a**) and experimental one (**b**) are compared for simulation result of Ag NDiA.

and the other at $\lambda = 615$ nm. These peaks can be associated to the experimental peaks which occur at at $\lambda = 501$ nm and $\lambda = 642$ nm. The first one is well matched and is due to geometrical arrangement. On the other hand, the second one in the experimental spectrum is redshifted. This peak can be associated to the LSPR and the difference can be due to the non perfect cylindrical shape of real nanodisks, while the differences on the bandwidth and the absorbance intensity are due to the lattice defects or non identical size and/or shape of disks.

From FEM results we can also evaluate the local electric field distribution on the two resonances. Figure 3.17 shows the electric field distribution in the planes $\hat{x}\hat{z}$ at $y = 0$ and $\hat{x}\hat{y}$ at $z = 0$. In particular, the field enhancement $|\mathbf{E}|/E_0$ and the component $\hat{z}$ of the electric field E_z/E_0, perpendicular to the lattice plane, are plotted.

Figures 3.17a (plane $\hat{x}\hat{z}$) and 3.17c ($\hat{x}\hat{y}$) show the field enhancement at $\lambda = 505$ nm, whereas figures 3.17b ($\hat{x}\hat{z}$) and 3.17d ($\hat{x}\hat{y}$) show E_z at the same wavelength.
In the same configuration figures 3.17e, f, g and h show the field enhancement and E_z respectively, at $\lambda = 615$ nm.

By looking at the field distribution is possible to understand the nature of the two investigated resonances. The field at $\lambda = 615$ nm is more confined than the one at $\lambda = 505$ nm and given the field distribution, we can associate this resonance to a dipolar LSPR. Furthermore we note a high field enhancement (up to 16 times E_0) in the proximity of the bottom edge of the disk.
On the other hand, the field at $\lambda = 505$ nm is less confined and more intense: this is a confirmation of the extended nature of the resonance and therefore it can be associated to the SLR of the system.

(a) Side view ($\hat{x}z$, $y = 0$) of near field enhancement $|\mathbf{E}|/E_0$ at $\lambda = 505\,\mathrm{nm}$
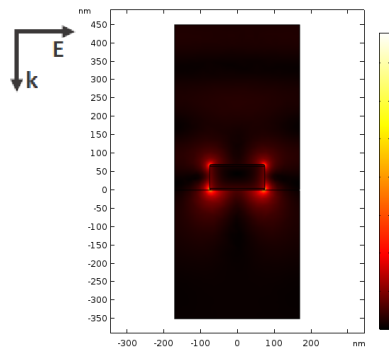
(b) Side view ($\hat{x}z$, $y = 0$) of E_z/E_0 at $\lambda = 505\,\mathrm{nm}$
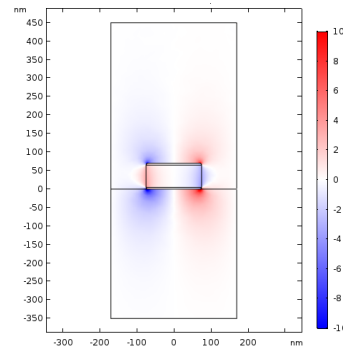
(c) Top view ($\hat{x}y$, $z = 80\,\mathrm{nm}$) of near field enhancement $|\mathbf{E}|/E_0$ at $\lambda = 505\,\mathrm{nm}$
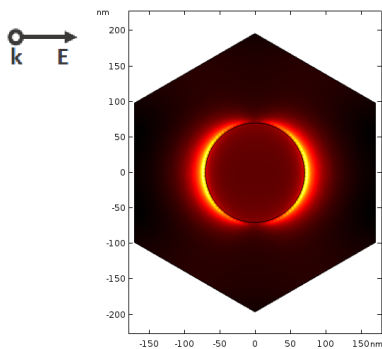
(d) Top view ($\hat{x}y$, $z = 80\,\mathrm{nm}$) of E_z/E_0 at $\lambda = 505\,\mathrm{nm}$
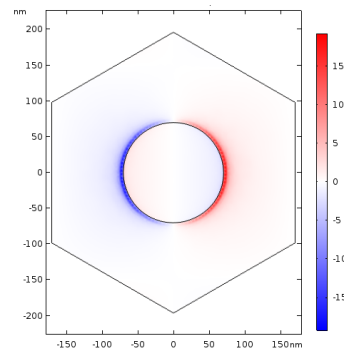
(e) Side view ($\hat{x}z$, $y = 0$) of near field enhancement $|\mathbf{E}|/E_0$ at $\lambda = 615\,\mathrm{nm}$
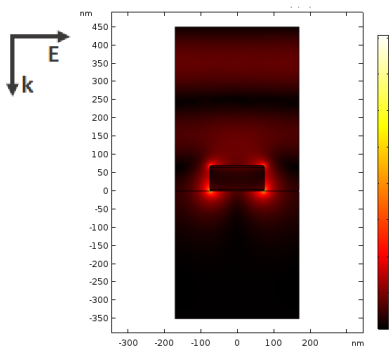
(f) Side view ($\hat{x}z$, $y = 0$) of E_z/E_0 at $\lambda = 615\,\mathrm{nm}$
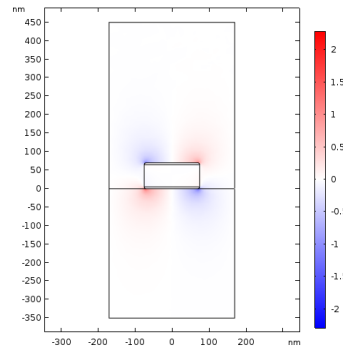
(g) Top view ($\hat{x}y$, $z = 80\,\mathrm{nm}$) of near field enhancement $|\mathbf{E}|/E_0$ at $\lambda = 615\,\mathrm{nm}$
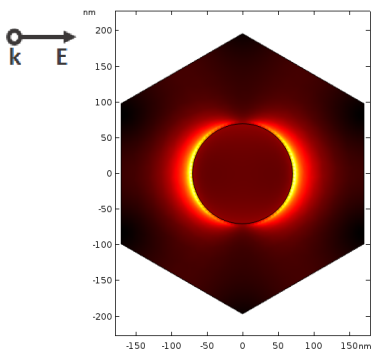
(h) Top view ($\hat{x}y$, $z = 80\,\mathrm{nm}$) of E_z/E_0 at $\lambda = 615\,\mathrm{nm}$
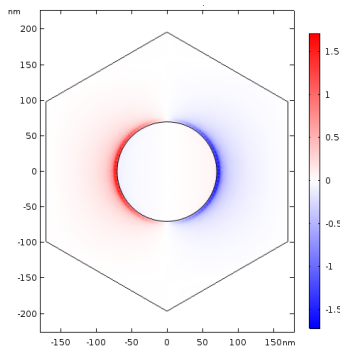
Figure 3.17: Simulation of electric near-field distribution of an Ag nanodisk array.

Chapter 4

Lasing Emission Properties

In this chapter we will present the results about the emission properties of our devices, demonstrating the possibility to reach lasing emission from the coupling between dye molecules and plasmonic nanostructure arrays made by NSL. In particular, we will describe the setups with which photoluminescence (PL) measurement are taken, and we will show and discuss the main properties of the emitted beam, spectral bandwidth, threshold, directionality and angular divergence. Furthermore, we will report and discuss the results on the temporal coherence of the emission obtained by the modified Michelson interferometer set up during this project. From these results we will discuss the possible future development of these plasmonic nanolaser devices, supported by numerical simulations and first experimental results.

4.1 Photoluminescence Spectroscopy

The photoluminescence (PL) spectroscopy technique investigates the emission of light from a material after the absorption of photons. In our system, shown in figure 4.1a, the second harmonic (at $\lambda = 532\,\mathrm{nm}$) of a *Q-switched Nd:YAG* laser (Blilliant by Quantel) is used as optical pump. The laser emits pulses of $4.5\,\mathrm{ns}$ at a repetition rate (RR) of $10\,\mathrm{Hz}$. The laser beam is attenuated by optical density (OD) filters (by Thorlabs), which are placed in two wheels and can be interchanged and combined in order to modulate the beam's energy. After the filter wheels, the laser beam is driven toward the sample by two highly reflective mirrors for this specific wavelength (intensity loss $< 2\,\%$). Along its path, the beam passes through a pinhole with a diameter of $3\,\mathrm{mm}$, which defines the beam dimension with an area of $7.1\,\mathrm{mm}^2$.

For the collection part of our system, we set up an apparatus for angle-dependent measurements, shown in figure 4.1b. As for angle-dependent transmittance measurements, the sample is placed in the middle of a manual goniometer in order to control the lattice orientation. This goniometer is vertically placed (figure 4.1b) at the center of a motorized rotating stage but, unlike previous measurements, the sample holder is disconnected from this. A micrometer under the manual goniometer allows us to finely control the position of the sample on the pivot of the motorized rotating system.

On the motorized rotating frame it is attached a guide which houses the collection set-up. This one is composed by a $5\times$ objective that focuses the collected radiation on the entrance lens of an optical fiber, or alternatively by a coupling lens which focuses the emitted light into the fiber. Moreover, a longpass filter $\lambda > 550\,\mathrm{nm}$ is placed in front of
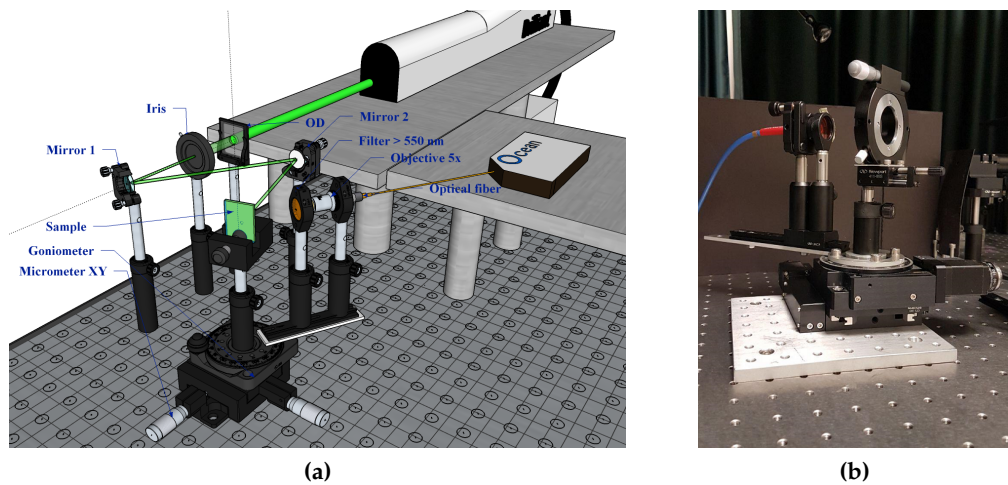
Figure 4.1: (a) Schematic description of the optical setup used for emission characterization. **(b)** Photo of collection setup.

the collection lens in order to prevent possible reflections of the pump laser from entering the detector. This collection system can be moved along the guide, allowing us to find a good balance between collected intensity and angular resolution. The system with the objective is placed at a distance of $\sim 11\,\mathrm{cm}$ from the sample surface that corresponds to an angular aperture of about $6°$ (NA $\simeq 0.05$), while for the other system the lens is placed at about the same distance but the angular aperture is about $3°$ (NA $\simeq 0.03$).

Then the fiber carries the signal to the detector OceanOptics HR-4000, which records and transfers data to a computer and by the software *SpectraSuite* we can visualize and save the spectra. By analysing the data, we can extrapolate the principal properties of the emitted beam: wavelength, spectral bandwidth, threshold, directionality and angular divergence. These will be reported in the following sections for the plasmonic nanostructures taken into account.

4.2 Dye Emission Properties

In the present work laser dyes are used as gain media. As previously described in section 2.7, Pyridine 2 and Styryl 9M have been chosen for their high efficiency and emission in the visible and near-IR spectral region. In figure 4.2, we report the normalized absorption and emission spectra of the Pyridine 2 (fig. 4.2a) and Styryl 9M (fig 4.2b) dissolved in ethanol. Pyridine 2 presents an absorption peak at $505\,\mathrm{nm}$, while an emission peak in ethanol at $694\,\mathrm{nm}$. Styryl 9M has an absorption peak at $583\,\mathrm{nm}$, and an emission peak in ethanol at $808\,\mathrm{nm}$. In the spectra, the wavelength of the second harmonic of the Nd:YAG pump laser ($\lambda = 532\,\mathrm{nm}$) is highlight in green. We show here also the angular maps, previously reported in chapter 3, of an Au NDoA (fig. 4.2c) and an Ag NDiA (fig. 4.2d). Here the emission bands of the dyes are superimposed in order to check the match between the dye emission and the plasmonic modes. The plotted bands indicate the FWHM of the dyes' emission spectra converted in energy.

A solid state system has been also investigated and characterized. This consists in a dye-doped polymer thin film, containing Styryl 9M molecules. The synthesis process is explained in section 2.7. The absorption and emission spectra are reported in figure 4.2e.

While the absorption spectrum is unchanged, the emission spectrum is blueshifted at 740 nm. This shift is of about 0.15 eV, comparable with the energy of vibrational states of the molecules, suggesting the inhibition of some vibrational and rotating states by the embedding in the polymeric matrix.

(a) Pyridine 2

(b) Styryl 9M

(c) Au nanodome array

(d) Ag nanodisk array

(e) Styryl 9M in PMMA
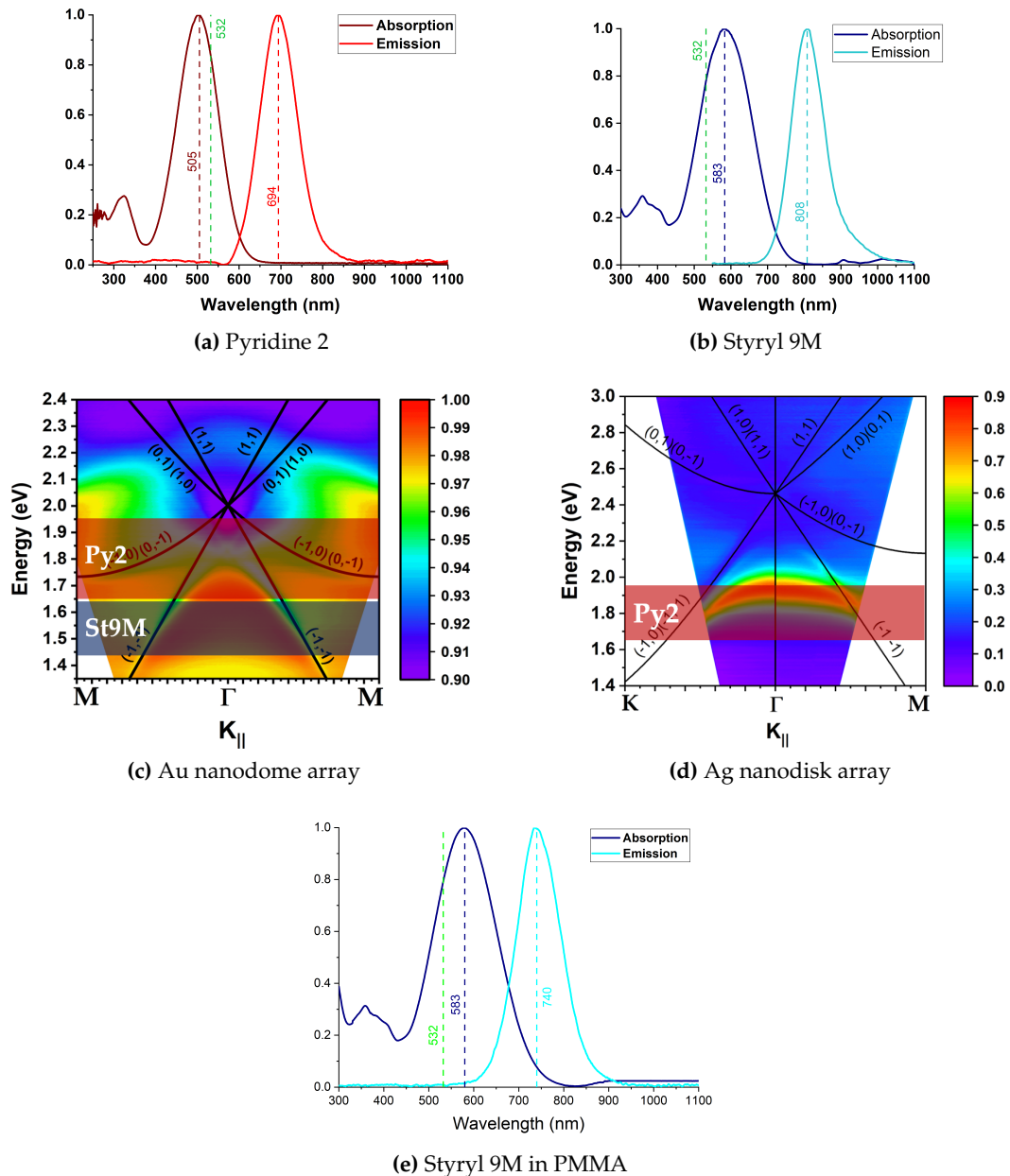
Figure 4.2: (a) Normalized absorption and emission of Pyridine 2. **(b)** Normalized absorption and emission of Styryl 9M. **(c)** Extinction map of an Au nanodome array with dyes' emission superimposed. **(d)** Absorbance map of an Ag nanodisks array with Pyridine 2 emission superimposed. **(e)** Normalized absorption and emission of Styryl 9M embedded in a PMMA film.

Photobleaching

As we discussed in section 2.7, a phenomenon which we have to pay attention to is the photobleaching. In this process the dye molecules bleach as a consequence of a photoreaction with the surrounding environment, leading to a decreasing of the quantum yield and, consequently, of the fluorescence emission of the dye molecules [102].

For the dyes in a liquid solution, a high photochemical stability is demonstrated in the literature [117], up to tens of mJ/cm^2, i.e. well above of our working condition $\sim$ 1 mJ/cm^2. However, this phenomenon can become important when the dye molecules are embedded in a solid matrix.

For this reason, we performed long time exposure measurements on a typical Styryl 9M doped PMMA film used in our system, with a concentration of about 1 mM. In figure 4.3 we report the fluorescence peak intensity as a function of the exposure time t for different pumping fluences. In particular, in **(a)** for a fluence of about 1 mJ/cm^2, the intensity can be linearly fitted and its variation after some hours is less than 10 %. Increasing the fluence to about 4 mJ/cm^2, shown in **(b)**, the data follow an exponential decreasing, with a characteristic time of 40 ± 3 minutes. Jumping to an higher fluence of about 20 mJ/cm^2, **(c)**, the fluorescence intensity can be fitted by a double exponential

$$y = A_1 e^{-x/t_1} + A_2 e^{-x/t_2} + y_0 \tag{4.1}$$

where $t_1 = 1.9 \pm 0.2$ minutes and $t_2 = 16 \pm 2$ minutes are the characteristic times of

(a) $1\,\text{mJ/cm}^2$
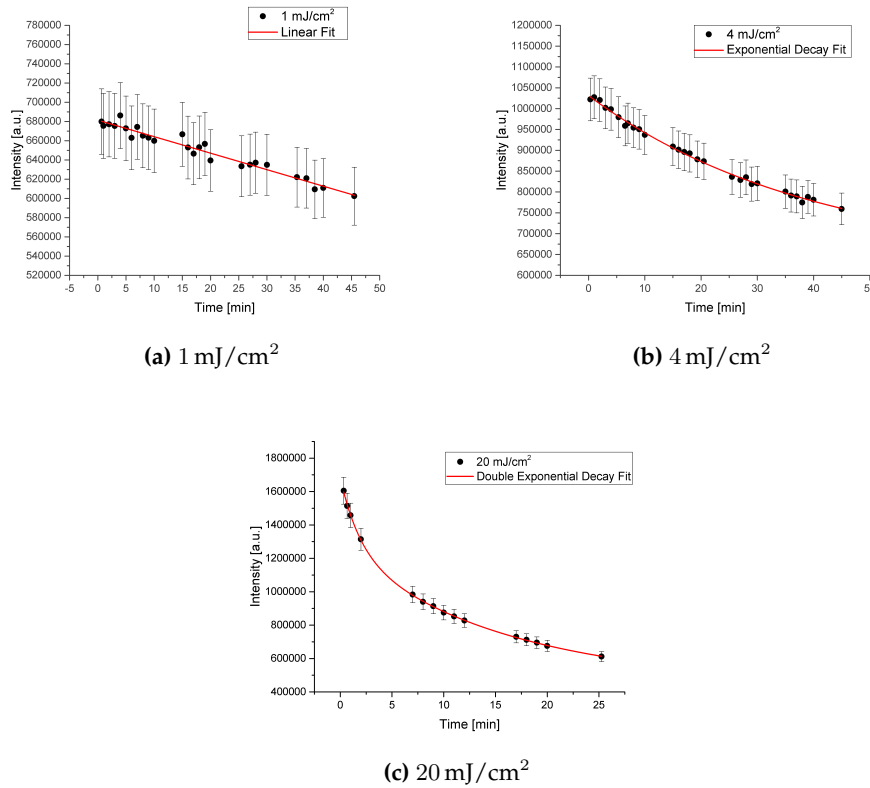
(b) $4\,\text{mJ/cm}^2$

(c) $20\,\text{mJ/cm}^2$

Figure 4.3: Photobleaching measurements at different pumping fluences: $1\,\text{mJ/cm}^2$ in **(a)**, $4\,\text{mJ/cm}^2$ in **(b)** and $20\,\text{mJ/cm}^2$ in **(c)**. The black points represent the fluorescence peak intensity at the time t of exposure, while the red curve is the best fit of the experimental points.

each contribution. This trend in the photobleaching process is common and is due to the different arrangements of the dye molecules, which interact differently with the environment [117].

The photobleaching process thus places a limit of operation for the samples at a certain fluence condition. However, the working range of our samples is around $1\,\mathrm{mJ/cm^2}$, so we expect that bleaching does not play a significant role.

4.3 Lasing Emission Results

The emission properties of the gain media coupled to the synthesized nanoarrays have been characterized with different methods to obtain information about wavelength, bandwidth, threshold, directionality and angular divergence of the emission. In particular, we coupled Au nanodome arrays with Pyridine 2 dissolved in ethanol (Au NDoA-Py2) and PMMA films embedded Styryl 9M (Au NDoA-St9M). Ag nanodisk arrays has been coupled with Pyridine 2 dissolved in ethanol (Ag NDiA-Py2). The concentration of Pyridine 2 in ethanol is of about $1\,\mathrm{mM}$, as well for the Styryl 9M embedded in the PMMA film. These results will be presented in the following paragraphs.

4.3.1 Nanodome Array - Liquid Gain Medium

The first sample we are going to discuss is the Au nanodome array (Au NDoA), which parameters are reported in table 3.1. From the optical properties of the Au NDoAs, we have chosen to couple these nanoarrays with Pyridine 2 dissolved in ethanol (Au NDoA-Py2). This device is characterised by the PL measurements (sec. 4.1) and shows an amplified emission, which arises at 720 nm as we can see in figure 4.4a at a pump fluence of $1.4\,\mathrm{mJ/cm^2}$. On the other hand, this phenomenon occurs neither in SiO_2 nanodome arrays nor in the presence of the dye only. This means that our system works and that the dye emission is modified by the presence of the plasmonic lattice below. The ability to emit laser light lasts for a long time, thanks to its low emission threshold which allows the system to work at low fluences, minimizing the photobleaching effect.
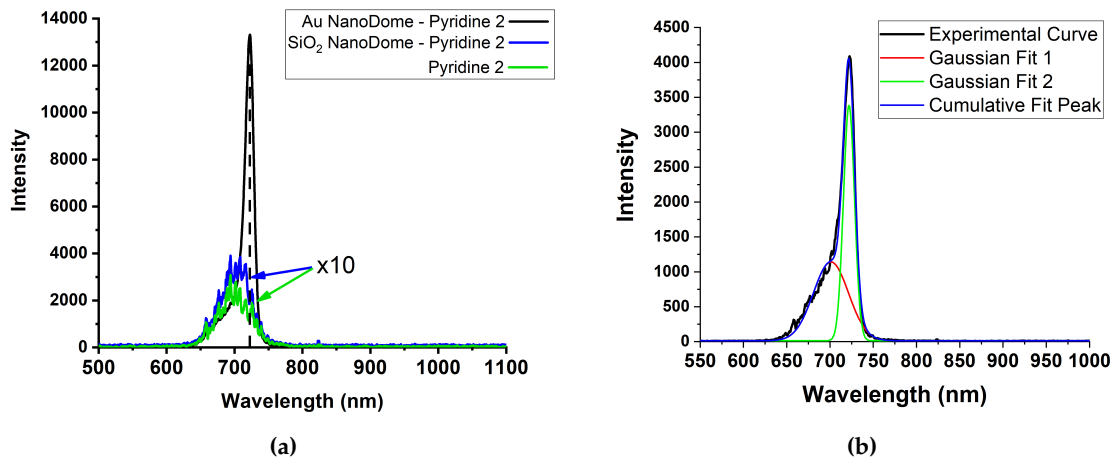
Figure 4.4: Comparison of the Pyridine 2 emission coupled with an Au nanodome array, a SiO_2 nanodome array and a flat silica slab. The samples are pumped at $50°$ with a fluence of about $1.4\,\mathrm{mJ/cm^2}$ and the emission is collected at $17°$.

In figure 4.4b an emission spectrum of the Au NDoA-Py2 at a pump fluence of $1.4\,\mathrm{mJ/cm^2}$ is reported. How we can see the spectrum is formed by two component, the amplified emission and the fluorescence band. These two components are deconvoluted by a multipeak fit, as shown in figure 4.4b, where the linear convolution of two Gaussian peaks is used.

Threshold

One of the main characteristics of a laser emission is the threshold behaviour. For excitation at fluence above the threshold a narrow emission feature distinctive of stimulated emission grows very quickly, faster than spontaneous emission, as a function of pump fluence.

Au NDoA-Py2 is pumped with a different fluences in order to verify the threshold behaviour of the sample emission. As shown in figure 4.5a and 4.5b (in a 3D representation for a clearer view of the individual curves), a narrow peak at $720\,\mathrm{nm}$ arises from the flu-
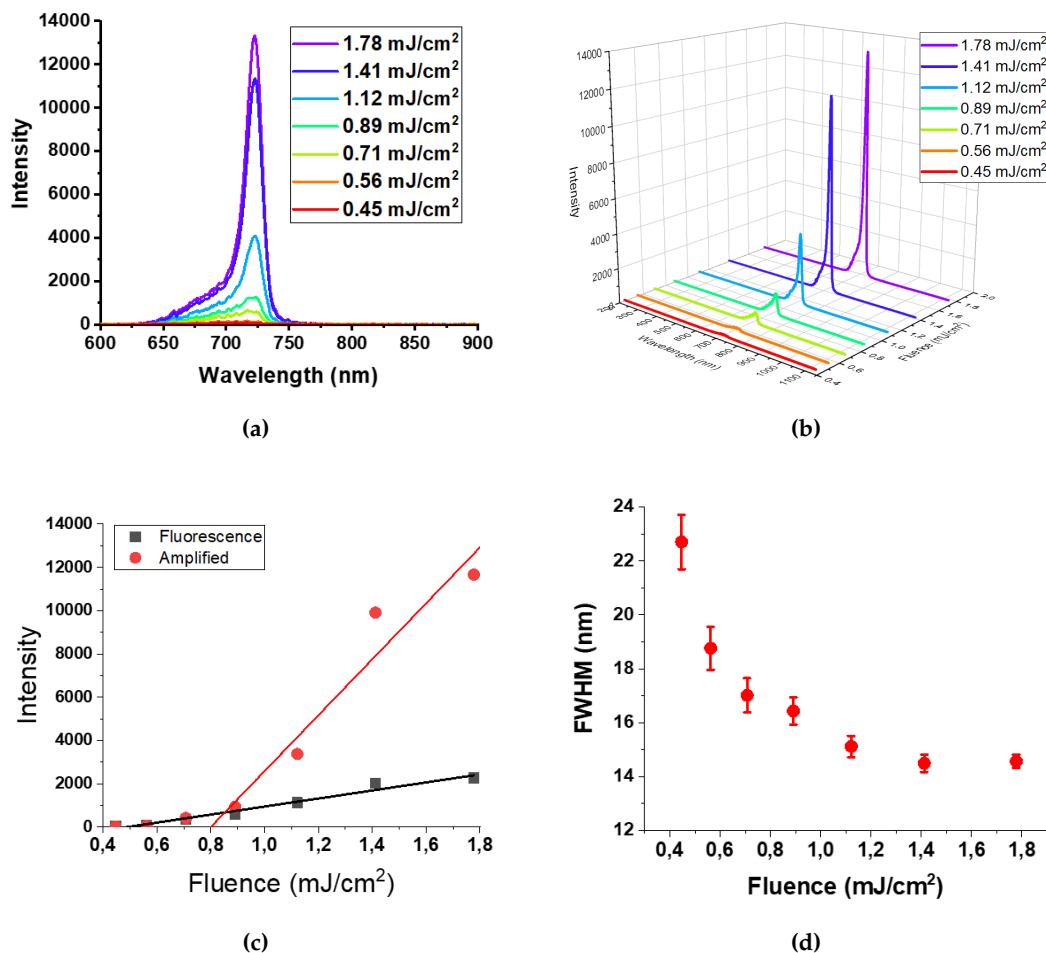
Figure 4.5: Emission spectra of Au NDoA-Py2 device are plotted at different pump fluences in **(a)** and in **(b)** with a 3D view. **(c)** Intensity of fluorescence (black points) and amplified emission (red points) as a function of pump fluence. The two lines are linear fits of the data. **(d)** Bandwidth of the amplified emission peak as a function of pump fluence.

orescence band. This emission is redshifted with respect to the fluorescence peak, which occurs at about $695\,$nm, because, unlike fluorescence that depends on only the molecule structure, lasing emission is the result of the combination between a cavity mode and a specific optical transition in the molecular energy level structure.

By deconvolution of the two contributions intensity peaks of fluorescence and amplified emission can be plotted as a function of excitation fluence, as shown in figure 4.5c. The Fluorescence peak grows linearly with the fluence, while amplified emission presents two distinct trends, which define a threshold behaviour. These two regimes are correlated, one to compensation population inversion where spontaneous emission prevails and the other when the saturation of population inversion is reached and stimulated emission prevails [43]. By fitting these two regions with linear fits the crossing point between the lines is obtained. This represent the threshold point of the laser emission, which occurs at $0.9 \pm 0.1\,$mJ/cm^2, comparable with threshold values in the literature for the similar devices [19, 27, 34].

The FWHM of the Gaussian fits is also plotted as a function of pump fluence, is shown in figure 4.5d. The graph shows a decreasing of FWHM of amplified emission, from $\sim$ $23\,$nm to $14\,$nm, which confirms the arising of a stimulated process. For the fluorescence one the value stills around $70\,$nm.

Furthermore, an important phenomenon that has to be taken into account is: the *Amplified Spontaneous Emission* (ASE). ASE is the amplification of the spontaneous emission by the stimulated emission process, i.e. a photon emitted by spontaneous emission, before leaving the gain material, triggers stimulated emission of excited molecules generating amplification [118, 119]. ASE presents many common features with laser emission, such as the threshold behaviour. However, unlike laser emission, which needs a feedback for oscillation, ASE arises without the feedback process and this gives rise to an important difference on the temporal coherence of the signal. In fact, even if ASE can present high spatial coherence, it has not temporal coherence given by the feedback process and presents a broad emission.
Therefore, in order to discern lasing emission form ASE, coherence measurements have been performed. The results will be presented in section 4.4.

The comparison between the emission spectra as a funcion of the pump fluence of a Au NDoA-Py2, SiO$_2$ NDoA-Py2 and Pyridine 2 only is presented in figure 4.6. Fixing the intensity range for all the samples, we notice a significant difference in the maximum
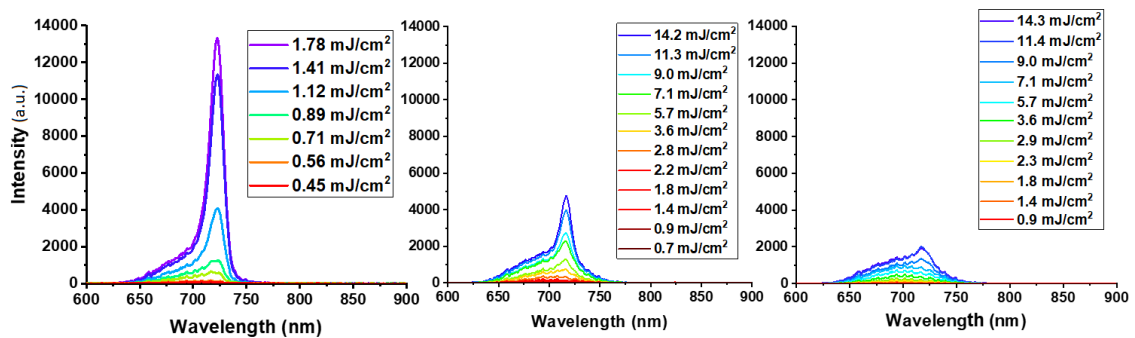
Figure 4.6: Comparison of the Pyridine 2 emission coupled with an Au nanodome array, a SiO$_2$ nanodome array and a flat silica slab at different pump fluences. The samples are illuminated at $50°$ and the emission is collected at $17°$.
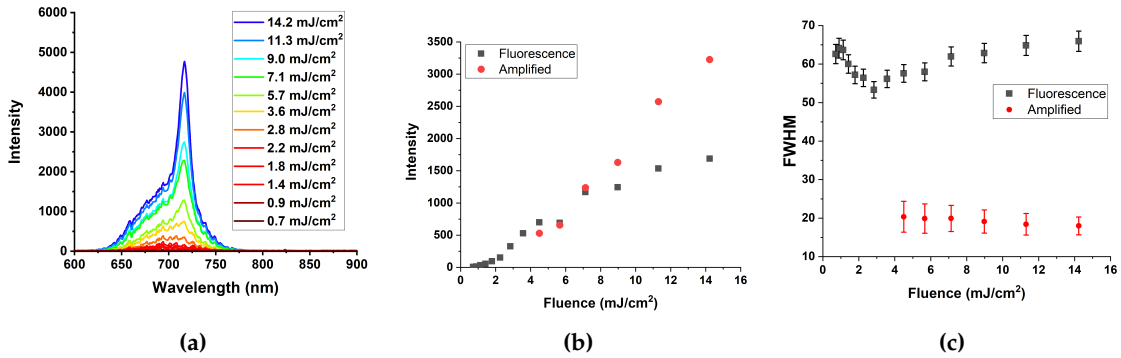
Figure 4.7: SiO$_2$ NDoA-Py2: **(a)** emission spectra as a function of pump fluence. **(b)** Intensity of fluorescence (black points) and amplified emission peaks (red points) as a function of pump fluence. **(c)** Bandwidth behaviour as a function of pump fluence.

emission. It is important to say that, even if we use a ten-times higher fluence, we do not obtain comparable values with Au nanodome arrays. In fact, in SiO$_2$ nanodome arrays and the dye solution, the maximum emission is significantly lower, meaning that stimulated emission does not occur.

However, some narrower features arise from the fluorescence band in the SiO$_2$ NDoA-Py2 and dye emission spectra, as we can see in more details in figure 4.7a for SiO$_2$ NDoA-Py2 and 4.8a for Pyridine 2. For the SiO$_2$ NDoA-Py2 this narrow emission occurs at fluences bigger than $\sim 5\,\mathrm{mJ/cm}^2$ as shown in figure 4.7b. This emission grows linearly without any characteristic threshold features, with a stable FWHM of about $20\,\mathrm{nm}$ (fig. 4.7c). Instead, for the sole Pyridine 2 a narrow peak arises above $\sim 9\,\mathrm{mJ/cm}^2$, as we can see in figure 4.8b, with a similar FWHM.

These results confirm a drastically different interaction between the dye and the Au nanostructured sample, which is due to the plasmonic properties of the nanoarray. This narrow peak, that arises at the same wavelength as for Au NDoA-Py2, is probably due to the amplified spontaneous emission of the dye which can exhibit at this fluence.
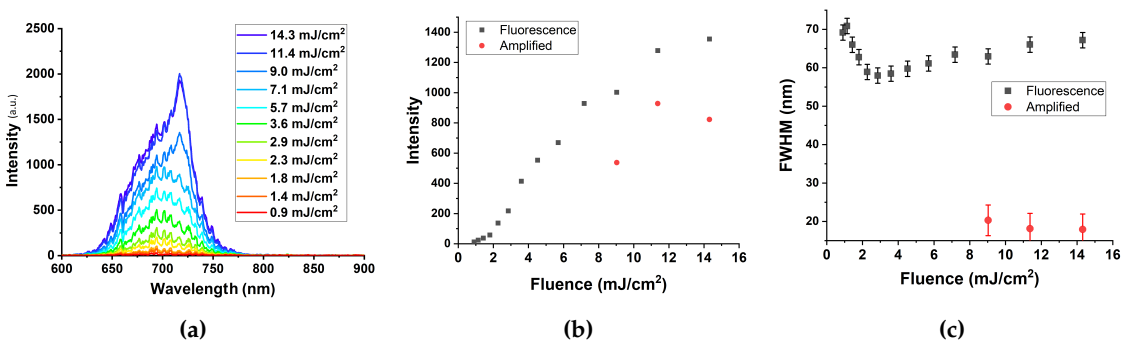
Figure 4.8: Pyridine 2 solution: **(a)** emission spectra as a function of pump fluence. **(b)** Intensity of fluorescence (black points) and amplified emission peaks (red points) as a function of pump fluence. **(c)** Bandwidth behaviour as a function of pump fluence.

Directionality

Amplified emission of Au NDoA-Py2 is strongly angle-dependent, i.e. the sample emits a beam with a specific direction and a small angular divergence. Directionality of laser emission is an important characteristic which distinguishes laser from other light sources and is also very useful for many applications. In a conventional laser, as discuss in section 1.1.4, directionality is a consequence of the selection of modes by the optical cavity where the gain medium is placed.

For two-dimensional plasmonic arrays, the directionality is given by the coupling with the lattice modes. Figure 4.9a represents the angular behaviour at $1.4\,\text{mJ/cm}^2$ pump fluence of the amplified emission of an Au NDoA-Py2: a high intensity emission at $17°$ and $720\,\text{nm}$ ($1.72\,\text{eV}$). By superimposing the Rayleigh anomaly mode (-1,-1), it is clear that lasing emission occurs when the plasmonic lattice mode (sec. 1.2.3) crosses the emission band of the dye. This confirms that the plasmonic lattice mode couples spectrally and spatially with the Pyridine 2 molecules, leading to an amplified emission.

Analysing the emission spectra taken at different angles, we can plot the angular behaviour of the amplified emission, the result is reported in fig. 4.9b: a Gaussian curve can be used to fit the data. The FWHM of this curve identifies the angular divergence of the emitted beam and result $3.0° \pm 0.3°$. The peak occurs at to the emission angle of $16.9° \pm 0.1°$.

The angular emission behaviour of SiO_2 NDoA-Py2 is reported in figure 4.10a, measured at higher fluence $14.3\,\text{mJ/cm}^2$. This value is almost ten times the fluence used for the Au NDoA-Py2. This sample shows again an amplified emission at $17°$, resulting from the crossing of the Rayleigh anomaly (-1,-1) mode, figure 4.10a. This means that the lattice properties of the nanostructed array define the directional properties of the amplified emission.

Differently for the Pyridine solution (fig. 4.10b) the amplified radiation does not exhibit any angular dependence.

(a)

(b)
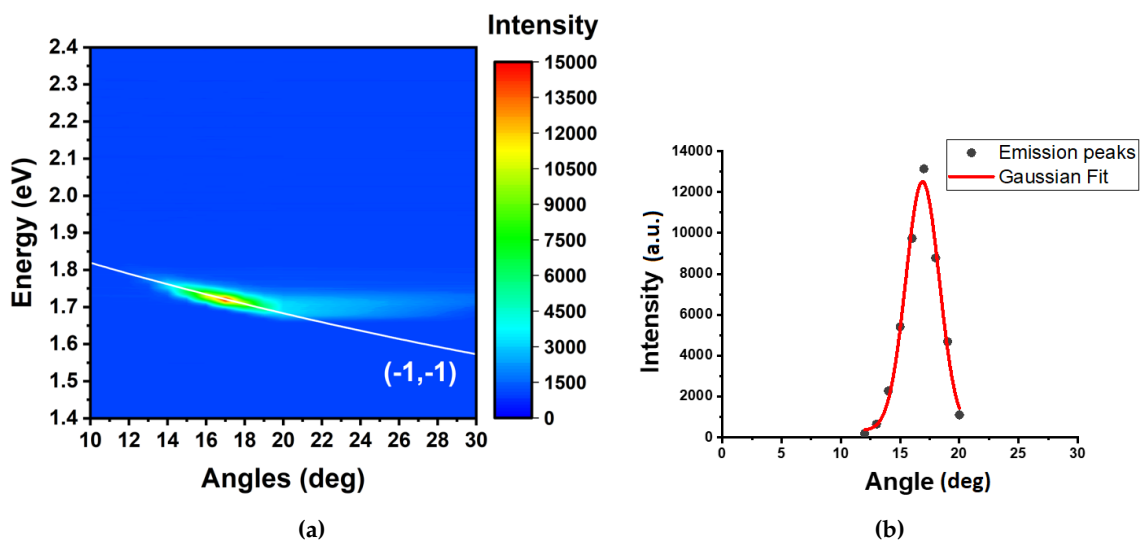
Figure 4.9: (a) Emission map of a Au NDoA-Py2. The white line identifies the (-1,-1) Rayleigh mode. **(b)** Amplified emission intensity as a function of collection angle: the red curve represents the Gaussian fit of the data.
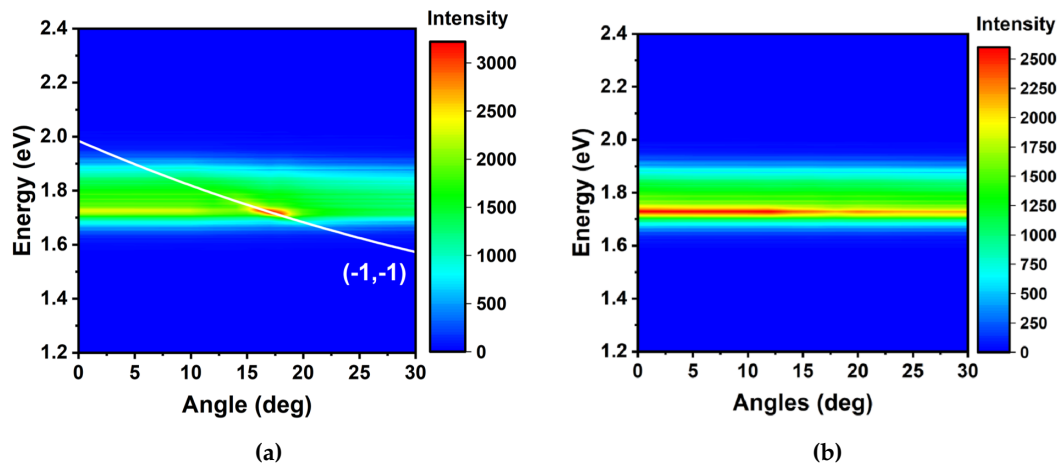
Figure 4.10: (a) Emission map of a SiO$_2$ NDoA-Py2: the white line identifies the (-1,-1) Rayleigh anomaly. **(b)** Emission map of Pyridine 2 only dissolved in ethanol.

Furthermore, since amplified emission occurs at $17°$, the sample is pumped with an angle of $50°$ due to the geometrical arrangement of the optical system. So we investigated the dependence of the emission as a function of the incidence angle of the excitation beam, in order to verify that the direction of the incident beam does not play a role on the lasing emission. This means that the pump configuration does not influence the lasing emission. Therefore we chose to excited the sample at $50°$ in order to have an enough wide range of angles to study the directional properties of the lasing emission. Moreover, as shown in figure 4.11, above $50°$ the intensity drastically decreases due principally to the dependence of the fluence on $\cos(\theta)$. The gap in the data is due to the condition of superimposition of the specular reflection of the pump beam and the collection setup.

Particularly, figure 4.11 shows the emission of an Au nanodome array coupled with Pyridine 2 in ethanol as a function of the incident angle of the exiting beam. These measurements have been taken with the same PL setup described above, with the collection setup fixed at $17°$ from the normal of the sample surface. In the graph, the points represent the intensity of the two contributions which form the emission spectrum: fluores-
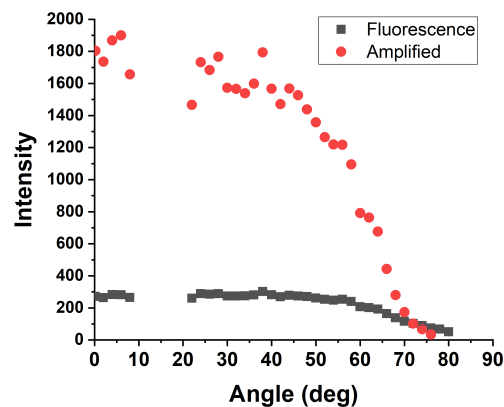
Figure 4.11: (a) Emission of Au NDoA-Py2 as a function of the incident angle of the pump beam.

cence emission (black squares) and amplified emission (red dots).

In summary the Au nanodome array device (Au NDoA-Py2) exhibit an amplified emission with a low threshold $0.9\,\text{mJ/cm}^2$ and a high directionality $17°$ with an angular divergence of $3°$, different to SiO_2 nanodome array device (SiO_2 NDoA-Py2) and Pyridine 2 only. However, SiO_2 NDoA-Py2 present a similar angular behaviour as the Au NDoA-Py2, even if the amplified emission occurs at a fluence ten times higher. Therefore we can deduce that the lattice modes contribute to the directionality of the amplified emission, while the plasmonic properties contribute to reduce the threshold of the amplified emission.

4.3.2 Nanodisk Array - Liquid Gain Medium

The next structure taken into account is the Ag nanodisk array, with a lattice constant of $340\,\text{nm}$ defined by the diameter of PS NSs used during the synthesis process (sec. 2.5). This class of nanoarrays sustaains localized SPR resonances since the metallic disks are well separated and was designed to move the working range more in the visible. However the minimum reachable nanodisks' diameter limited us to the range of Pyridine 2 emission band, as shown in figure 4.2d. From this figure, we expect that an amplified emission arises in the crossing range of Rayleigh mode and the Pyridine emission band. Therefore, we tested these samples by coupling them with Pyridine 2 dissolved in ethanol at a concentration of $\sim 1\,\text{mM}$ (Ag NDiA-Py2).
As showed in figure 4.12 at a pump fluence of $3\,\text{mJ/cm}^2$, we found an amplified emission arise from this coupling, in particular at $720\,\text{nm}$ and an angle of $65°$. Given the high angle of emission, the sample is pumped at normal incidence.
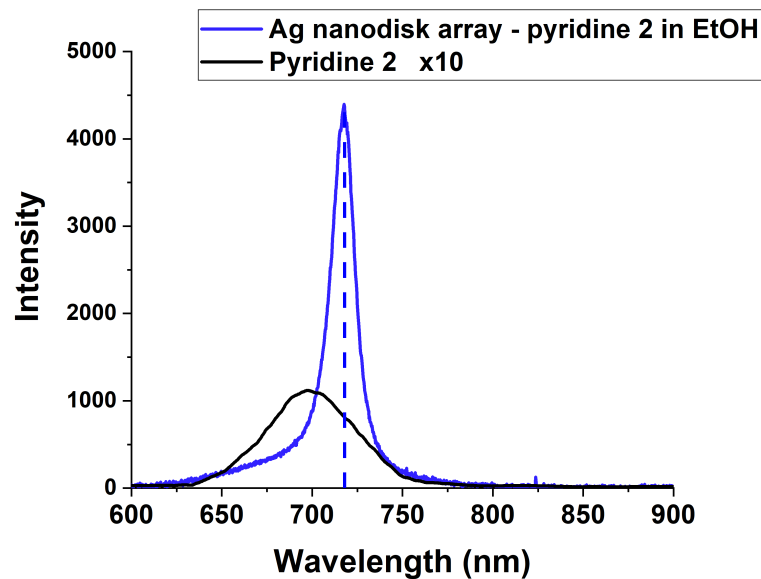
Figure 4.12: Spectral emission of Pyridine 2 in ethanol (black line) and Ag NDiA-Py2 (blue line). The samples were pump at normal incidence with a fluence of about $3\,\text{mJ/cm}^2$ and the emission was collected at $65°$.

Threshold

As for the Au nanodome arrays, Ag nanodisk arrays present a threshold behaviour for the amplified emission. In figure 4.13a, the emission spectra of the Ag NDiA-Py2 are plotted at different pump fluences, showing an increase on the amplified emission peak by increasing the excitation fluence.

The analysis of the spectra by deconvolution of the fluorescence and amplified contributions allowed us to obtain the graph in fig. 4.13b and 4.13c in which the peak intensity and the peak FWHM are reported as a function of pump fluence. For this Ag NDiA-Py2, the threshold occurs at $1.6 \pm 0.1 \, \text{mJ/cm}^2$ (intersection of the two linear fit), which is a little higher but in the same order of magnitude than Au NDoA-Py2 threshold. Furthermore, FWHM of the amplified emission shows a decreasing from $20 \, \text{nm}$ down to $14.6 \, \text{nm}$, that are values comparable with those found for Au nanodome arrays.
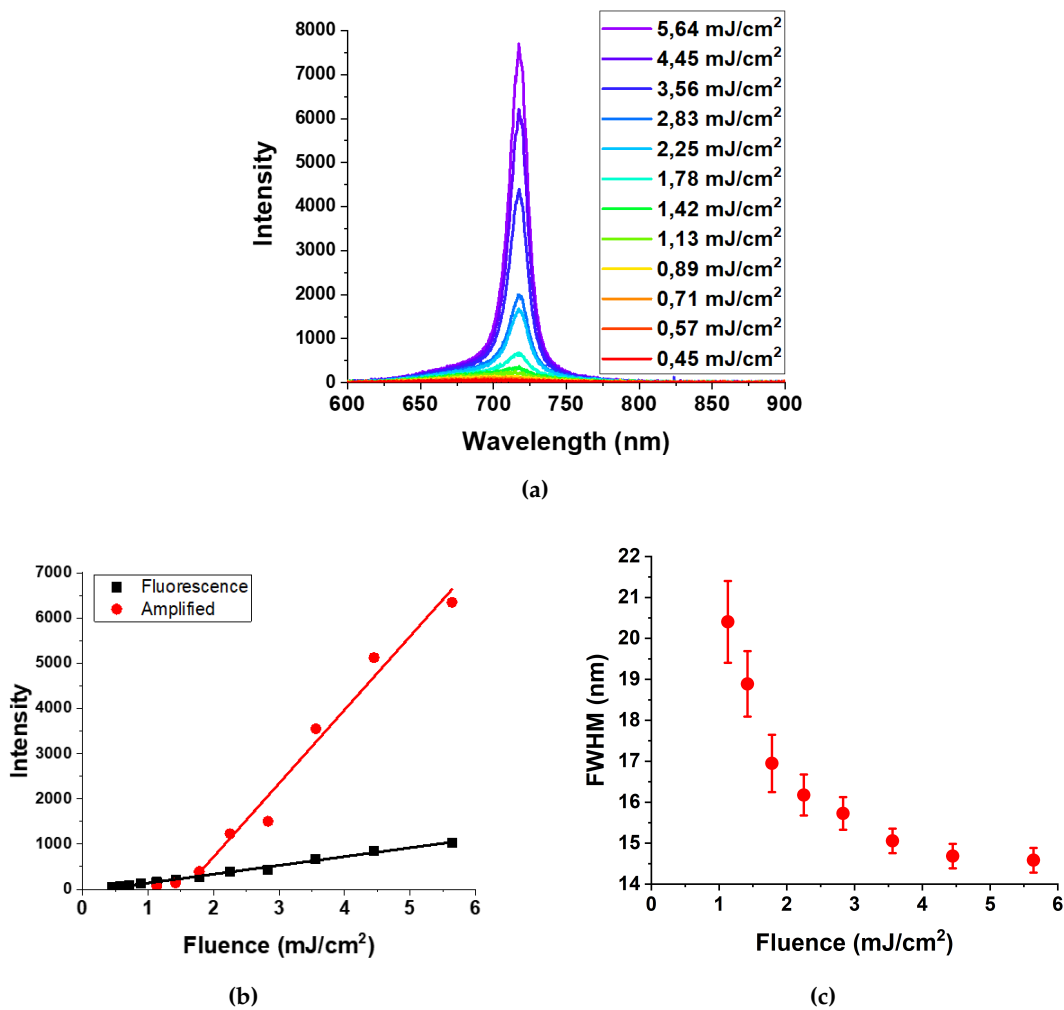
Figure 4.13: Ag NDiA-Py2: **(a)** Emission spectra at different pump fluences. **(b)** Intensity of fluorescence (black points) and amplified emission (red points) as a function of pump fluence. **(c)** Bandwidth behaviour as a function of pump fluence.

Directionality

As for Au NDoA-Py2, Ag NDiA-Py2 presents a strong angle-dependent emission. The directionality of the amplified emission is given by the coupling with the lattice mode. In fact, when the (-1,-1) Rayleigh anomaly intercepts the emission spectra the amplified emission occurs assisted by the LSPR plasmonic properties of the individual nanodisk.

Figure 4.14a shows the angular emission map of the Ag NDiA-Py2. Moreover, data analysis of the amplified emission peaks reveals an emission centred at $65.2° \pm 0.3°$ with a divergence of $14° \pm 1°$ (fig. 4.14b). This wide divergence can be explained by looking at the data figure 4.14a: in the region where the amplified emission occurs, around $65°$, the slope of the Rayleigh anomaly is lower than that one in the Au NDoA-Py2 emission range, spreading the interaction in a broader range of angles, which results in a bigger divergence of the emission.

Au nanodome arrays and Ag nanodisk arrays are structurally different. Au nanodome array is a nanostructured continuous film where LSPR arises in the gap of two neighbour domes, as shown by numerical result 3.4.1, while nanodisks present a LSPR confined in the single disk. The lattice constant is different ($522\,$nm for Au NDoA and $340\,$nm for Ag NDiA), as well as the material, shape and dimensions. However, a similar emission behaviour was found, which confirms that the amplified emission in these nanoarrays occurs as a consequence of the interplay of lattice modes in the nanoarrays and LSPR properties of each nanounit. Therefore, as a perspective, optimizations of shape, lattice path, dimension, composition and gain medium can be done in order to synthesize the most efficient system, taking in to account the optimization of lattice modes and the coupling with the gain medium.
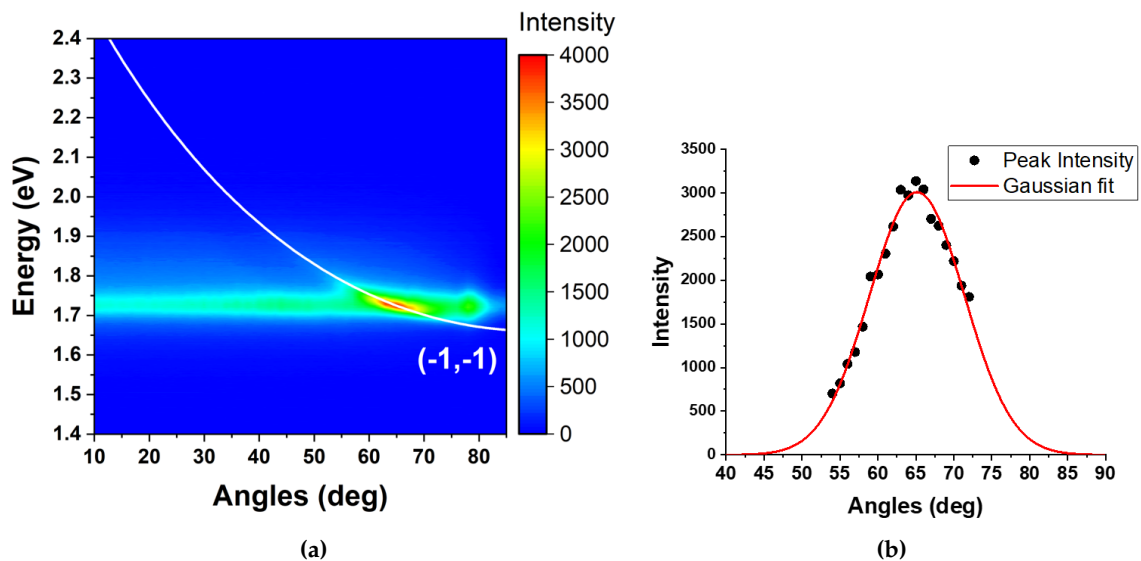
Figure 4.14: (a) Emission map of an Ag NDiA-Py2: the white line identifies the (-1,-1) Rayleigh anomaly. **(b)** Fluorescence (black point) and amplified emission (red points) intensity as a function of the collection angle.

4.3.3 Nanodome Array - Solid State Gain Medium

We also took into account the possibility to synthesize solid state devices, by embedding dye molecules in a polymer matrix. A solid state system is very useful in terms of integrability in optical circuits, and makes the devices more stable and compact with respect to a liquid state system. In particular we coupled the Au nanodome arrays with a Styryl 9M-doped PMMA film with a thickness of about $100\,\mu$m and a concentration of the order of $1\,$mM (Au NDoA-St9M).

As shown in figure 4.15, an amplified emission arises at $795\,$nm for the Au NDoA-St9M. The graph shows also the result obtained for an Au thin film (thickness $70\,$nm) coupled with the dye-doped film (blue line) and the Styryl 9M-doped PMMA film only (black line): no amplified emission is observed at the fluence used. The measurements shown in figure 4.15 were performed with a collection angle of $25°$ and a pumping fluence of $2.5\,$mJ/cm^2.

The different intensity between the emission spectra of the samples with and without the gold film (black and blue lines in figure 4.15) is due to the reflection of the metal film. This last reflects both the incident and emitted radiation, with a reflectivity of $75\,\%$ and $97\,\%$ for the two wavelengths, respectively [120].

Threshold

The graphs in figure 4.16 show the results of the pump fluence dependence of the samples' emission spectra: Au NDoA-St9M, Au thin film coupled with Styryl 9M-doped PMMA layer and Styryl 9M-doped PMMA film.

The Au NDoA-St9M emission intensity at different fluences is plotted in figure 4.16a, showing how by increasing the excitation fluence an amplified emission peak drastically grows over the fluorescence peak. Figure 4.16b displays the amplified emission peak in-
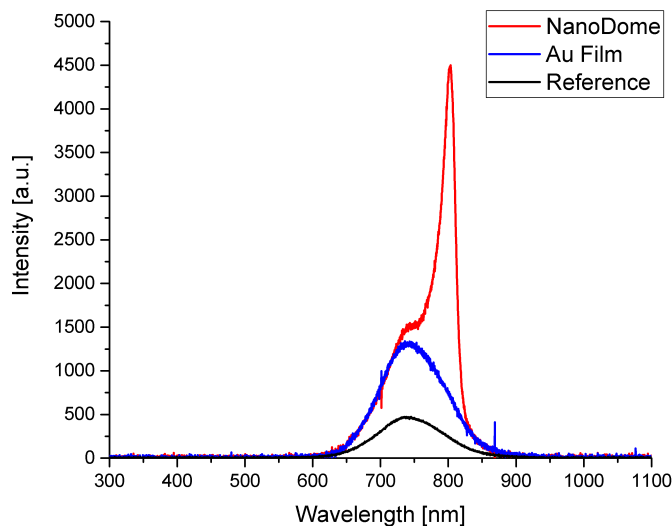
Figure 4.15: Comparison of the emission spectra of Au NDoA-St9M, an Au thin film coupled with Styryl 9M-doped PMMA film and a Styryl 9M-doped PMMA film only. The samples were pumped at $0°$ and was collected at $25°$.

(a)

(b)

(c)

(d) Au thin film coupled with Styryl 9M-doped PMMA layer

(e) Styryl 9M-doped PMMA film
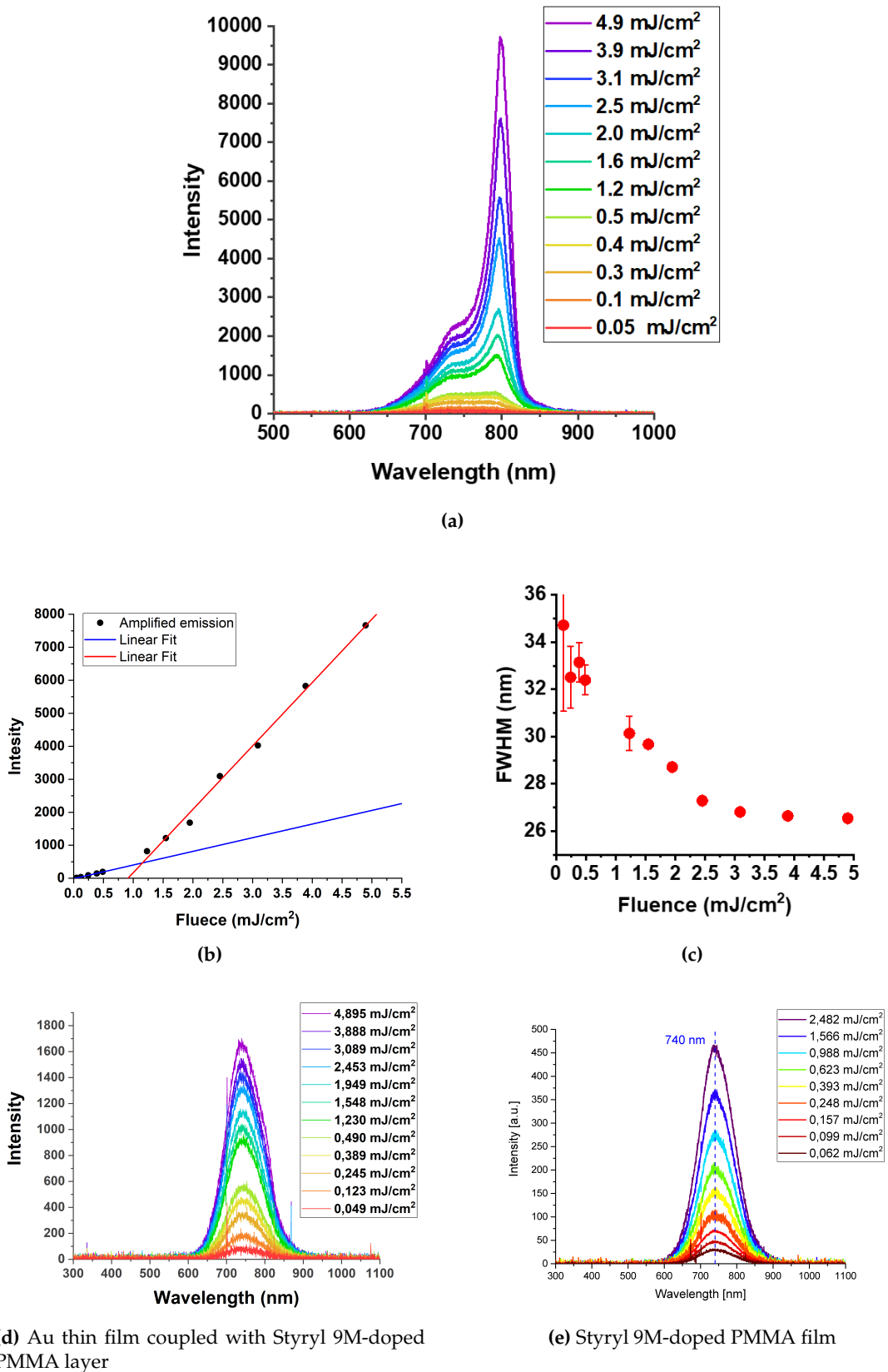
Figure 4.16: Au NDoA-St9M: **(a)** Emission spectra at different pump fluences. **(b)** Amplified emission intensity as a function of pump fluence. **(c)** FWHM of the amplified emission peak as a function of pump fluence. As a comparison:**(d)** Emission spectra at different pump fluences of Au thin film coupled with Styryl 9M-doped PMMA layer. **(e)** Emission spectra at different pump fluences of Styryl 9M-doped PMMA film.

tensity as a function of the pump fluence. How we can see, as for the liquid-state system Au NDoA-Py2, the solid-state system Au NDoA-St9M presents a threshold behaviour: in this case, the intersection of the two linear fits defines the threshold, is at $1.2 \pm 0.1 \, \mathrm{mJ/cm^2}$. The threshold value is comparable with the one obtained with the previous samples in the liquid-state system, Au NDoA-Py2 and Ag NDiA-Py2, suggesting that the amplification of the emission is due to the same phenomena.

The FWHM of the amplified emission peak decreases from 35 nm to 26 nm as a function of pump fluence, suggesting a stimulated emission nature of the amplified emission, further confirming a coupling between Au NDoA and dye emission. However, the FWHM value result higher than the previous ones found for Au NDoA-Py2 and Ag NDiA-Py2 in the liquid-state system.

Figures 4.16d and 4.16e show the emission spectra as a function of the pump fluence for a thin Au film coupled with Styryl 9M-doped PMMA layer and the Styryl 9M-doped PMMA film only, respectively: no threshold behaviour was observed for these samples. This means that the amplification emission in the Au NDoA-St9M occurs as a consequence of the coupling between plasmonic nanoarray and the dye.

Directionality

The directionality properties of Au NDoA-St9M were investigated by angle-dependent measurements from $15°$ to $80°$, with a normal incidence of the pump beam at $2.5 \, \mathrm{mJ/cm^2}$. In figure 4.17a it is reported the map of the intensity spectra as a function of the angle, showing a high intensity spot in the crossing of (-1,-1) Rayleigh anomaly with the dye emission. The emission is directed at $23.7° \pm 0.2°$ with an angular divergence of $6.0° \pm 0.5°$ (figure 4.17b).

It should be noted that the working condition for this sample is lower then the limit imposed by the photobleaching phenomenon, which becomes important above $\sim 4 \, \mathrm{mJ/cm^2}$, as discussed in section 4.2.
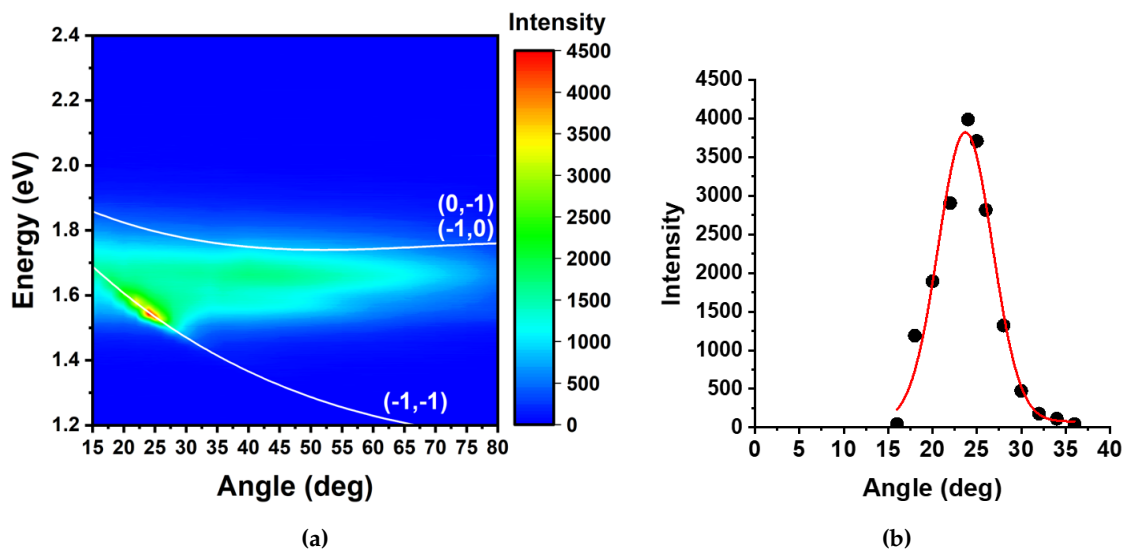
Figure 4.17: (a) Emission map of an Au nanodome array coupled with Styryl 9M-doped PMMA film, the lines white identify the Rayleigh anomalies labelled by Miller indices. **(b)** Amplified emission (black points) intensity peaks as a function of collection angle.

We have shown the possibility to synthesize a solid-state device, with emission properties similar to the other samples made with a liquid-state gain medium. A remarkable characteristic of the solid-state system is the possibility of creating a self-standing device without the need of a substrate. We have then separated the PMMA film from the substrate, maintaining in the dye-doped film the nanostructure array.
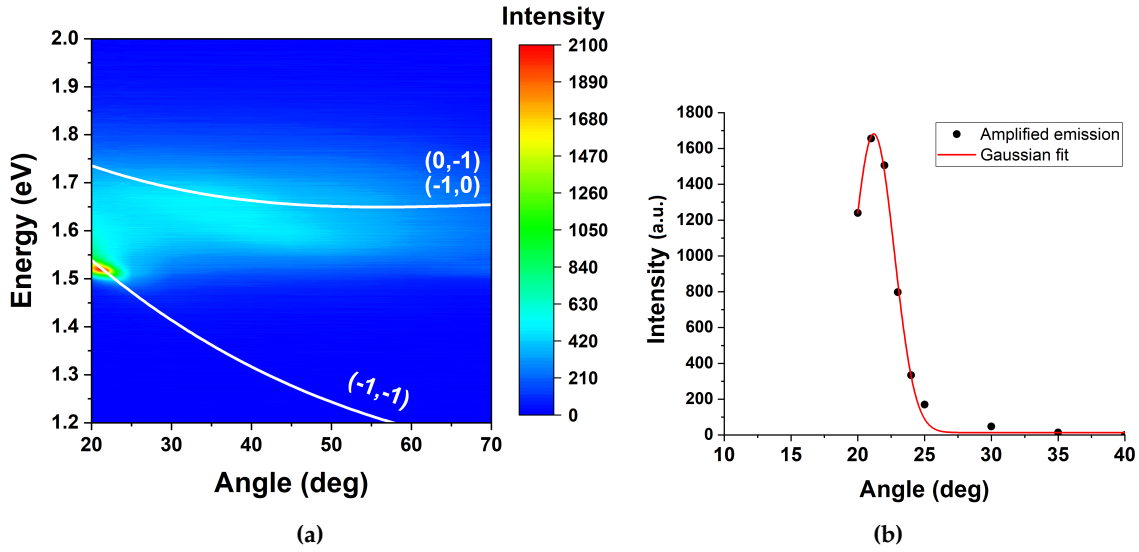
Self-Standing Samples

A self-standing device is very useful for optical integration, by giving the possibility to eliminate the space occupied by the substrate, reducing the dimensions of the final device. Furthermore, there is also the possibility to use a flexible polymer for hosting the dye molecules, opening up to new properties, such as the tunability of the emission.

As for the previous samples, emission as a function of the pump fluence was studied

(a)

(b)

(c)
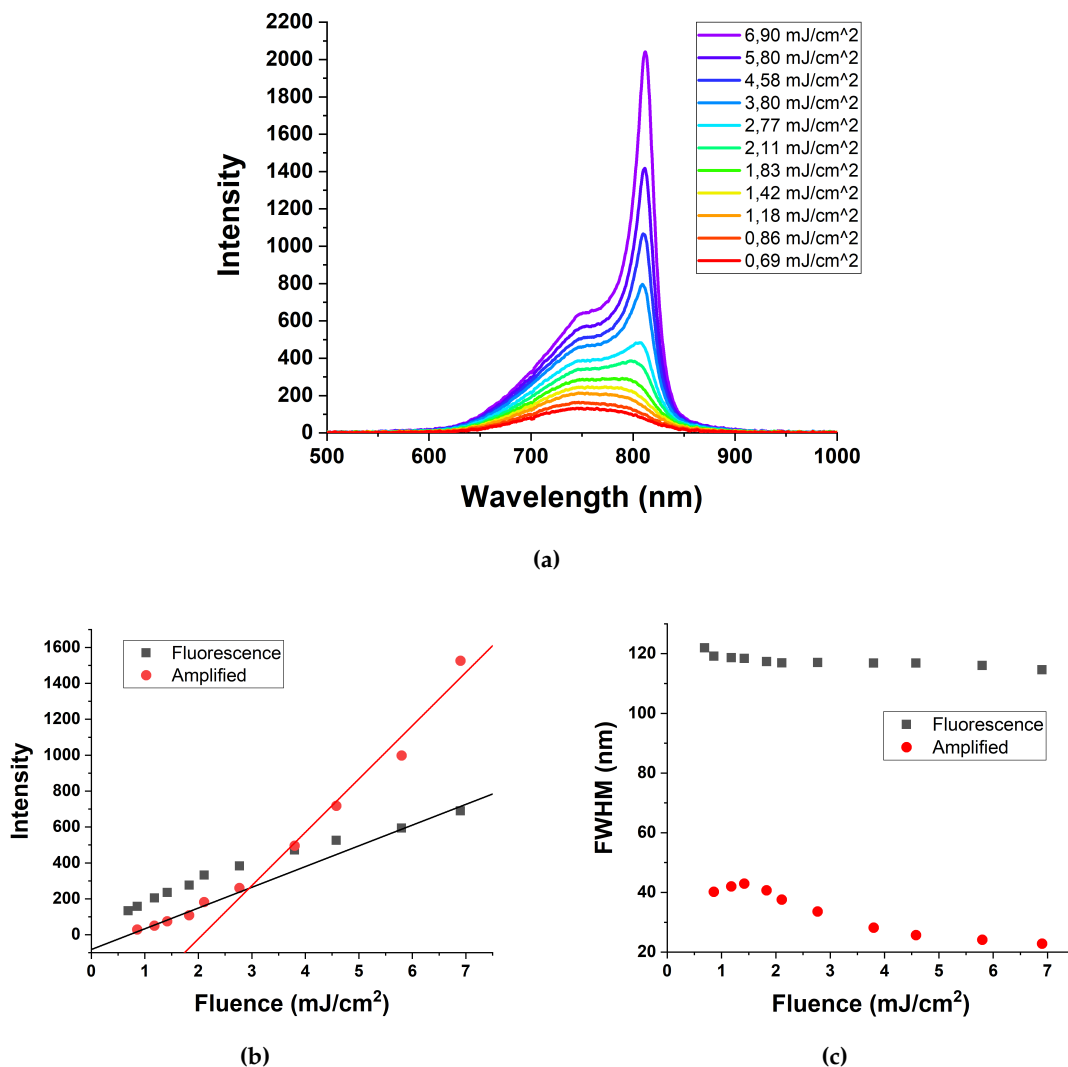
Figure 4.18: Self-standing Au NDoA-St9M: **(a)** emission spectra at different pump fluences. **(b)** Fluorescence (black points) and amplified emission (red points) as a function of the pumping fluence. **(c)** FWHM of fluorescence (black points) and amplified emission (red points) as a function of fluence.

Figure 4.19: Self-standing Au NDoA-St9M: **(a)** Emission map, the white lines identify the Rayleigh anomalies labelled by Miller indices. **(b)** Amplified emission (black points) intensity as a function of the collection angle.

and the results are reported in figure 4.18. The amplified emission arises at $815\,\text{nm}$ with a threshold of $2.9 \pm 0.2\,\text{mJ/cm}^2$ (fig. 4.18b), while FWHM of it decreases down to $22\,\text{nm}$ (fig. 4.18c).

The angular behaviour is shown in figure 4.19a. Rayleigh anomalies are plotted to evaluate the crossing at the emission angle. We found that the amplified emission is directed at $21.3° \pm 0.2°$ with a divergence of $3.7° \pm 0.4°$ (fig. 4.19b).

4.4 Coherence

As described in section 1.1.4, coherence is one of the most important properties of a laser beam and is a unique property that characterizes lasers [42, 43, 121].

Our purpose is to evaluate the temporal coherence property of the synthesized samples, in order to distinguish ASE from lasing emission in our devices and to estimate the coherence length of the emitted beam. To this aim, a modified Michelson interferometer is setted up.

4.4.1 Modified Michelson Interferometer

The scheme of the modified Michelson interferometer set up for the temporal coherence measurements is shown in figure 4.20a. The sample is pumped, as for previous PL spectroscopy by the second harmonic of the Q-switched Nd:YAG laser, and the emitted beam is directed toward the interferometer. A longpass filter ($\lambda > 550\,\text{nm}$) is placed in order to avoid possible reflections from the pump laser to enter the CCD. The emitted beam passes through the filter and an iris before reaching a cube beam splitter, which divides the radiation in two beams with the same intensity and with an angle of $90°$. Two high reflectance silver mirrors ($R > 97.5\,\%$ in Vis-NIR region) are placed at the same distance from the beam splitter and reflect the two beams. The two superposed beams are then collected by a fused silica lens with a focal length of $20\,\text{mm}$. The image formed by the
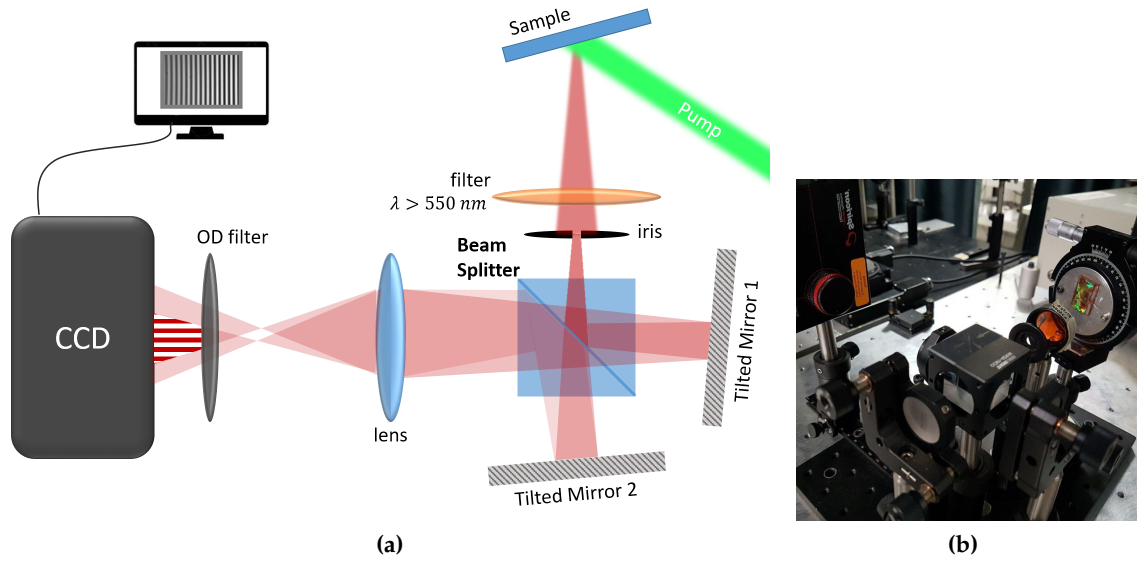
Figure 4.20: (a) Schematic description of the optical setup used for the characterization of temporal coherence properties. **(b)** Photo of the used interferometer.

lens is recoded by a CCD camera (BGP-USB-SP503U Camera by Ophir-Spiricon), which sends the data to a computer. By the BeamScan software we can visualize the interference pattern created by the superposition of the two beams. An optical density filter is used to adjust the input light level on the CCD.

One of the mirrors is placed on a micrometer in order to adjust the mirror position exactly at the same distance of the other mirror, which is in a fixed position from the beam splitter. The two mirrors, unlike a conventional Michelson interferometer, are tilted of about $1°$. A conventional Michelson interferometer, performs a first order correlation $\gamma^{(1)}(\mathbf{r}, \tau)$ (eq. 1.22) of the two light beams as a function of the optical delay τ. In the conventional interferometer, it is introduced an optical path difference (OPD) and, consequently, a time delay $\tau = \text{OPD}/c$, by moving backward one of the two mirrors. Then, the visibility V (eq. 1.24) is calculated as a function of the OPD. The coherence length l_{co} is determined as the FWHM of the visibility function.

In the configuration with the tilted mirrors set up in the present work, these are fixed during the measurement because the tilting introduces a continuous increment of the OPD along one direction, allowing to show in a single image the visibility variation as a function of OPD. Furthermore, the movable mirror can be moved in order to adjust the zero path distance, which can be positioned for example in the center of the image. In the interference image, the distance between two maxima is related to the wavelength of the radiation λ_l according to the expression:

$$\text{OPD} = (\lambda_l/\Lambda)\, x \tag{4.2}$$

where Λ is the period of the fringes and x the coordinate normal to the fringes, i.e. the pixel coordinate. The value of Λ depends on the mirror tilting and the distance of the CCD from the lens. Therefore, these two parameters have been optimized in order to maximise the OPD range in the acquired images.

By analysing the intensity profile of an interference image, we can extrapolate the

(a) Above threshold $1.4\,\mathrm{mJ/cm^2}$

(b) Below threshold $0.4\,\mathrm{mJ/cm^2}$
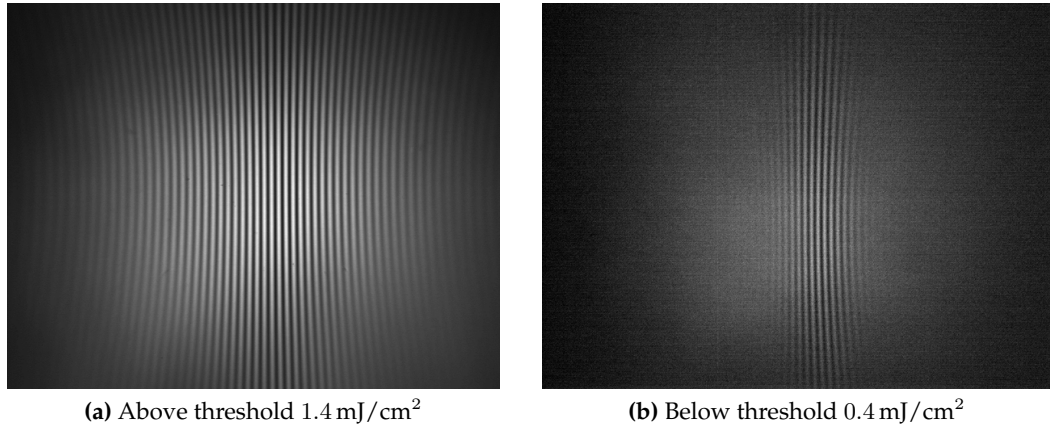
Figure 4.21: Au NDoA-Py2: Interference fringes collected by CCD camera above **(a)** and below **(b)** threshold.

visibility

$$V = \frac{I_{max} - I_{min}}{I_{max} + I_{min}}$$

as a function of the OPD, where I_{max} and I_{min} are the value of the maximum and minimum intensity of the fringes, and estimate the coherence length l_{co} of the emitted beam.

4.4.2 Results

Figure 4.21 displays two interference images collected by the CCD camera of the Au NDoA-Py2: **(a)** was taken at $1.4\,\mathrm{mJ/cm^2}$, above the threshold, while **(b)** at $0.4\,\mathrm{mJ/cm^2}$, below the threshold. First, we can note in figure the presence of interference fringes, which confirms that the emitted beam is coherent.

Moreover, the wide number of visible fringes above the threshold indicates a good level of coherence, in contrast to the small number in figure 4.21b, which has been taken below threshold. In fact, due to the tilting of the mirrors, in the x direction there is a continuous increment of the delay. Therefore, the higher the number of visible fringes, the wider the visibility curve and so the greater the coherence length, as we shall see below.

Extrapolating a profile from the images, we can evaluate the coherence length of these two configurations. The extracted profile is modified by a fast Fourier transform (FFT) filter. The result can be seen in figure 4.22a (4.23a below threshold); the X pixel coordinate (normal to the fringes) is converted into the OPD by equation 4.2.

Thus we are able to calculate the visibility V for each consecutive maximum and minimum, V is plotted as a function of OPD, in figure 4.22b (4.23b below threshold). The data are then fitted by a Gaussian curve whose FWHM identifies the coherence length l_{co} of the emitted beam.

Above the threshold we obtain $l_{co} = 29 \pm 1\,\mu\mathrm{m}$, while below the threshold the coherence length results $l_{co} = 4.2 \pm 0.3\,\mu\mathrm{m}$.

This means that the degree of coherence increase above threshold confirming the stimulated nature of the emitted beam.

As discussed in section 1.1.4, for a stationary beam, the concept of temporal coherence is intimately connected with the monochromaticity by $\tau_{co} = 1/\Delta\nu \simeq \lambda^2/c\Delta\lambda$ where $\Delta\nu$ is the oscillation bandwidth and $\Delta\lambda$ is the spectral bandwidth. Considering an emission at

720 nm with a bandwidth of 14 nm as our system shows, the estimated coherence length is $l_{co}^{(th)} \simeq 37\,\mu$m, which is close to the experimental one of $29\,\mu$m.
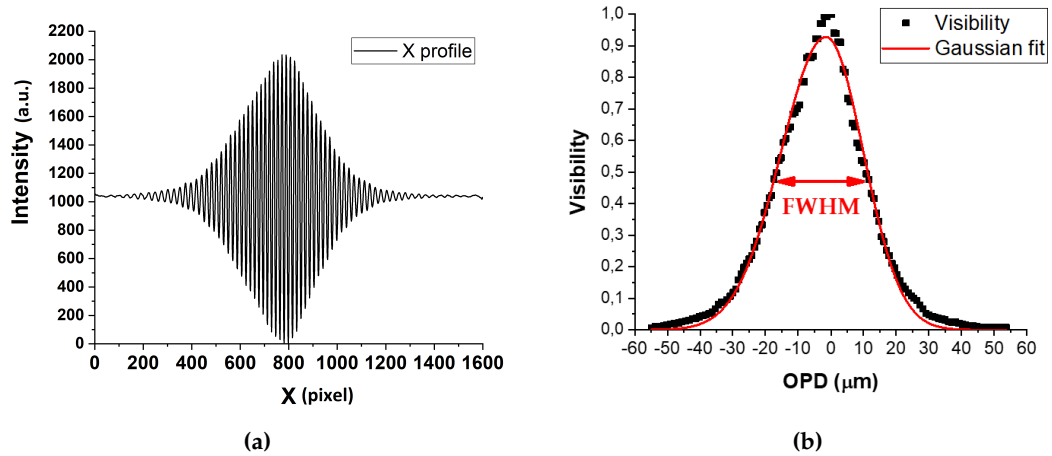
Figure 4.22: Au NDoA-Py2 at $1.4\,$mJ/cm^2, above threshold: **(a)** X profile of interference fringes; **(b)** extrapolated visibility curve from the X profile in **(a)**.
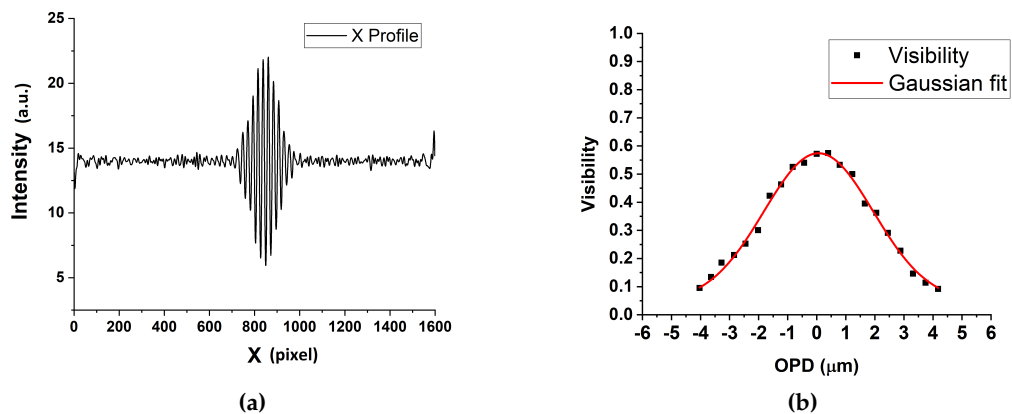
Figure 4.23: Au NDoA-Py2 at $0.4\,$mJ/cm^2, below threshold: **(a)** X profile of interference fringes; **(b)** extrapolated visibility curve from the X profile in **(a)**.

4.5 Prospectives

The amplified emissions in the synthesized samples is the result of the coupling between the dye and the plasmonic modes, in the region between the two high symmetry points of reciprocal space, Γ and M. The amplified emission occurs at the angles of the intersection between the Rayleigh mode and the wavelength region in which the dye is most efficient. However, at these positions the Rayleigh modes have a non-zero slope which leads to a group velocity $v_g = \frac{\partial E}{\hbar \partial k}$ different from zero of the propagating waves in the lattice plane. A group velocity different from zero gives rise to a phase shift in the individual LSPRs, that leads to a phase shift in the emission of different dye molecules, distributed in the lattice plane. The result is a decreasing of the temporal coherence and a broadening of the emission band.

On the other hand, at the high-symmetry points Γ, M or K at the bandedge, the group velocity of the wave is zero. Thus this produces a stationary wave on the whole lattice, which leads to an in-phase oscillation of the individual LSPRs. As a result the temporal coherence of the emission will increase and a narrower bandwidth will be obtain.

For this reason we performed numerical simulations by COMSOL Multiphysics® in order to find a lattice mode at the Γ point, i.e. at incidence equal to zero, by narrow peak next to the diffraction condition in the extinction simulated spectra.

4.5.1 Ag Nanodisk Array

For the nanodisk arrays, since the synthesis process places a limit on the minimum nanododisk's diameter reachable, the simulations were performed for different lattice constants fixing the nanodisks' diameter at the corresponding minimum reachable. The parameters used for these simulation are shown in table 4.1

Table 4.1: Numerical simulation parameters for different Ag nanodisk arrays.

Lattice Constant a (nm)	Diameter D (nm)	Height h (nm)	Refractive Index n
248	83	70	1.33 - 1.5
340	113	70	1.33 - 1.5
418	139	70	1.33 - 1.5
522	150	150	1.33 - 1.5

The used model is the same as the one presented in section 3.6. We show in figure 4.24 the extinction spectra with different lattice constants a: **(a)** 248 nm, **(b)** 340 nm, **(c)** 418 nm, **(d)** 522 nm.

All the spectra show two distinct peaks: one, broader and redshifted, which can be associated to the dipolar LSPRs of each disk; the other, narrower and blueshifted, can be associated to the SLRs.

It is important to note that the sample with lattice constant of 522 nm and a refractive index of 1.5 presents a strong SLR peak in the visible range which is a promising candidate to improve the performance of our devices.
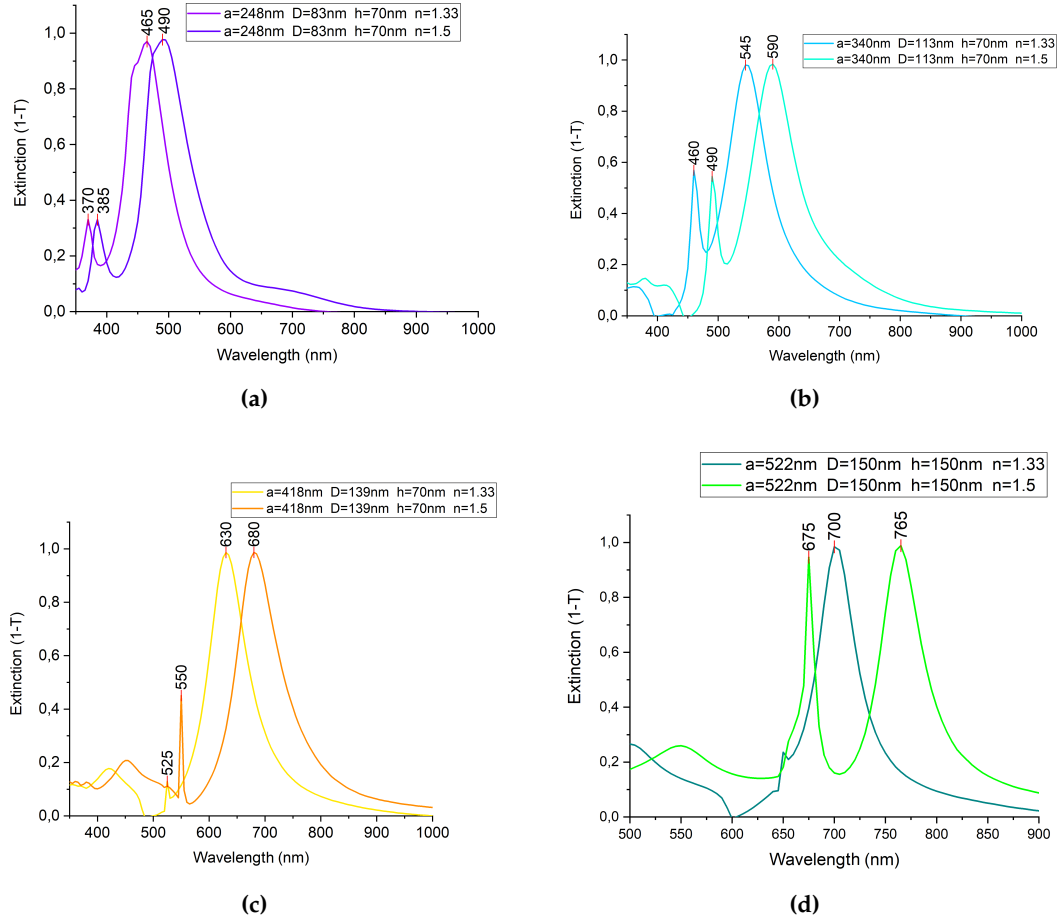
Figure 4.24: Numerical em simulated extinction spectra of Ag nanodisk arrays with different parameters as reported in table 4.1: **(a)** $a = 248\,\text{nm}$, **(b)** $a = 340\,\text{nm}$, **(c)** $a = 418\,\text{nm}$, **(d)** $a = 522\,\text{nm}$.

4.5.2 Ag Nanosphere Array

Another structure taken in to account to find a SLR at Γ point, is the Ag nanosphere array, described in section 2.6. In order to obtain nanosphere arrays, we performed thermal annealing on the nanoprism array. This process results as a blueshift of the LSPR peak in the visible region, as shown in figure 2.18e and 2.18f, and suitable to show an SLR with a structure having a lattice constant $a = 522\,\text{nm}$. For this reason the numerical simulations have been performed with nanospheres arranged in a honeycomb lattice with a lattice constant $a = 522\,\text{nm}$.

The numerical simulations have been performed by the software COMSOL Multiphysics®, and the details of the simulations are described in section 3.3. The used 3D model and the parameters are reported in figure 4.25a and 4.25b, respectively. The nanosphere honeycomb lattice was modelled with a rhomboidal conventional primitive cell with a lattice constant of $a = 522\,\text{nm}$ that corresponds to a side of the cell. In the cell, two spheres with 100 or 150 nm diameter are placed in $(0, \pm a/2\sqrt{3})$, as shown in figure 4.25b. Each lateral face of the cell has a PBC condition with its opposite and the model has PMLs on the top and the bottom, in the $\hat{z}$ direction. The SiO$_2$ substrate is modelled by a non dissipative material with a refractive index $n = 1.45$ and a thickness of 500 nm. Instead the medium on the top is modelled by a non dissipative material with a refractive index
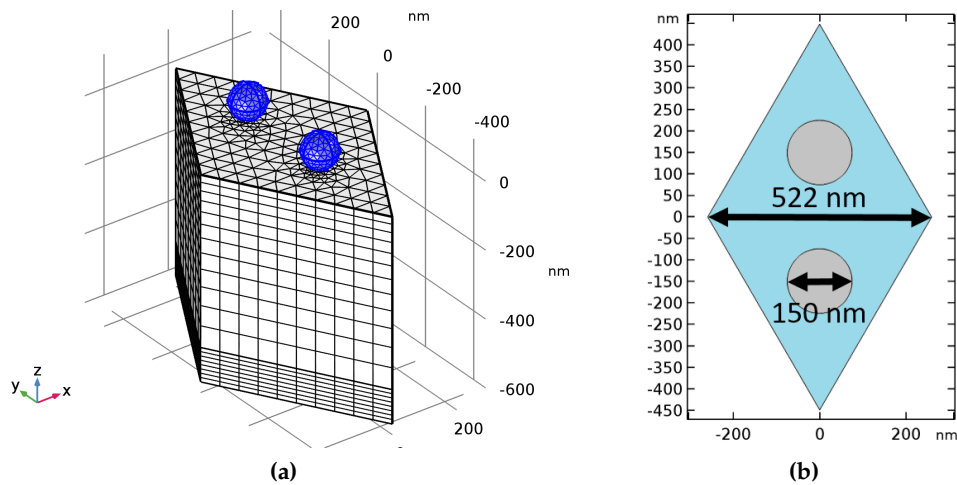
Figure 4.25: (a) Representation of 3D model used for Ag nanosphere array siulation where spheres are highlighted and mesh is shown. **(b)** Principal geometric parameters used in the simulation, the sketch shows the $\hat{x}\hat{y}$ plane at $z = 75$.

$n = 1.33 - 1.43 - 1.5$ and a thickness of $700\,\text{nm}$.

FEM simulations in FDFD have been performed in the wavelength range of $400 - 1000\,\text{nm}$. The incident beam is a EM plane wave with amplitude $E_0 = 1\,\text{V/m}$.

The simulated extinction spectra are displayed in figure 4.26, and they exhibit a peak associated to SLRs. In particular, in figure 4.26a, nanospheres with diameter of $100\,\text{nm}$ present a LSPR at 450, 470 and $490\,\text{nm}$ for the three different refractive indices, and for $n = 1.43$ and 1.5 a SLR peak occurs at 655 and $675\,\text{nm}$, respectively. Moreover, in figure 4.26b, nanospheres with diameter of $150\,\text{nm}$ present a LSPR at 430, 455 and $475\,\text{nm}$, and a stronger SLR peak at 655, 675 and $705\,\text{nm}$, for the three different refractive indices respectively.

This demonstrates that this type of arrays are optimal candidates to develop plasmonic nanolasers, thanks to their strong SLRs.

(a) Diameter of $100\,\text{nm}$

(b) Diameter of $150\,\text{nm}$
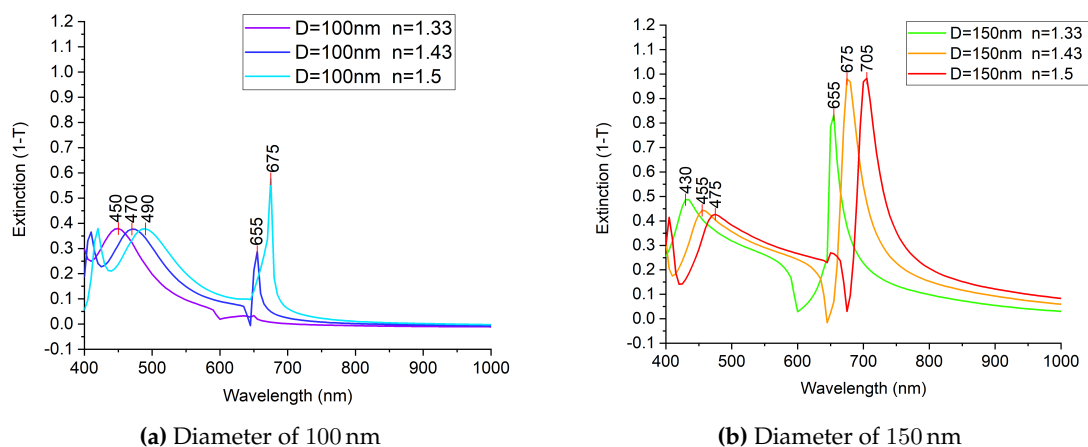
Figure 4.26: Simulated extinction spectra at three different refractive index 1.33, 1.43, 1.5: **a** spheres' diameter $100\,\text{nm}$ **b** spheres' diameter $150\,\text{nm}$.

Chapter 5

Conclusions

In this work the possibility to reach lasing emission in plasmonic nanolaser devices has been studied. The synthesized plasmonic nanolasers exhibit amplified emission by the coupling between plasmonic nanostructure arrays and laser dyes. Two principal plasmonic nanostructure arrays have been investigated: gold nanodome arrays and silver nanodisk arrays.

Au nanodome arrays and Ag nanodisk arrays arranged in a two-dimensional hexagonal lattice have been designed, synthesized and characterised. The possibility to synthesize this type of devices in a cost-effective way and with a high-throughput technique has been also proven. It has been shown how nanosphere sithography (NSL) represents a powerful and reliable technique to realize high ordered nanostructure arrays based on self-assembled monolayers of polystyrene nanospheres as lithographic masks. Moreover, the versatility of NSL combined with Reactive Ion Etching (RIE), Physical Vapor Deposition (PVD) and thermal annealing has allowed us to develop different nanofabrication protocols and finely control the morphology of the nanostructures and thus the plasmonic properties of the nanoarrays.

The optical properties of our synthesized nanostructures have been investigated in TM mode, reconstructing the optical band structure along the high symmetry directions ΓM and ΓK of the reciprocal space. We have thus observed an interaction between the lattice modes and the plasmonic resonances driven by the Rayleigh anomalies. Then, suitable dye emitters were selected in order to couple their emission with the optical modes of the nanoarray. In addition, in order to optimize the plasmonic properties and the local field enhancement of the metallic nanostructures, numerical simulations by COMSOL Multiphysics$^\circledR$ were performed.

As expected, the interaction between dye and plasmonic structure generated an amplified emission. In the Au nanodome array coupled with Pyridine 2 dissolved in ethanol, the plasmonic structure provides a sufficient feedback action to overcome the energy loss of metal nanostructures. Consequently, a narrow amplified emission arises at $720\,\mathrm{nm}$ with a FWHM of $14\,\mathrm{nm}$. This amplification exhibits a threshold behaviour and the threshold is at $0.9\,\mathrm{mJ/cm^2}$. Furthermore, the Au nanodome array has a highly directional emission that occurs at $17°$ with an angular divergence of $3°$ and takes place along the Rayleigh anomaly mode identified by the Miller index $(-1, -1)$.

In order to strengthen our results, we additionally compared the properties of Au nanodome arrays with silica nanodomes array ones and with the pyridine 2 solution only. No clear threshold behaviour is observed in this case, even if a narrow emission was found for the SiO_2 nanodome array, at high fluences (around 1 order of magnitude

larger) and with a broader FWHM with respect to the Au nanoarrays. Moreover, silica nanodome array presents an amplification at the same angle of the Au one, even if at higher pump fluence. From this comparison, we concluded that lattice modes give a contribution to the emission directionality, while plasmonic modes provide a reduced lasing threshold to overcome the energy loss.

We investigated also Ag hexagonal nanodisk arrays, which show a behavior similar to the Au nanodome arrays. We found a lasing threshold at $1.6\,\mathrm{mJ/cm^2}$, with also a similar FWHM. Due to the different lattice path, the emission occurs at $65°$ and presents an angular divergence of about $14°$, broader than the previous one, due to the lower slope in the reciprocal space of the coupled mode.

Moreover, we considered a nanolaser with a solid state gain medium for the interest in applications and for the device integration on a chip. The laser dye Styryl 9M, suitable for this purpose, was embedded in a PMMA film, presenting a fluorescence emission at $740\,\mathrm{nm}$. When the dye-doped film is coupled with an Au nanodome array, this solid state system presents an amplified emission at $795\,\mathrm{nm}$ with a threshold of $1.2\,\mathrm{mJ/cm^2}$ and a FWHM of about $26\,\mathrm{nm}$. The sample has also a directional emission at $24°$ and with an angular divergence of $6°$. In addition, we have demonstrated the possibility to eliminate the substrate, creating a self-standing device, which exhibits an amplified emission with similar properties of that with the substrate.

Finally, in order to discern the spontaneous or stimulated nature of the emission, we performed coherence measurements of the emitted beam. By a modified Michelson interferometer, a coherence length of about $29\,\mu\mathrm{m}$ was obtained for the Au nanodome arrays above threshold. This result demonstrated that a coherent, low-threshold and highly directional emission can be obtained by coupling a suitable fluorescent dye to a properly designed virtual cavity realized by an ordered array of plasmonic nanostructures.

With the prospect to improve these remarkable results, by increasing monochromaticity and coherence properties, we have studied the possibility to realize by NSL a suitable nanostructure which presents plasmonic modes at the high symmetry point Γ of the reciprocal lattice. Therefore, by FEM numerical simulations and optical measurements, we have shown how Ag nanoprism arrays arranged in a honeycomb lattice could satisfy this request.

On the other hand, the possibility of selecting different materials to be used both for the nanostructures and for the gain medium makes the device adaptable to many situations. It would be possible in principle to explore the whole visible range, with the possibility of a laser emission tunable by varying for example the grating period of the nanostructures or to make multi-color devices implementing more gain media. This opens the way to many studies for the future, placing these devices at the center of interest for new applications in many fields, including diagnosis, sensing, communications or optical circuits.

List of Figures

Bibliography

[1] Richard P Feynman. There's plenty of room at the bottom. *California Institute of Technology, Engineering and Science magazine*, 1960. 1

[2] S. A. Maier. *Plasmonics: fundamental and application*. Springer, 2007. 1, 5, 15

[3] R Gordon Gould. The laser, light amplification by stimulated emission of radiation. In *The Ann Arbor Conference on Optical Pumping, the University of Michigan*, volume 15, page 128, 1959. 1, 5

[4] TH Maiman. Stimulated emission of radiation in ruby. *Nature*, 187:493–494, 1960. 1

[5] Ifor David Williams Samuel and Graham Alexander Turnbull. Organic semiconductor lasers. *Chemical Reviews*, 107(4):1272–1295, 2007. 1

[6] JM Pitarke, VM Silkin, EV Chulkov, and PM Echenique. Theory of surface plasmons and surface-plasmon polaritons. *Reports on progress in physics*, 70(1):1, 2006. 2

[7] David J Bergman and Mark I Stockman. Surface plasmon amplification by stimulated emission of radiation: quantum generation of coherent surface plasmons in nanosystems. *Physical review letters*, 90(2):027402, 2003. 2

[8] Martin T Hill, Yok-Siang Oei, Barry Smalbrugge, Youcai Zhu, Tjibbe De Vries, Peter J Van Veldhoven, Frank WM Van Otten, Tom J Eijkemans, Jarosław P Turkiewicz, Huug De Waardt, et al. Lasing in metallic-coated nanocavities. *Nature Photonics*, 1(10):589, 2007. 2

[9] MA Noginov, G Zhu, AM Belgrave, Reuben Bakker, VM Shalaev, EE Narimanov, S Stout, E Herz, T Suteewong, and U Wiesner. Demonstration of a spaser-based nanolaser. *Nature*, 460(7259):1110–1112, 2009. 2

[10] Rupert F Oulton, Volker J Sorger, Thomas Zentgraf, Ren-Min Ma, Christopher Gladden, Lun Dai, Guy Bartal, and Xiang Zhang. Plasmon lasers at deep subwavelength scale. *Nature*, 461(7264):629, 2009.

[11] Ren-Min Ma, Rupert F Oulton, Volker J Sorger, Guy Bartal, and Xiang Zhang. Room-temperature sub-diffraction-limited plasmon laser by total internal reflection. *Nature materials*, 10(2):110, 2011.

[12] Jae Yong Suh, Chul Hoon Kim, Wei Zhou, Mark D Huntington, Dick T Co, Michael R Wasielewski, and Teri W Odom. Plasmonic bowtie nanolaser arrays. *Nano Letters*, 12(11):5769–5774, 2012. 2, 27

[13] Yu-Jung Lu, Chun-Yuan Wang, Jisun Kim, Hung-Ying Chen, Ming-Yen Lu, Yen-Chun Chen, Wen-Hao Chang, Lih-Juann Chen, Mark I Stockman, Chih-Kang Shih, et al. All-color plasmonic nanolasers with ultralow thresholds: autotuning mechanism for single-mode lasing. *Nano letters*, 14(8):4381–4388, 2014.

[14] Ekaterina I Galanzha, Robert Weingold, Dmitry A Nedosekin, Mustafa Sarimollaoglu, Jacqueline Nolan, Walter Harrington, Alexander S Kuchyanov, Roman G Parkhomenko, Fumiya Watanabe, Zeid Nima, et al. Spaser as a biological probe. *Nature communications*, 8:15528, 2017.

[15] Kun-Ching Shen, Chen-Ta Ku, Chiieh Hsieh, Hao-Chung Kuo, Yuh-Jen Cheng, and Din Ping Tsai. Deep-ultraviolet hyperbolic metacavity laser. *Advanced Materials*, 30 (21):1706918, 2018. 2

[16] Alastair D Humphrey and William L Barnes. Plasmonic surface lattice resonances on arrays of different lattice symmetry. *Physical Review B*, 90(7):075404, 2014. 2, 26

[17] Nikolay I Zheludev, SL Prosvirnin, N Papasimakis, and VA Fedotov. Lasing spaser. *Nature Photonics*, 2(6):351, 2008. 2, 27

[18] Frerik van Beijnum, Peter J van Veldhoven, Erik Jan Geluk, Michiel JA de Dood, W Gert, and Martin P van Exter. Surface plasmon lasing observed in metal hole arrays. *Physical Review Letters*, 110(20):206802, 2013. 2

[19] Wei Zhou, Montacer Dridi, Jae Yong Suh, Chul Hoon Kim, Dick T Co, Michael R Wasielewski, George C Schatz, Teri W Odom, et al. Lasing action in strongly coupled plasmonic nanocavity arrays. *Nature Nanotechnology*, 8(7):506–511, 2013. 2, 27, 77

[20] Ran Li, Danqing Wang, Jun Guan, Weijia Wang, Xianyu Ao, George C Schatz, Richard Schaller, and Teri W Odom. Plasmon nanolasing with aluminum nanoparticle arrays. *JOSA B*, 36(7):E104–E111, 2019. 2

[21] Claire Deeb, Zhi Guo, Ankun Yang, Libai Huang, and Teri W Odom. Correlating nanoscopic energy transfer and far-field emission to unravel lasing dynamics in plasmonic nanocavity arrays. *Nano letters*, 18(2):1454–1459, 2018. 2

[22] Thang B Hoang, Gleb M Akselrod, Ankun Yang, Teri W Odom, and Maiken H Mikkelsen. Millimeter-scale spatial coherence from a plasmon laser. *Nano letters*, 17(11):6690–6695, 2017. 2

[23] Weijia Wang, Nicolas Watkins, Ankun Yang, Richard D Schaller, George C Schatz, and Teri W Odom. Ultrafast dynamics of lattice plasmon lasers. *The journal of physical chemistry letters*, 2019. 2

[24] Danqing Wang, Marc R Bourgeois, Won-Kyu Lee, Ran Li, Dhara Trivedi, Michael P Knudson, Weijia Wang, George C Schatz, and Teri W Odom. Stretchable nanolasing from hybrid quadrupole plasmons. *Nano letters*, 18(7):4549–4555, 2018. 2

[25] Ankun Yang, Thang B Hoang, Montacer Dridi, Claire Deeb, Maiken H Mikkelsen, George C Schatz, and Teri W Odom. Real-time tunable lasing from plasmonic nanocavity arrays. *Nature Communications*, 6, 2015. 2

[26] Danqing Wang, Ankun Yang, Weijia Wang, Yi Hua, Richard D Schaller, George C Schatz, and Teri W Odom. Band-edge engineering for controlled multi-modal nanolasing in plasmonic superlattices. *Nature nanotechnology*, 12(9):889, 2017. 2

[27] TK Hakala, HT Rekola, AI Väkeväinen, J-P Martikainen, M Nečada, AJ Moilanen, and P Törmä. Lasing in dark and bright modes of a finite-sized plasmonic lattice. *Nature communications*, 8:13687, 2017. 2, 77

[28] Heikki T Rekola, Tommi K Hakala, and Päivi Törmä. Lasing in small-sized aluminum nanoparticle arrays. In *Metamaterials, Metadevices, and Metasystems 2017*, volume 10343, page 103432E. International Society for Optics and Photonics, 2017. 2

[29] Sara Pourjamal, Tommi K Hakala, Marek Nečada, Francisco Freire-Fernàndez, Mikko Kataja, Heikki Rekola, Jani-Petri Martikainen, Päivi Törmä, and Sebastiaan van Dijken. Lasing in ni nanodisk arrays. *ACS nano*, 13(5):5686–5692, 2019. 2

[30] Rui Guo, Marek Nečada, Tommi K Hakala, Aaro I Väkeväinen, and Päivi Törmä. Lasing at k points of a honeycomb plasmonic lattice. *Physical review letters*, 122(1): 013901, 2019. 2

[31] Heikki T Rekola, Tommi K Hakala, and Päivi Törmä. One-dimensional plasmonic nanoparticle chain lasers. *ACS Photonics*, 5(5):1822–1826, 2018. 2

[32] Konstantinos S Daskalakis, Aaro I Väkeväinen, Jani-Petri Martikainen, Tommi K Hakala, and Päivi Törmä. Ultrafast pulse generation in an organic nanoparticle-array laser. *Nano letters*, 18(4):2658–2665, 2018. 2

[33] Päivi Törmä. Nanolasing: Multimode superlattice arrays. *Nature nanotechnology*, 12(9):838, 2017. 2

[34] A Hinke Schokker, Floor van Riggelen, Yakir Hadad, Andrea Alù, and A Femius Koenderink. Systematic study of the hybrid plasmonic-photonic band structure underlying lasing action of diffractive plasmon particle lattices. *Physical Review B*, 95(8):085409, 2017. 2, 77

[35] Ke Guo and A Femius Koenderink. Spatial intensity distribution in plasmonic particle array lasers. *Physical Review Applied*, 11(2):024025, 2019.

[36] Ke Guo, Sachin Kasture, and A Femius Koenderink. Plasmon antenna array "patchwork" lasers—towards low etendue, speckle free light sources. *OSA Continuum*, 2(6):1982–1997, 2019.

[37] A Femius Koenderink. Plasmon nanocavity array lasers: Cooperating over losses and competing for gain. *ACS nano*, 13(7):7377–7382, 2019. 2

[38] A Hinke Schokker and A Femius Koenderink. Lasing in quasi-periodic and aperiodic plasmon lattices. *Optica*, 3(7):686–693, 2016. 2

[39] Hsin-Yu Wu, Longju Liu, Meng Lu, and Brian T Cunningham. Lasing emission from plasmonic nanodome arrays. *Advanced Optical Materials*, 2016. 2

[40] John C Hulteen and Richard P Van Duyne. Nanosphere lithography: A materials general fabrication process for periodic particle array surfaces. *Journal of Vacuum Science & Technology A: Vacuum, Surfaces, and Films*, 13(3):1553–1558, 1995. 3

[41] Christy L Haynes and Richard P Van Duyne. Nanosphere lithography: a versatile nanofabrication tool for studies of size-dependent nanoparticle optics. *The Journal of Physical Chemistry B*, 105(24):5599–5611, 2001. 3, 31

[42] O Svelto. *Principles of Lasers*. Heidelberg: Springer, 2010. 5, 88

[43] Anthony E Siegman. *Lasers*, volume 37. Mill Valley, CA, 1986. 5, 9, 28, 77, 88

[44] Albert Einstein. Zur quantentheorie der strahlung (on the quantum theory of radiation). *Physikalische Zeitschrift*, 18, 1917. 5

[45] E. Hecht. *Optics*. Pearson education. Addison-Wesley, 2002. ISBN 9780321188786. URL https://books.google.it/books?id=T3ofAQAAMAAJ. 13

[46] M Vollmer and U Kreibig. *Optical properties of metal clusters*. Springer Ser. Mat. Sci, 1995. 15

[47] Robert W. Boyd. *Nonlinear Optics*. Academic Press, 2003. 16

[48] Peter B Johnson and R-W_ Christy. Optical constants of the noble metals. *Physical Review B*, 6(12):4370, 1972. 17, 18, 19

[49] Tatsuya Kashiwa and Ichiro Fukai. A treatment by the fd-td method of the dispersive characteristics associated with electronic polarization. *Microwave and Optical Technology Letters*, 3(6):203–205, 1990. 17

[50] F Hao and P Nordlander. Efficient dielectric function for fdtd simulation of the optical properties of silver and gold nanoparticles. *Chemical Physics Letters*, 446(1):115–118, 2007. 18

[51] Gustav Mie. Beiträge zur optik trüber medien, speziell kolloidaler metallösungen (contributions to the optics of diffusing media). *Annalen der Physik*, 330(3):377–445, 1908. 19, 22, 35, 57

[52] Craig F Bohren and Donald R Huffman. *Absorption and scattering of light by small particles*. John Wiley & Sons, 2008. 21

[53] Uwe Kreibig and Michael Vollmer. *Optical properties of metal clusters*, volume 25. Springer Science & Business Media, 2013. 19

[54] R Gans. Fortpflanzung des lichts durch ein inhomogenes medium (propagation of light through a inhomogeneous medium). *Annalen der Physik*, 352(14):709–736, 1915. 19

[55] John David Jackson. *Classical electrodynamics*. Wiley, 1999. 21

[56] M Meier and A Wokaun. Enhanced fields on large metal particles: dynamic depolarization. *Optics Letters*, 8(11):581–583, 1983. 21

[57] Alexander Moroz. Depolarization field of spheroidal particles. *JOSA B*, 26(3):517–527, 2009. 21

[58] Th Kokkinakis and K Alexopoulos. Observation of radiative decay of surface plasmons in small silver particles. *Physical Review Letters*, 28(25):1632, 1972. 22

[59] Edward Mills Purcell. Spontaneous emission probabilities at radio frequencies. *Physical Review*, 69:681, 1946. 22

[60] Pascal Anger, Palash Bharadwaj, and Lukas Novotny. Enhancement and quenching of single-molecule fluorescence. *Physical Review Letters*, 96(11):113002, 2006. 22

[61] M Meier, A Wokaun, and Paul F Liao. Enhanced fields on rough surfaces: dipolar interactions among particles of sizes exceeding the rayleigh limit. *JOSA B*, 2(6): 931–949, 1985. 23

[62] C Ropers, DJ Park, G Stibenz, G Steinmeyer, J Kim, DS Kim, and C Lienau. Femtosecond light transmission and subradiant damping in plasmonic crystals. *Physical review letters*, 94(11):113901, 2005. 23

[63] FJ García De Abajo. Colloquium: Light scattering by particle and hole arrays. *Reviews of Modern Physics*, 79(4):1267, 2007. 23

[64] Robert Williams Wood. On a remarkable case of uneven distribution of light in a diffraction grating spectrum. *Proceedings of the Physical Society of London*, 18(1):269, 1902. 23

[65] Lord Rayleigh. Iii. note on the remarkable case of diffraction spectra described by prof. wood. *The London, Edinburgh, and Dublin Philosophical Magazine and Journal of Science*, 14(79):60–65, 1907. 23

[66] Ugo Fano. The theory of anomalous diffraction gratings and of quasi-stationary waves on metallic surfaces (sommerfeld's waves). *JOSA*, 31(3):213–222, 1941. 23

[67] Mohammad Ramezani, Gabriel Lozano, Marc A Verschuuren, and Jaime Gómez-Rivas. Modified emission of extended light emitting layers by selective coupling to collective lattice resonances. *Physical Review B*, 94(12):125406, 2016. 23

[68] Ugo Fano. Effects of configuration interaction on intensities and phase shifts. *Physical Review*, 124(6):1866, 1961. 25

[69] Shengli Zou, Nicolas Janel, and George C Schatz. Silver nanoparticle array structures that produce remarkably narrow plasmon lineshapes. *The Journal of chemical physics*, 120(23):10871–10875, 2004. 25

[70] Uri Laor and George C Schatz. The role of surface roughness in surface enhanced raman spectroscopy (sers): the importance of multiple plasmon resonances. *Chemical Physics Letters*, 82(3):566–570, 1981. 25

[71] SRK Rodriguez, MC Schaafsma, A Berrier, and J Gómez Rivas. Collective resonances in plasmonic crystals: Size matters. *Physica B: Condensed Matter*, 407(20): 4081–4085, 2012. 26

[72] Dhara J Trivedi, Danqing Wang, Teri W Odom, and George C Schatz. Model for describing plasmonic nanolasers using maxwell-liouville equations with finite-difference time-domain calculations. *Physical Review A*, 96(5):053825, 2017. 27, 30

[73] Themistoklis PH Sidiropoulos, Robert Röder, Sebastian Geburt, Ortwin Hess, Stefan A Maier, Carsten Ronning, and Rupert F Oulton. Ultrafast plasmonic nanowire lasers near the surface plasmon frequency. *Nature Physics*, 10(11):870, 2014. 27

[74] Shih-Hui Chang and Allen Taflove. Finite-difference time-domain model of lasing action in a four-level two-electron atomic system. *Optics express*, 12(16):3827–3833, 2004. 28

[75] Gabriela M Slavcheva, John M Arnold, and Richard W Ziolkowski. Fdtd simulation of the nonlinear gain dynamics in active optical waveguides and semiconductor microcavities. *IEEE Journal of selected topics in quantum electronics*, 10(5):1052–1062, 2004.

[76] Yingyan Huang and Seng-Tiong Ho. Computational model of solid-state, molecular, or atomic media for fdtd simulation based on a multi-level multi-electron system governed by pauli exclusion and fermi-dirac thermalization with application to semiconductor photonics. *Optics express*, 14(8):3569–3587, 2006.

[77] Sebastian Wuestner, Andreas Pusch, Kosmas L Tsakmakidis, Joachim M Hamm, and Ortwin Hess. Gain and plasmon dynamics in active negative-index metamaterials. *Philosophical Transactions of the Royal Society A: Mathematical, Physical and Engineering Sciences*, 369(1950):3525–3550, 2011.

[78] Andreas Pusch, Sebastian Wuestner, Joachim M Hamm, Kosmas L Tsakmakidis, and Ortwin Hess. Coherent amplification and noise in gain-enhanced nanoplasmonic metamaterials: A maxwell-bloch langevin approach. *ACS nano*, 6(3):2420–2431, 2012.

[79] Montacer Dridi and George C Schatz. Model for describing plasmon-enhanced lasers that combines rate equations with finite-difference time-domain. *JOSA B*, 30 (11):2791–2797, 2013. 28, 29

[80] JP Martikainen, TK Hakala, HT Rekola, and P Törmä. Modelling lasing in plasmonic nanoparticle arrays. *Journal of Optics*, 18(2):024006, 2016. 28

[81] Allen Taflove and Susan C Hagness. *Computational electrodynamics*. Artech House Publishers, 2000. 28, 61

[82] Jan Trieschmann, Shumin Xiao, Ludmila J Prokopeva, Vladimir P Drachev, and Alexander V Kildishev. Experimental retrieval of the kinetic parameters of a dye in a solid film. *Optics Express*, 19(19):18253–18259, 2011. 28

[83] Klaus Böhringer and Ortwin Hess. A full-time-domain approach to spatio-temporal dynamics of semiconductor lasers. i. theoretical formulation. *Progress in Quantum Electronics*, 32(5):159–246, 2008.

[84] Sebastian Wuestner, Andreas Pusch, Kosmas L Tsakmakidis, Joachim M Hamm, and Ortwin Hess. Overcoming losses with gain in a negative refractive index metamaterial. *Physical Review Letters,* 105(12):127401, 2010. 28

[85] JA Rogers and RG Nuzzo. Nanostructured plasmonic sensors. *Chem Rev*, 108(2): 494521, 2008. 31

[86] Huaqing Li and Nianqiang Wu. A large-area nanoscale gold hemisphere pattern as a nanoelectrode array. *Nanotechnology*, 19(27):275301, 2008. 31

[87] J Rybczynski, U Ebels, and M Giersig. Large-scale, 2d arrays of magnetic nanoparticles. *Colloids and Surfaces A: Physicochemical and Engineering Aspects*, 219(1):1–6, 2003. 32

[88] Boris Kalinic, Tiziana Cesca, Carlo Scian, Niccoló Michieli, Ionut Gabriel Balasa, Enrico Trave, and Giovanni Mattei. Emission efficiency enhancement of er3+ ions in silica by near-field coupling with plasmonic and pre-plasmonic nanostructures. *physica status solidi (a)*, 215(3):1700437, 2018. 32

[89] Valentina Russo, Tiziana Cesca, Carlo Scian, Davide Silvestri, Margherita Morpurgo, Giovanni Mattei, et al. Gold–silver alloy semi-nanoshell arrays for label-free plasmonic biosensors. *Nanoscale*, 9(28):10117–10125, 2017. 32

[90] Michael Christian Gwinner, Elisabeth Koroknay, Liwei Fu, Piotr Patoka, Witold Kandulski, Michael Giersig, and Harald Giessen. Periodic large-area metallic split-ring resonator metamaterial fabrication based on shadow nanosphere lithography. *Small*, 5(3):400–406, 2009. 32

[91] Zuzanna A Lewicka, Yang Li, Arash Bohloul, W Yu William, and Vicki L Colvin. Nanorings and nanocrescents formed via shaped nanosphere lithography: a route toward large areas of infrared metamaterials. *Nanotechnology*, 24(11):115303, 2013. 32

[92] George Gabriel Stokes. *On the effect of the internal friction of fluids on the motion of pendulums*, volume 9. Pitt Press Cambridge, 1851. 33

[93] Nikolai D Denkov. Two-dimensional crystallization. *Nature*, 361(6407):26, 1993. 34

[94] Seyed Milad Mahpeykar, Qiuyang Xiong, Jue Wei, Lingju Meng, Brandon K Russell, Peter Hermansen, Akshay V Singhal, and Xihua Wang. Stretchable hexagonal diffraction gratings as optical diffusers for in situ tunable broadband photon management. *Advanced Optical Materials*, 4(7):1106–1114, 2016. 36

[95] Takashi Yamasaki and Tetsuo Tsutsui. Fabrication and optical properties of two-dimensional ordered arrays of silica microspheres. *Japanese journal of applied physics*, 38(10R):5916, 1999. 37, 38

[96] Stephen M Rossnagel, Jerome J Cuomo, and William Dickson Westwood. *Handbook of plasma processing technology: fundamentals, etching, deposition, and surface interactions*. William Andrew, 1990. 38

[97] Donald M Mattox. *Handbook of physical vapor deposition (PVD) processing*. William Andrew, 2010. 40

[98] Fathima S Ameer, Shilpa Varahagiri, Donald W Benza, Daniel R Willett, Yimei Wen, Fenglin Wang, George Chumanov, and Jeffrey N Anker. Tuning localized surface plasmon resonance wavelengths of silver nanoparticles by mechanical deformation. *The Journal of Physical Chemistry C*, 120(37):20886–20895, 2016. 46

[99] Jihad René Albani. *Structure and dynamics of macromolecules: absorption and fluorescence studies*. Elsevier, 2011. 48

[100] HD Försterling and H Kuhn. *Physikalische Chemie in Experimenten, Verlag Chemie*. Weinheim, 1971. 48

[101] Joseph T Verdeyen. *Laser Electronics. 3ed*. Prentice Hall, 1995. 49, 50

[102] IP Kaminow, LW Stulz, EA Chandross, and CA Pryde. Photobleaching of organic laser dyes in solid matrices. *Applied Optics*, 11(7):1563–1567, 1972. 51, 74

[103] T Bernas, M ZarEBski, RR Cook, and JW Dobrucki. Minimizing photobleaching during confocal microscopy of fluorescent probes bound to chromatin: role of anoxia and photon flux. *Journal of Microscopy*, 215(3):281–296, 2004. 51

[104] Michelle S Mackey and Wade N Sisk. Photostability of pyrromethene 567 laser dye solutions via photoluminescence measurements. *Dyes and Pigments*, 51(2):79–85, 2001. 51

[105] James Pawley. *Handbook of biological confocal microscopy*. Springer Science & Business Media, 2010. 51

[106] Carl Zeiss Microscopy GmbH. Zeiss geminisem, 2019. URL `https://www.zeiss.com/microscopy/int/products/scanning-electron-microscopes/geminisem.html`. Available on line. 54

[107] Bruker Corporation. Tapping mode afm, 2019. URL `https://blog.brukerafmprobes.com/guide-to-spm-and-afm-modes/tapping-mode-afm/`. Available on line. 54

[108] David Nečas and Petr Klapetek. Gwyddion: an open-source software for spm data analysis. *Open Physics*, 10(1):181–188, 2012. 54

[109] James A Lock and Gérard Gouesbet. Generalized lorenz–mie theory and applications. *Journal of Quantitative Spectroscopy and Radiative Transfer*, 110(11):800–807, 2009. 57

[110] G Pellegrini and G Mattei. High-performance magneto-optic surface plasmon resonance sensor design: An optimization approach. *Plasmonics*, 9(6):1457–1462, 2014. 57

[111] Charalambos C Katsidis and Dimitrios I Siapkas. General transfer-matrix method for optical multilayer systems with coherent, partially coherent, and incoherent interference. *Applied optics*, 41(19):3978–3987, 2002. 57

[112] Peter P Silvester and Ronald L Ferrari. *Finite elements for electrical engineers*. Cambridge university press, 1996. 57

[113] Olaf Schenk and Klaus Gärtner. Solving unsymmetric sparse systems of linear equations with pardiso. *Future Generation Computer Systems*, 20(3):475–487, 2004. 57

[114] D Cassagne, C Jouanin, and D Bertho. Hexagonal photonic-band-gap structures. *Physical review B*, 53(11):7134, 1996. 65

[115] Lukas Novotny and Bert Hecht. *Principles of nano-optics*. Cambridge University Press, 2012. 65

[116] Lev Davidovich Landau and Evgenii Mikhailovich Lifshitz. *Quantum mechanics: non-relativistic theory*, volume 3. Elsevier, 2013. 68

[117] Franco Laeri, Ferdi Schüth, Ulrich Simon, and Michael Wark. *Host-Guest-Systems Based on Nanoporous Crystals*. John Wiley & Sons, 2006. 74, 75

[118] Frank J Duarte, Paul Kelley, Lloyd W Hillman, and Peter F Liao. *Dye laser principles: with applications*. Academic Press, 1990. 77

[119] Uri Ganiel, A Hardy, G Neumann, and D Treves. Amplified spontaneous emission and signal amplification in dye-laser systems. *IEEE Journal of Quantum Electronics*, 11(11):881–892, 1975. 77

[120] Otto Loebich. The optical properties of gold. *Gold Bulletin*, 5(1):2–10, 1972. 84

[121] Mark Csele. *Fundamentals of light sources and lasers*. Wiley Online Library, 2004. 88